SYNTHETICALLY CONTROLLING DOPING AND NANOSCALE MORPHOLOGY IN VAPOR-LIQUID-SOLID GROWN SILICON NANOWIRES TO ENCODE FUNCTIONALITY

Joseph Dale Christesen

A dissertation submitted to the faculty at the University of North Carolina at Chapel Hill in partial fulfillment of the requirements for the degree of Doctor of Philosophy in the Department of Chemistry in the College of Arts and Sciences.

Chapel Hill
2016

Approved by:

James Cahoon

John Papanikolas

Andrew Moran

Joanna Atkin

Rene Lopez

© 2016
Joseph Dale Christesen
ALL RIGHTS RESERVED

ABSTRACT

Joseph Dale Christesen: Synthetically Controlling Doping and
Nanoscale Morphology in Vapor-Liquid-Solid Grown Silicon Nanowires
to Encode Functionality
(Under the direction of James Cahoon)

Control of morphology and composition on nanometer length scales is a necessary tool for tuning the optical and electrical properties of semiconductor devices. Currently, this is achieved through "top-down" lithographic fabrication techniques, which are prohibitive due to high costs, increased complexity, and/or low throughput. Therefore, a new strategy is needed in order to create low cost and scalable method for fabricating nanomaterials for future semiconductor applications. Semiconductor nanowires (NWs) synthesized through the vapor-liquid-solid (VLS) mechanism are an ideal nanomaterial, as they enable rational synthetic control over composition, morphology, and corresponding properties of the NW from the atomic to microscopic scale.

First, we report a bottom-up method to break the conventional "wire" symmetry and synthetically encode a high-resolution array of arbitrary shapes along the NW growth axis. Rapid modulation of phosphorus doping combined with selective wet-chemical etching enables morphological features as small as 10 nm to be patterned over wires more than 50 μm in length. We then investigate the abruptness of these heterojunctions, which is important for a range of technologies. The abruptness of the heterojunction is mediated by the liquid catalyst, which can act as a reservoir of material and impose a lower limit on the junction width. We demonstrate that this "reservoir effect" is not a fundamental limitation and can be suppressed by selection of specific VLS reaction conditions. Using this precise control of the morphology of the Si NW, we were able synthesis a variety of devices with applications in optics, electronics, and computation.

Finally, we investigate the effect of device geometry and compositional control over the photovoltaic performance of axial and radial Si NW p–n junctions through finite-element simulations. We compare simulated current–voltage data to experimental measurements, permitting detailed analysis of NW performance, limitations, and prospect as a technology for solar energy conversion.

To my loving wife. Thanks for being with me through this adventure.

ACKNOWLEDGMENTS

I would like to thank my entire family for all of their support. Words cannot express how thankful I am to my parents, Steve and Laurie, my brothers, Brien and Eric, my grandmother, Elaine, and all of my aunts, uncles, and cousins who helped motivate me over my five years of graduate school. I would also thank my wife, Sarah Christesen, for being with me for every step of this journey, and who's support and understanding helped keep me going.

I would also like to thank my mentor and advisor Professor James F. Cahoon for five years of invaluable advice and guidance. I am thankful for his expertise, passion, and dedication to helping me grow and mature as a researcher. His encouragement and critiques pushed me to follow my dreams, and it allowed me to go beyond what I though I could ever accomplish during graduate school.

I would also like to thank all of the members of the Cahoon lab who were always willing to take time out of their day to help with experiments or answer any questions that I had about my project or science in general. Their support and encouragement pushed me to always better myself in my research, and I am truly grateful for all of their help.

I would also like to thank my friends who kept me grounded and sane during my time at UNC. They made the whole process enjoyable and worthwhile.

TABLE OF CONTENTS

LIST OF FIGURES . . . . **xi**

LIST OF TABLES . . . . **xiii**

CHAPTER 1: INTRODUCTION **1**

1.1 Morphology Control in Semiconductors 1

1.2 Semiconductor Nanowire Synthesis 4

1.2.1 Heterostructures 7

1.3 Properties of Semiconductor Nanowires 9

1.3.1 Morphology 13

CHAPTER 2: METHODS **15**

2.1 Nanowire Growth 15

2.1.1 Substrate Preparation 15

2.1.2 Nanowire Nucleation and Growth 16

2.1.3 Epitaxial Shell Deposition 17

2.1.4 Oxidation 17

2.2 Wet-chemical Etching 18

2.3 Imaging and Analysis 19

2.3.1 Scanning Electron Microscopy 19

2.3.2 Transmission Electron Microscopy and Energy-Dispersive x-Ray Spectroscopy 19

2.3.3 Fitting Diameter and Dopant Profiles 20

2.4 Device Fabrication 21

2.4.1 Marker Pattern Fabrication 21

2.4.2 Nanowire Registration 22

2.4.3 Nanowire Etching for Radial Photovoltaic Devices 22

2.4.4 Evaporation of Metal Contacts 22

2.4.5 Resistivity Measurements 23

2.4.6 Photovoltaic Measurements 24

2.5 Finite Element Simulations 24

2.5.1 Optical Simulations 24

2.5.2 Electrostatic Simulations 25

CHAPTER 3: SYNTHETICALLY ENCODING 10 NM MORPHOLOGY IN SILICON NANOWIRES 31

3.1 Introduction 31

3.2 Methods 33

3.3 Characterization and Optimization of ENGRAVE 33

3.4 Applications 37

3.5 Conclusion 41

CHAPTER 4: ENCODING ABRUPT AND UNIFORM DOPANT PROFILES IN VAPOR–LIQUID–SOLID NANOWIRES BY SUPPRESSING THE RESERVOIR EFFECT OF THE LIQUID CATALYST 42

4.1 Introduction 42

4.2 Results 44

4.3 Kinetic Modeling and Analysis 52

4.4 Conclusions 60

CHAPTER 5: ROOM TEMPERATURE ELECTRONIC RATCHETS IN ANISOTROPIC SAWTOOTH SILICON NANOWIRES . . 62

5.1 Introduction 62

5.2 Results 64

5.3 Conclusion 68

CHAPTER 6: DESIGN PRINCIPLES FOR PHOTOVOLTAIC DEVICES BASED ON SILICON NANOWIRES WITH AXIAL OR RADIAL P–N JUNTIONS 69

6.1 Introduction 69

6.2 Methods 71

6.3 Results 72

CHAPTER 7: CONCLUSIONS 87

APPENDIX: CODE FOR IMAGE ANALYSIS **89**

REFERENCES **121**

LIST OF FIGURES

Figure 1.1: Si–Au binary phase diagram 5

Figure 1.2: Schematic illustration of axial and radial NW heterostructures 7

Figure 1.3: Methods for bottom-up control of NW morphology. 12

Figure 3.1: Synthesis of Si NWs with encoded morphology 32

Figure 3.2: Characterization of NW growth, etching, and morphology. 34

Figure 3.3: SEM images and phosphine flow profiles for the synthesis of Si NWs with complex morphology 36

Figure 3.4: Thermal Oxidation of ENGRAVE structures. 37

Figure 3.5: Nanogap-encoded NWs for plasmonics. 39

Figure 3.6: Nanorod-encoded NW for non-volatile memory 40

Figure 4.1: VLS NW growth and the reservoir effect 43

Figure 4.2: Characterization of P doping in VLS-grown Si NWs 45

Figure 4.3: Fit of the EDS spectrum 46

Figure 4.4: n-type Si NW resistivity measurements 47

Figure 4.5: EDS spectrum, HAADF-STEM image, and EDS elemental images of a ntype/intrinsic/n-type segment. 49

Figure 4.6: Arrhenius plot for VLS growth and VS overcoating. 50

Figure 4.7: Evaluating the abruptness of P dopant profiles in Si NWs 51

Figure 4.8: Transition width at various carrier gas flow rates with a constant NW growth rate . . . 53

Figure 4.9: Influence of NW growth rate and diameter on the abruptness of n-type/intrinsic dopant heterostructures . . . 57

Figure 4.10: Suppressing the reservoir effect for diameter-independent, high-resolution heterostructures . . . 60

Figure 5.1: Principles of geometric diodes and fabrication of sawtooth Si NWs . . . 63

Figure 5.2: Four-point probe measurements of geometric diodes . . . 66

Figure 6.1: Overview of NW geometries used for photovoltaics . . . 70

Figure 6.2: Details of simulation geometries used for finite-element modeling . . . 71

Figure 6.3: Charge density and electric field distributions for axial and radial NWs . . . 73

Figure 6.4: Depiction of the space-charge region in radial NWs at low doping levels . . . 74

Figure 6.5: Analysis of axial p–i–n junction photovoltaic device characteristics . . . 75

Figure 6.6: Analysis of radial p–i–n junction photovoltaic device characteristics . . . 78

Figure 6.7: Analysis of radial p–i–n junction photovoltaic device characteristics . . . 80

Figure 6.8: Comparison of simulated and experimental I–V or J–V curves for single-nanowire (NW) photovoltaics under 1 sun illumination . . . 82

Figure 6.9: Effective minority carrier diffusion length in axial NWs . . . 84

Figure 6.10: Photovoltaic performance of axial NWs at high doping levels . . . 85

Figure 6.11: IQE of axial and radial NWs . . . 86

LIST OF TABLES

Table 4.1: Encoded doping levels and measured active doping levels 48

Table 6.1: Simulated photovoltaic metrics for axial NW p–i–n junctions 76

Table 6.2: Simulated photovoltaic metrics for radial NW p–i–n junctions with donor/acceptor doping levels of 1e18 79

Table 6.3: Simulated photovoltaic metrics for radial NW p–i–n junctions with donor/acceptor doping levels of 1e20 79

Table 6.4: Comparison of experimental and simulated photovoltaic metrics for axial and radial NWs 81

LIST OF ABBREVIATIONS

2DEG two–dimensional electron gas

BHF buffered hydrofluoric acid

CVD chemical–vapor–deposition

EBL electron–beam lithography

EDS energy–dispersive x–ray spectroscopy

ENGRAVE Encoded Nanowire GRowth and Appearance through VLS and Etching

FF fill factor

FIB focused ion beam

$\mathbf{I_{SC}}$ short–circuit current

IPA isopropyl alcohol

IQE internal quantum efficiency

IR infrared

$\mathbf{J_{SC}}$ short–circuit current density

$\mathbf{L_{eff}}$ effective minority carrier diffusion length

LED light-emitting diode

MFPL mean–free path length

MIBK methyl isobutyl ketone

MMA methyl methacrylate

NPGS Nanometer Pattern Generation System

NW nanowire

PML perfectly matched layer

PMMA polymethyl methacrylate

QD quantum dot

sccm standard cubic centimeters per minute

SEM scanning electron microscope

SERS surface–enhanced Raman spectroscopy

SOI silicon–on–insulator

SPP surface plasmon polariton

SRH Shockley–Read–Hall

SRV surface recombination velocity

STEM scanning transmission electron microscope

TEM transmission electron microscope

UV ultraviolet

$\mathbf{V_{OC}}$ open–circuit voltage

VLS vapor–liquid–solid

VS vapor–solid

VSS vapor–solid–solid

WZ wurtzite

ZB zincblende

CHAPTER 1: INTRODUCTION

1.1 Morphology Control in Semiconductors

Since the discovery of semiconductors, control of morphology and composition has been a necessary tool in tuning the optical and electrical properties of devices. Control of doping and pattering of Si in particular enabled the departure from vacuum tube to the solid state transistor, which ushered in the digital age.[1] As the control of doping and pattering increased, so did the quality and quantity of the transistors.[2] The technology for controlling the morphology and composition improved at such a rate that Gordon Moore famously predicted, "The complexity for minimum component costs has increased at a rate of roughly a factor of two per year. Certainly over the short term this rate can be expected to continue, if not to increase. Over the longer term, the rate of increase is a bit more uncertain, although there is no reason to believe it will not remain nearly constant for at least ten years."[3] Moore's law, as it is generally referred to, continued not just for the ten years that Gordon Moore predicted, but for over fifty years.

The technology, which allowed for the growth in manufacturing of transistors in accordance with Moore's Law, is photolithography; a process that utilizes light to transfer a geometric pattern from a photomask onto another substrate. This transfer is mediated by a chemical photoresist, which when exposed to light will either become soluble (positive photoresist) or insoluble (negative photoresist) in a photoresist developer. The selective removal of photoresists allows for removal of, deposition on, or alteration of the exposed areas of the substrate as defined by the photomask. This process can be repeated multiple times in sequence to create the complex structures of various compositions and morphologies necessary to produce transistors and other

electrical components. The resolution at which the photomask can be transferred to the photo resist is generally limited by the Abbe diffraction limit, which can be written as

$$d = \frac{\lambda}{2n\sin\theta} \tag{1.1}$$

where λ is the wavelength of light, θ is the angle of incidence, n is the refractive index, and d is the spot size. Therefore, the resolution can be improved by either decreasing the wavelength or increasing the denominator, $n\sin\theta$, which is generally referred to as the numerical aperture. This has led to lithographic techniques such as extreme ultraviolet, immersion, and phase shift lithography in an attempt to improve the resolution of photolithography beyond the diffraction limit.[4–7] While these techniques can improve the resolution down to tens of nanometers, they become increasingly more complex, difficult, and/or cost prohibitive to manufacture and utilize in various nanotechnology applications.

Other techniques for creating structures on the order of nanometers include electron–beam lithography (EBL) and focused ion beam (FIB) milling and deposition.[4,8,9] EBL utilizes electrons instead of light to expose the resist and create the desired geometry on the substrate. Because the wavelength of electrons at 30 keV is much smaller than the wavelength of ultraviolet (UV) photons, EBL has a resolution of a few nanometers. However, the throughput for EBL is a limiting factor as the electron beam must raster scan over the substrate as opposed to photolithography, which exposes the entire sample at once. FIB milling, which uses ions to remove material selectively from the substrate without the need for a resist, and deposition, which uses ions to selectively react a gas phase precursor onto the sample, both suffer from the same problem as EBL in that it is needs to raster scan the ion source over the entire sample, which greatly reduces its throughput.

These "top-down" lithographic fabrication techniques are prohibitive for creating nanostruc-

tures due to high costs, increased complexity, and/or low throughput, and therefore, a new strategy is needed in order to create low cost and scalable method for creating nanomaterials for future semiconductor applications. Significant research has been devoted to the "bottom-up" chemical synthesis of semiconductor nanostructures, and this paradigm offers a scalable method for creating nanostructures with atomic precision and distinct composition, size, and morphology.

These semiconductor nanostructures are generally categorized based on the number of non-nanoscale dimensions the structure posses. 0-D structures, or quantum dots (QDs), are structures in which all three dimensions are in the nanoscale, and they have been synthesized with a wide variety of shapes, sizes, and compositions.[10,11] Solution based synthesis methods are the most common for QDs, and they allow for precise control of size and composition and is readily scalable to various manufacturing processes including roll-to-roll printing.[12] QDs are usually only a few nanometers in size, which gives rise to quantum confinement effects and including size dependent photoluminescence.[10] These quantum effects have been studied for various applications in photonics and electronics including lighting and photovoltaics.[13–15] While the quantum mechanical description for the semiconductor dot is well understood, a significant amount of research has been devoted to understanding the chemistry and electron kinetics of the solution interface of QD as well as transfer of electrons between QDs, which is necessary for future applications where electronic connection between QDs is paramount.[16,17]

2-D materials are nanomaterials that have one nanoscale dimension, usually a single to a few atomic layers, and two dimensions that are not nanoscale. Significant research into this class of materials has only started to take off recently with the isolation of individual graphene sheets about a decade ago.[18] Graphene has showed great promise due to a number of excellent properties including extreme mechanical strength, high electron and thermal conductivities, and impermeability to gas among others, but its lack of a band gap made it unsuitable for use as

transistor in electronic applications.[19] Other 2-D materials have been studied for applications in transistor electronics as well as photonics including transition metal dichalcongenides, which have band gaps ranging from the UV to the infrared (IR) .[20] However, most methods for synthesizing these 2D materials require separating bulk material into individual sheets though mechanical or chemical means, and therefore, it lacks precise control of composition as well as geometry though research is currently progressing on addressing these issues.

1-D structures, or NWs, are high aspect ratio nanomaterials in which only two dimensions are nanoscale, and they have become one of the most powerful tools for nanoscience. Through semiconductor NWs, it is possible to ab initio design and synthetically tune the composition, morphology, and corresponding properties of the NW from the atomic to microscopic scale. This level of control makes NWs an ideal nanomaterial building block, enabling a wide variety of new technologies as well as improvements on previous technologies, and will be the focus of this dissertation.

1.2 Semiconductor Nanowire Synthesis

First discovered by Wagner and Ellis at Bell Labs in 1964,[21] the vapor–liquid–solid (VLS) growth mechanism is one of the most common methods for NW growth due its excellent control of diameter[22] and composition[23] and its compatibility with a wide variety of materials and systems. Discussion of the VLS mechanism should first start with a phase diagram, and as the NWs grown in this dissertation are Si catalyzed by Au, we will use the Au–Si phase diagram as shown in Figure 1.1 as the example even though VLS mechanism can be performed with any metal–semiconductor combination, which forms a eutectic system. The system starts off with pure Au nanoparticles at room temperature, and they are subsequently heated to a temperature above the eutectic point. A vapor phase Si precursor (e.g. SiH_4, Si_2H_8, or $SiCl_4$) is then introduced and reacts with the Au catalysts to form a liquid Si–Au alloy and solid Au particle.

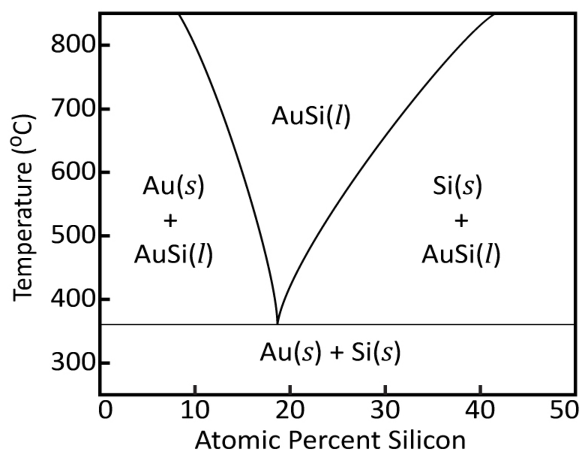

Figure 1.1: Si–Au binary phase diagram.

More Si precursor is continually introduced into the system such that the alloy concentration moves toward continually increasing Si concentration until no solid Au remains, and the particle is a complete liquid droplet. The liquid alloy is pushed out of equilibrium by the continual incorporation of the Si precursor into the liquid droplet, and eventually, the liquid droplet crystallizes solid Si in an area defined by the size of the original Au nanoparticle. Therefore, the size of the initial Au catalyst determines the final diameter of the Si NW.

For many applications of VLS grown NWs, it is necessary to grow NWs with a high level of precision over parameters such as diameter, crystallinity, crystal direction, and uniformity. Therefore, it is crucial to understand key factors of NW growth via the VLS mechanism in order to synthetically control crystal direction, crystal defects, kinking, and overcoating. Crystal defects such as twin planes,[24–27] stacking faults,[25] and screw dislocations[28–30] are know to affect the growth morphology as well as optical[31] and electronic properties[32] of NWs and can be controlled through a wide variety of synthetic parameters including gas flow rates,[30] temperature,[25] and surface chemistry.[24] Twin planes and stacking faults can occur in group IV and III–V NWs both perpendicular[25] or parallel[26] to the growth direction and have been shown to cause electron scattering, which inhibits electron transport along the NW.[33,34] These

crystal defects can also lead to mixtures of wurtzite (WZ) and zincblende (ZB) crystal structures generally in III–V semiconductor NWs and can be controlled through a combination of NW diameter and temperature.[25] The WZ and ZB crystal structures have different band gaps and can even switch between direct and indirect-band gaps in certain materials.[35]

Beyond crystal defects, changes in the NW growth direction during synthesis, also known as kinking, can prevent alignment of NWs or can be used in a rational design of more complex large scale devices. NW growth direction has been shown to be controlled by a wide range of synthetic parameters including temperature,[36–38] pressure,[39–41] catalyst composition,[42,43] and type of gas phase precursors.[41,44,45] These parameters are different methods of changing the surface chemistry, and it is the surface chemistry at the interface between the vapor phase precursors, liquid catalyst, and solid NW that defines the growth. Changes to the surface chemistry at this point will change the contact angle of the catalyst as well as its stability.[46] For growth of Si NWs in the <111> crystal direction, it has been shown that Au diffusion along the side walls lowers the surface energy and prevents the NW from kinking into the preferred <112> crystal direction.[37,43,47] By changing the surface chemistry of the NW itself, it is possible to change the growth direction of the NW during the growth in order to create more complex structures.[24,26,48]

The surface chemistry not only plays a vital role in determining the NW growth direction, but it also plays a role in preventing amorphous deposition of the vapor-precursor on the side of the NW.[46,49–51] This deposition, generally referred to as vapor–solid (VS) growth, can lead to tapered NWs, unintended doping, low resistance shunt pathways, and nonuniformities in composition and structure, or as will be discussed in the next section, can be used to create rationally designed heterostructures.[52–55] Unintended VS overcoating can be prevented by either lowering the growth temperature to a point where VS overcoating is negligible over the time scale of the NW growth[56] or by modifying the surface adsorbates to block any overcoating and

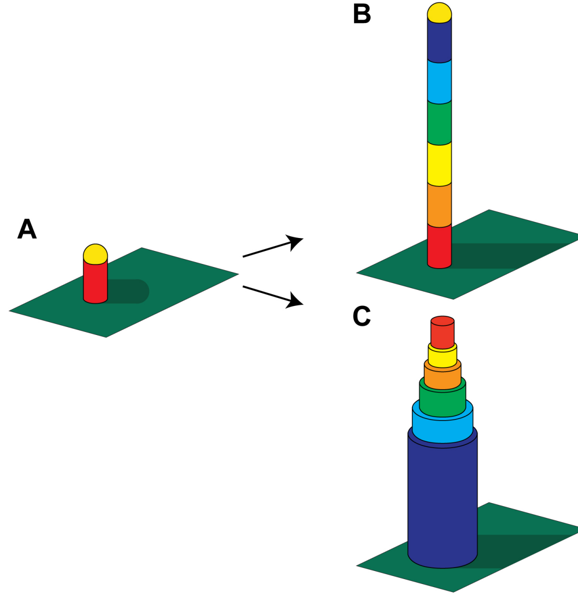

Figure 1.2: Schematic illustration of a (A) VLS growth of a homogeneous NW, and the subsequent formation of heterostructures from (B) continued VLS growth or (C) VS growth.

promote stable growth.[46,49–51] The surface adsorbate used are atoms or small molecules (i.e. H[46], Cl[51], CH_3[46,49,50]) that will readily adsorb to the NW and prevent any reactions of the precursor gas with the NW surface.

1.2.1 Heterostructures

The true power of NWs is the ability to tune structure and composition on a variety of length scales ranging from single atoms to microns, which is due in part to the wide variety of materials that are compatible with VLS mechanism. It is these heterostructures that enable breakthroughs and advances in technology. The ability to modulate composition both axially and radially with respect to the NW growth direction as schematically depicted in Figure 1.2 allows for synthetic control of diverse set of properties including band gap, Fermi level, crystal structure, dielectric constant, modulus, thermal conductance, mobility, carrier concentration, and many others.

Axial heterostructures are formed by switching, adding, or removing gas phase precursor during VLS growth as depicted in Figure 1.2B. For heterostructures formed by switching, the NW will continue to grow, utilizing the reservoir of material remaining in the catalyst while

simultaneously incorporating a new material. Because of the time necessary to completely switch the materials in the catalyst, the demarcation between the two materials in the solid NW will be blurred in what is commonly know as the "reservoir effect" in the NW literature. This effect has been observed for heterostructures involving a change in dopants (e.g., P-doped Si[52] and Si-doped GaAs[57]) and structures involving a change in semiconductor (e.g., Si/Ge[58–60] and GaAs/InAs[61,62]). For group IV NWs, transition widths comparable to the wire diameter have been observed for P dopant transitions[52] as well as junctions between Si and Ge.[58–60] Several strategies to mitigate this effect have been developed. For example, metal catalysts with a lower solubility of semiconductor in the liquid, such as an $Au_{1-x}Ga_x$ alloy,[63] can shorten the transition width. Another alternative is to forego the VLS mechanism in favor of a vapor–solid–solid (VSS) mechanism, in which the metal catalyst is solid and has little to no solubility with the semiconductor.[64,65] The VSS growth process has been successfully demonstrated for dopant transitions in Au-catalyzed NWs[66] and for Si/Ge transitions in AuAl-catalyzed NWs.[65] Although VSS growth has been shown to produce near-atomic compositional transitions, the growth rate is slow, preventing application for many devices. For III–V NWs, the reservoir effect has been observed for heterostructures involving a change in dopant and a change in the group III material.[58] However, the effect is generally not observed for a change in the group V material, which has been attributed to the low solubility of group V elements in the liquid catalyst.[63] For structures in which the group III material is changed, methods such as pulsing the group III precursor have improved the transition width, resulting, for example, in sharper InAs/GaAs transitions.[67] In this case, it is believed that Ga reduces the solubility of In in the metal catalyst to reduce the reservoir effect; however, a general strategy for suppression of the effect has yet to be developed.

VS growth can be used to produce highly crystalline and atomically abrupt radial heterostruc-

tures as depicted in Figure 1.1C unlike the unintended, amorphous VS overcoating previously described. By increasing the temperature well above the eutectic temperature and lowering the partial pressure of reactant gasses, the VLS mechanism is suppressed, and overcoating via the VS mechanism is greatly enhanced. The high temperatures also facilitates the formation of an epitaxial crystalline shell on the NW. The radial structures do not have the problem of the reservoir effect because the heterostructure formation does not go through the catalyst. However, at elevated temperatures, there is the possibility of diffusion of materials in the NW, but atomically abrupt heterostructures are possible.

1.3 Properties of Semiconductor Nanowires

NWs exhibit unique optical, electrical, and mechanical properties due to their geometry as well as compositional variation within said geometry. With control over these properties along a single NW, one has the building blocks necessary to create devices for new technologies, and we will discuss these unique properties and how they can be applied to various technologies and devices.

NWs have generated a lot of interest for electronics applications due to the precise band-gap engineering and new devices geometries.[68] Because NWs are synthesized from the bottom-up, it is much easier to control the band-gap, Fermi level, and carrier concentrations through doping or material changes. This allows for fabrication of abrupt[69] or graded[70] heterostructures or thin barriers for quantum applications including single electron transistors[71] or resonant-tunneling diodes.[72]

As traditional Si transistors continue to shrink, it is necessary to improve the mobility of electrons and holes in the channel to increase the transitor speed and prevent losses due to heat. Si has a poor electron and hole mobility relative to other semiconductors, and therefore, a new semiconductor with higher mobilities would be advantageous. However, Si continues to be used in

part due to its low cost, and the inability to reliably fabricate other semiconductors off of silicon–on–insulator (SOI) substrates due to large crystal mismatches. The NW geometry, however, allows for heterostructures between crystals with widely varying lattice constants because the strain can be relaxed at the edge of the NW. Therefore, NWs can be grown epitaxially off of SOI substrates, which makes it a promising candidate for integrating other higher mobility materials with current architectures.

Similar to the precise electronic control, NWs can also be fabricated with control over optical properties such as the type and size of the band gap and refractive index, which makes NWs an attractive building block for light management applications such as light-emitting diodes (LEDs), lasers, single-photon sources, and photodiodes.[73,74] Altering the band gap for tuning the emission of NWs has enabled the fabrication of LEDs with tunable emission from the UV to the IR in a manner not possible with planar technology.[75] Phosphor-free white LEDs have been produced in InGaN/GaN NWs by tuning the length and composition of the InGaN quantum well segments, which is not possible in planar technology due to the quantum confined Stark effect.[76]

NWs can also be fabricated into lasers where the NW defines both the lasing cavity and gain material. The compact footprint of NWs make them promising candidates for applications where current laser sources cannot be used such as optical on-chip communication and in situ biodetection.[77–79] The synthetic variety of NWs allows for tunability in cavity and the gain medium, and NWs lasers have already been demonstrated with wavelengths ranging from the UV all the way out to the IR and have been pumped both optically and electronically.[77–79]

NWs have shown promise in quantum information processing applications as well. A hurdle for quantum information processing is on-demand generation of single photons in order to transfer quantum states, entangle distant quantum memories, or generate encryption keys. QDs have been considered due to their discrete energy levels and controlled emission properties, but

inefficient extraction of photons decreases the overall efficiency of the device. QDs embedded in axial or radial NW heterostructures are a promising candidate due to the high extraction efficiencies provided by the NW scaffold.[80]

Because of their subwavelength size, NWs can generate strong resonances based on their cross-sectional shape and size.[81–83] These resonance modes lead to greatly enhanced light-matter interactions and longer effective absorption path lengths along in the NW. This coupled with low leakage currents in axial p-n junctions makes NWs a promising candidate for wavelength selective avalanche photodiodes.[84,85]

These antenna effects also make NWs a promising candidate for next generation photovoltaic architectures along with lower costs through reduced material usage and eliminating the need for high quality crystals. Lower quality semiconductor materials have low minority-carrier diffusion lengths due to either high levels of impurities or defects, and cannot be used in conventional planar photovoltaics. The reason is because the optical and charge carrier paths are along the same axis, and in order to collect the incident light, the optical path needs to be long and is much longer than the minority-carrier diffusion length. NWs, on the other hand, are able to use these lower cost materials because the optical and charge carrier paths can be decoupled, and the charge collection lengths can be on the order of tens of nanometers while maintaining the necessarily long optical path lengths.[86] On the other side of the spectrum, NWs open up the possibility of using more expensive materials because of the optical antenna effect. Because the NWs can collect light from a larger region than their physical size, the NWs can be spaced apart from one another in semiconductor a periodic array and still collect light from the entire device. The NWs can also be can be grown off of inexpensive substrates adding another cost saving measure in the production of photovoltaics.[87]

While nanoscale photonic components are important for increasing computation speeds, the

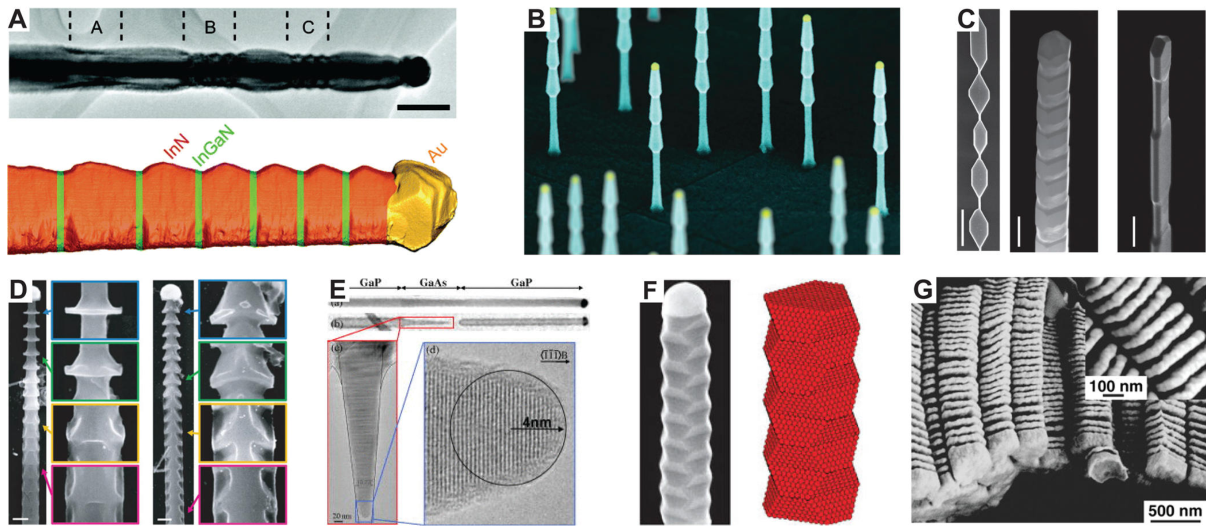

Figure 1.3: Methods for bottom-up control of NW morphology. (A) Diameter modulation of III–V VLS-grown NWs; scale bar, 100 nm. (B) Chemically controlled VS sidewall deposition on Ge NWs. (C) High-temperature shell deposition on Si NWs showing periodicity as a result of Plateau–Raleigh instability; scale bars, 400 nm. (D) Si NWs with Au silicide that acts as an etch stop for aqueous KOH etching; scale bars, 200 nm. (E) GaAs/ GaP NWs etched in aqueous KOH solution. (F) Twinning super lattice in InP NWs. (G) Au NWs with gaps produced by on-wire lithography (OWL). Reprinted with permission from Christesen, J. D., Pinion, C. W., Hill, D. J., Kim, S. & Cahoon, J. F. Chemically Engraving Semiconductor Nanowires: Using Three-Dimensional Nanoscale Morphology to Encode Functionality from the Bottom Up. J. Phys. Chem. Lett. **2016**, *7*, 685–692. Copyright 2015 American Chemical Society.

speed increases are achieved from interconnects as opposed to computation. This is because photons only weakly interact with one another and require more complex nonlinear materials to create optical transistors or logic gates. Therefore, a new architecture is needed to increase the computation frequency. Surface plasmon polaritons (SPPs) are a coherent oscillation of electrons at the interface of a metal and a dielectric, and they operate at high frequencies comparable to visible light but are confined to the dielectric-metal interface. So they have frequencies comparable to light but can be confined in a small area and can interact with one another meaning they could enable faster computing speeds. Along with application in computing, the evanescent field of SPP produces an extremely high electric field, which has been used for chemical detection in surface enhanced Raman spectroscopy.[88]

1.3.1 Morphology

The NW geometry offers a platform for nanometer-scale morphological control, and significant research effort has been devoted toward controlling the morphology of wires grown by VLS mechanism.[25,49,50,89–98] For example, the Gradecak research group at MIT modulated the diameter of III–V NW catalysts by altering the catalyst supersaturation, allowing an ∼25% modulation of the NW diameter (Figure 1.3A) during VLS growth.[91] Because the morphology change is fundamentally linked to the VLS growth mechanism, the results could potentially be generalized to other VLS-grown NW systems. The Filler group at Georgia Tech has developed methods to modulate the surface chemistry of NWs during growth,[49,50] allowing control of VS sidewall deposition. This method has created tear drop structures in Ge NWs (Figure 1.3B) by modulating the flow of methyl-containing precursors, which passivate the NW sidewall and prevent deposition. The Lieber group at Harvard University used a high-temperature deposition step following VLS growth to induce the growth of a shell that exhibits Plateau–Raleigh instability (Figure 1.3C).[90] By altering the temperature and pressures during this growth process, they created a wide variety of periodic structures with control over both the period and cross-sectional profile. The Tian group at the University of Chicago has utilized rapid depressurization during Si NW growth to induce Au deposition and diffusion along the NW axis, which forms a Au silicide that acts as a mask for ex situ wet-chemical KOH etching.[89] The etch reveals a sawtooth morphology in Si NWs (Figure 1.3D), which were used as novel atomic force microscopy (AFM) tips for interaction with soft matter. The Samuelson group at Lund University has shown several methods of control over the morphology of III–V NWs. With GaP–GaAs NWs, they have produced gaps through an ex situ wet-chemical etch to selectively remove the GaAs segments (Figure 1.3E).[94] For InP NWs, they created long-range twinning super lattices that remove the cylindrical cross section common to many NW systems (Figure 1.3F).[25] Beyond VLS-grown NWs, the Mirkin group at

Northwestern University developed a method termed on-wire lithography (OWL) for creating nanometer-sized gaps in metal NWs (Figure 1.3G).[99] The NWs are grown via electro-deposition into a porous substrate, and the deposited material can be altered during growth. Following growth, the porous substrate is removed and the material is etched, leaving gaps less than 5 nm in length. Other template-assisted growth mechanisms, such as coaxial lithography[100] (COAL) and template-assisted selective epitaxy[101] (TASE), have also been developed to create complex structures.

CHAPTER 2: METHODS

2.1 Nanowire Growth

Si NWs were grown with a home-built, hot-wall chemical–vapor–deposition (CVD) system, which consists of a quartz tube furnace (Lindberg Blue M) with 1 inch diameter bore, fast-responding mass-flow controllers (MKS Instruments P4B), a pressure control system (MKS Instruments 250E), and vacuum system with base pressure of $< 2 \times 10^{-3}$ Torr. The CVD system was computer-controlled using custom Labview software to enable rapid and reproducible modulation of the NW growth conditions and gas flow rates. The NWs are grown using Au nanoparticles dispersed onto a silicon-silicon oxide substrate within a 1 inch outer diameter quartz tube (Chemglass Life Sciences).

2.1.1 Substrate Preparation

The NW-growth substrate (Nova Electronic Materials; p-type Si wafers with 600 nm thermal oxide) is first cut to a width of $\sim$2 cm and a length from 1 to 3 cm so that the substrate resides about midway up in the quartz tube. The substrate is then sonicated with acetone, rinsed with acetone and isopropyl alcohol (IPA), and inserted into a UV-Ozone cleaner (Samco UV-1) for 5 minutes at a temperature of 150 °C. Poly-L-lysine (0.1% w/v in water) is dispersed over the cleaned wafers for a time between 4 and 10 minutes. The wafer is then rinsed with nanopure water (Barnstead Nanopure; 18 $M\Omega$∗cm) and dried with nitrogen gas. Citrate-stabilized Au nanoparticles (BBI International) diluted in nanopure water of ratios ranging from 1:1 to 1:20 are then dispersed on the poly-L-lysine coated substrate for 4 minutes. The substrate is then rinsed in nanopure water and dried with nitrogen before it is then reinserted into the UV-Ozone cleaner

for another 5 minutes at a temperature of 150 °C. The last UV-Ozone cleaning is performed within 6 hours of growth to remove any remaining carbon species from the substrate. Before the wafer is inserted into the quartz tube, the quartz tube is heated to 950 °C for 1 hour under 20 sccm of Ar flow to remove any excess material or contaminates from the tube surface. The quartz tube is allowed to cool down to a temperature $\sim$ 100°C below the initial run temperature, and the wafer is then inserted into the quartz tube within the single-zone quartz tube furnace, such that the substrate is directly above the K-type thermocouple. The system is pumped down to a base pressure of $< 2 \times 10^{-3}$ Torr, heated to the starting temperature, and allowed to settle before the run is started.

2.1.2 Nanowire Nucleation and Growth

NWs are nucleated at a furnace temperature between 420 °C and 460 °C, a total reactor pressure of between 20 and 100 Torr, a carrier gas flow of between 10 and 200 standard cubic centimeters per minute (sccm) of either H_2 (Matheson Tri-Gas; 5N semiconductor grade) or Ar (Matheson Tri-Gas; 5N semiconductor grade), a SiH_4 (Voltaix) flow rate of between 0.5 and 2 sccm, and optionally dopant flows of between 0.15 and 20 sccm of either PH_3 (Voltaix; 1,000 ppm in H_2) or B_2H_6 (Voltaix; 100 ppm in H_2) for between 5 and 30 minutes.

For continued NW growth, the temperature is ramped down from the nucleation temperature to 420 °C with a rate of $\sim$1 °C/min in order to limit the rate of radial overcoating to less than 0.05 nm/min (see Figure 4.6). The calibrated NW growth rate at 420 °C and a SiH_4 partial pressure of 0.4 Torr is $\sim$200 nm/min. During this time period, the flow rates of B_2H_6 and PH_3 can be changed in less than 1 second from the reactor to precisely tune the doping profile of the NW as it grows.

2.1.3 Epitaxial Shell Deposition

Growth of an epitaxial shell is performed directly after the completion of the axial growth of the NW. The chamber is evacuated to its base pressure, and the furnace is then heated to 760 °C with 0.15 sccm of SiH_4 at 25 Torr without breaking vacuum in order to prevent any oxide formation on the NWs. The SiH_4 flow rate is set to its minimum to prevent supersaturation of the catalyst and continued VLS growth. To encode an n-type shell, 0.75 sccm of PH_3 is added. The calibrated shell growth rate under these conditions is ∼1.5–2 nm/min.

2.1.4 Oxidation

Thermal oxidation treatments can be performed in order to passivate surfaces[102] or effect doping levels in Si.[103–106] After the CVD growth is over, NWs were removed from the CVD system, and loaded into another quartz tube furnace (Lindberg Blue M) with three separately controllable temperature zones and a 5 inch diameter bore. The substrate was placed in a quartz boat that remains outside of the furnace while the furnace is heated to temperature. The quartz boat is attached to a quartz rod containing a magnet sealed inside of it at the far end, which allows rapid insertion into the furnace and prevents oxidation of the magnet. The system is pumped down to base pressure and the first zone is heated to 1000 °C. O_2 is then introduced at 20 sccm and the system is pressurized to 100 Torr of pure O_2. The substrate and the quartz boat are inserted into the furnace by using an external magnet to slide the whole assembly in side the tube. The NWs are then oxidized for a time from 1 to 20 min, and the external magnet is used to quickly remove the sample from the furnace. The system is then evacuated to its base pressure before pressurizing with Ar and removing the sample.

In order to enhance absorption in photovoltaic devices, both axial and radial p–i–n NWs were coated with ∼40 nm of silicon oxide using a separate plasma-enhanced CVD process (Advanced Vacuum Vision 310) .

2.2 Wet-chemical Etching

For wet-chemical etching, NWs were mechanically transferred from the growth substrates onto Si wafers coated with 100 nm thermal oxide and 200 nm Si nitride (Nova Electronic Materials). The native oxide of the NWs, which were lying flat on the substrate, was etched by immersing the substrate in concentrated buffered hydrofluoric acid (BHF) (Transense BHF Improved) for 10 s. The substrate was then rinsed in nanopure water twice for 10 seconds each and in IPA for 30 seconds. The IPA was kept at the same temperature as the etch solution to allow the temperature of the substrate to equilibrate before inserting it into the etch solution. The substrate was then inserted into the KOH-etching solution (20.0 g KOH; 80.0 g water; 20 mL IPA as top surface layer) at a temperature between 20 and 40 °C for variable times up to 200 s. The substrate is then rinsed in a slightly acidic solution (∼4% acetic acid in water) to quench the etching process for 10 s, in nanopure water for 10 s, and in IPA for 15 s before drying with nitrogen. It was also noted that for NW transferred onto a marker pattern (see Chapter 2.4.1) the etch rate increased by ∼20-30%.

For NWs grown with significant Au diffusion along the side walls, the Au will act as an etch stop. An Au-etch step can be performed to remove any Au from the surface and can produce better etch results. For Au etching, the substrate is immersed in an Au etching solution (4 g KI; 1 g I_2; 40 mL H_2O) for 15 seconds, rinsed in nanopure water twice for 10 seconds each, rinsed in IPA for 15 seconds, and blown dry with nitrogen. The wet-chemical etching of the NWs can be performed directly after the Au etch by skipping the IPA rinse and drying steps, inserting the substrate directly into the BHF solution, and following the previously described etch steps.

NWs can also be etched on the growth substrate, but there are a few considerations that need to be taken into account in order to prevent etching of the n-type regions. While not necessary for mechanically transferred NWs, etching on the substrate requires vigorous shaking in order

to remove any excess BHF from the sample and allow the KOH to penetrate the NW mesh. Without vigorous shaking, BHF is not completely rinsed, and it will continue to etch the n-type regions through the remaining steps of the etching procedure. The etching of the n-type regions will be nonconformal and porous. It was also noted that the etch rate on the growth substrates was higher than mechanically transferred NWs by ∼50% and that growth substrates with a lower density of NWs produced more conformal etching.

2.3 Imaging and Analysis

2.3.1 Scanning Electron Microscopy

Scanning electron microscope (SEM) imaging was performed with an FEI Helios 600 Nanolab Dual Beam system with an imaging resolution <5 nm using a typical acceleration voltage of 5 kV, imaging current of 86 pA, and a working distance of ∼4 mm.

2.3.2 Transmission Electron Microscopy and Energy-Dispersive x-Ray Spectroscopy

Samples for electron microscopy were prepared by mechanical contact-transfer of the NWs directly onto lacey-carbon transmission electron microscope (TEM) grids (Ted–Pella #01895). Scanning transmission electron microscope (STEM) imaging was performed on a Tecnai Osiris by Professor James McBride at Vanderbilt University operating at 200 kV with a subnanometer probe with a current of 2 nA (spot size 3, 4k extraction voltage). The Osiris is equipped with a Super-X energy–dispersive x–ray spectroscopy (EDS) system, which consists of four solid-state detectors built into the objective lens. The maximum peak counts summed from the four detectors were on the order of 45 kcps. The STEM probe was retuned periodically to maintain the integrity of the imaging conditions and beam intensity. Drift-corrected STEM-EDS maps were obtained using the Bruker Esprit software. Total collection times for each map were 15 min except for chemical doping level data, which required an averaging time of 3 h. Standardless Cliff–Lorimer quantification was performed on the deconvoluted spectra from subsections of the

EDS maps. STEM images were obtained before and after map acquisition to note any change in the sample.

2.3.3 Fitting Diameter and Dopant Profiles

Diameter profiles were obtained from analysis of SEM images using custom program in MATLAB as seen in Appendix . The program first uses the scale bar to identify the scale of each pixel in the image. The user then identifies the orientation of the NW in order for the program to rotate the NW to vertical. Each pixel of the SEM image is then binned based on their intensity values into three separate bins. The diameter is then calculated by scanning across the NW, identifying the position of the two NW edges based on the binned values of each pixel, and calculating the distance between them over the entire length of the NW.

In order to calculate the transition width between n-type and intrinsic segments of NWs, the diameter profiles were fit to a Gaussian convoluted with an exponential. The exponential is used to account for the "reservoir effect", and the convolution of the Gaussian is used to correct for limits of the etching procedure due to mass transport. The equation for a Gaussian convoluted with an exponential used to fit the experimental data is:

$$\begin{aligned} f(t) = cA * \exp\left[\frac{-(t-c_{t0}) * \lambda_a - \sigma_a^2}{\sigma_a^2}\right] * \operatorname{erf}\left[\frac{\sqrt{2} * (t-c_{t0}) * \lambda_a - \sigma_a^2}{(2 * \sigma_a * \lambda_a) + 1}\right] \\ - cA * \left[1 + \operatorname{erf}\left[\frac{\sqrt{2} * (t-c_{t0})}{2 * \sigma_a}\right]\right] + cA * \operatorname{erf}\left[\frac{t-c_{t1}}{\lambda_b}\right] + c_{I1} \end{aligned} \tag{2.1}$$

where cA is the radius of the NW, c_{t0} is the location of the n-type/intrinsic transition, c_{t1} is the location of the intrinsic/n-type transition, σ_a is the Gaussian broadening, λ_a is the transition width of the n-type/intrinsic transition, λ_b is the transition width of the intrinsic/n-type transition, and c_{I1} is an offset.

2.4 Device Fabrication

2.4.1 Marker Pattern Fabrication

Marker patterns were generated using the Nanometer Pattern Generation System (NPGS) system, which is an EBL system, on a Hitachi S4700 Field Emission SEM to precisely identify NW locations in order to make electrical contacts to individual NWs. A Si wafer with a 200 nm Si nitride (Nova Electronic Materials) layer on top was cleaned by sonicating in acetone, rinsing with acetone and IPA, and inserted into a UV-Ozone cleaner for 5 minutes at 150 °C. Two spacer layers of methyl methacrylate (MMA) (MicroChem MMA (8.5) MMA EL 9) were dispersed using a spin coater (Laurell Technologies Model WS-650-23B) onto the cleaned substrate at 4000 rpm for 30 s, and baked at 180 °C for 1 minute after each layer. A final photoresist layer of polymethyl methacrylate (PMMA) (MicroChem 950 PMMA A2) was applied under the same conditions and again baked at 180 °C for 1 minute. The marker pattern was then written with the NPGS system at a working distance of 25 mm, current of 400 pA, and a magnification of 100$\times$ for the inner pattern and a working distance of 25 mm, a current of 7 nA, and a magnification of 20$\times$ for the outer pattern. The substrate is then developed in methyl isobutyl ketone (MIBK) (MicroChem MIBK/IPA 1:3 Developer) for 30 s and rinsed in IPA for 1 minute. The substrate is then loaded into an electron-beam evaporator (Thermionics VE-100) to evaporate $\sim$3 nm of Cr and 50 nm of Au at a rate of $<$1 Å/s at a pressure of $\sim 1 \times 10^{-7}$ Torr. Both metals are degassed before evaporation onto the sample by heating the metals until they reach a deposition rate of $<$0.3 Å/s with the shutter closed, waiting until the chamber reaches its base pressure, and allowing the metals to completely cool. After the metals are evaporated, the excess metal is lifted off by dissolving the remaining MMA and PMMA in acetone.

2.4.2 Nanowire Registration

NWs are then transferred to the marker pattern through mechanical transfer. Two layers of MMA and one layer of PMMA are applied using the same procedure describe before for marker pattern fabrication. Images of the maker pattern are taken using a Zeiss HAL 100 halogen lamp installed on a Zeiss AxioImager A2M upright microscope. A 10x objective with a numerical aperture of 0.2 and a working distance of 14.3 mm (Zeiss EC Epiplan 10x/0.2 HD WD = 14.3 M27) was used for low-magnification images, and a 50x objective with a numerical aperture of 0.75 and a working distance of 1.0 mm (Zeiss EC Epiplan 100x/0.75 HD WD = 1 M27) was used for high-magnification images. The locations of the NWs on the marker pattern were then registered using custom software in Igor, and contacts were drawn to the NWs in the DesignCAD file. After the sample is loaded into the SEM, NPGS is used to identify a transformation matix for the underlying maker pattern relative to the SEM image. Using the transformation matix, the inner contacts were written at a working distance of 25 mm, a current of 400 pA, and a magnification of 100x, and the outer contacts were written at a working distance of 25 mm, a current of 7 nA, and a magnification of 20x.

2.4.3 Nanowire Etching for Radial Photovoltaic Devices

For radial photovoltaic devices, SU-8 photoresist (MicroChem, 2000.5) was patterned by Xing Zhang on 15–30 μm-long portions of the NWs using EBL followed by wet chemical etching with KOH solution (18 g in 60/20 mL water/IPA at 60 °C) to remove the intrinsic and n-type shells in regions of the NWs not covered with resist in order to make electrical contact to the p-type core. SU-8 photoresist was subsequently removed using a UV-Ozone cleaner.

2.4.4 Evaporation of Metal Contacts

The pattern is developed in MIBK for 30 s and IPA for 1 minute. Before the pattern is loaded into the electron-beam evaporator, it is etched in BHF for 10 s followed by two sequential

water rinses for 10 s each, and an IPA rinse for 15 s before drying the sample with nitrogen. This etch is to remove any oxide on the NWs to ensure good contact between the metal and the NWs. Oxide will start to form on the NWs after BHF etching, and therefore, it is imperative to load the sample directly after etching and rinsing to prevent a substantial oxide buildup. Contacts are evaporated using Ti and Pd at pressures of $< 1 \times 10^{-7}$ Torr. To lower the pressure below 1×10^{-7} Torr, Ti and Pd are first degassed as previously described for Cr and Au, and then Ti is evaporated with the shutter closed to getter remaining gaseous species in the chamber. Ti is evaporated at a rate of 0.2 Å/s for 3 nm, and Pd is evaporated for 0.2 Å/s for the first 10 nm, 0.5 Å/s for the next 40 nm, and 1.0 Å/s until the total thickness is 50 nm larger than the NW diameter. The substrate is removed from the chamber, and the resist is dissolved in acetone to remove all excess metal.

2.4.5 Resistivity Measurements

Resitivity measurements were performed in both two terminal and four terminal configurations using a Keithley 2636A SourceMeter in conjunction with either Signatone micropositioners (S-725) and W probe tips (SE-TL) for two terminal measurements or a Lake Shore Cryotronics PS-100 probe station for either two or four terminal measurements. For the two terminal measurements, voltages were sourced in a range from values between ±100 mV to ±1 V from one terminal and currents measured from the second terminal which was held at 0 V. For the four terminal measurement, a constant current is applied across the two outermost terminals, and the resulting voltage drop is measured across the inner contacts. The resistance is calculated based on Ohm's law, and after measurement, NW diameters and lengths were determined by high resolution SEM in order to calculate resistivity.

2.4.6 Photovoltaic Measurements

Dark current–voltage (I–V) curves were measured by Xing Zang and Christopher Pinion using a Keithley 2636A SourceMeter in conjunction with Signatone micropositioners (S-725) and probe tips (SE-TL). I–V curves under 1-sun illumination were also measured by Xing Zang and Christopher Pinion with the same SourceMeter and with metal contacts formed using a wire bonder (West Bond model 7476D) with 1% Si/Al wire. The solar simulator used for light measurements (Newport, model 91191 with 1 kW Xenon lamp) contained an AM1.5G filter and was calibrated to 1-sun (100 mW/cm2) using a calibrated reference solar cell (Newport, model 91150V). After measurement, NW diameters and lengths were determined by high resolution SEM.

2.5 Finite Element Simulations

Both optical and electrostatic finite element simulations were performed using the Comsol Multiphysics commercial software package. Comsol Multiphysics is a finite element analysis, simulation, and solver software package, which enables simulation of a wide variety of systems through inclusion of relevant physics modules. Modules used for optical and electrical simulations include the AC/DC, transport of dilute species, and electrostatics modules.

2.5.1 Optical Simulations

Three-dimensional optical simulations were performed by Christopher Pinion and were implemented using the total-field, scattered-field method in order to evaluate Si/Au hybrid plasmonic structures. The background field was evaluated with a plane wave normally-incident on the substrate using periodic boundary conditions on the four horizontal boundaries, a perfectly matched layer (PML) on the lower boundary, and the plane wave source on the upper boundary. The scattered field was then solved after adding the Si/Au plasmonic structure to the simulation domain and replacing all boundaries with PMLs. Images of the surface plasmon modes (see

Figure 3.5) were generated by evaluating the scattered electric field intensity ($|E|^2$) in a horizontal plane 3 nm above the top surface of the NW.

2.5.2 Electrostatic Simulations

Electrostatic finite-element simulations were used to evaluate photovoltaic as well as phase change memory devices. These simulations used cylindrical symmetry to represent the three-dimensional structure. For both simulations, the external voltage was applied to Ohmic contacts on the n-type regions, and the simulations included realistic doping profiles as well as drift-diffusion physics. Simulations of the photovoltaic devices also include recombination processes to reproduce the current–voltage characteristics of the devices.

For the simulations of photovoltaic devices, the physics is based on the standard semiconductor drift and diffusion model[107,108] in which the electron continuity equation is represented as:

$$\frac{dn}{dt} = \nabla \cdot (D_n \nabla n - \mu_n n E) - R + G = 0 \tag{2.2}$$

where n represents the concentration of electrons, t time, D_n the electron diffusion constant,μ_n the electron drift mobility, E the internal electric field, R the net rate of charge-carrier recombination, and G the optical generation rate of charge carriers. The corresponding equation for holes, p, is given by the analogous equation with substitution of p for n. The electric field, E, is determined by Poisson's equation, which relates E to the electric potential, ψ, and the charge density ρ as:

$$\varepsilon \nabla E = -\varepsilon_r \varepsilon_0 \nabla^2 \psi = \rho \tag{2.3}$$

where ε_r is 11.7, the relative permittivity of Si, and ε_0 is the vacuum permittivity. The charge density, ρ, is calculated as:

$$\rho = q(N_d - Na - n + p) \tag{2.4}$$

where N_d and N_a are the density of donor and acceptor atoms, respectively, and q is the elementary charge. The spatial distributions of the donor and acceptor regions are represented as:

$$N = \begin{cases} N_{d,0} + N_{a,0}exp\left[-\frac{1}{2}(\frac{x-x_a}{\Delta x})^2\right] & (x < x_d) \\ N_{d,0}exp\left[-\frac{1}{2}(\frac{x-x_d}{\Delta x})^2\right] + N_{a,0}exp\left[-\frac{1}{2}(\frac{x-x_a}{\Delta x})^2\right] & (x_d \leq x \leq x_a) \\ N_{a,0} + N_{d,0}exp\left[-\frac{1}{2}(\frac{x-x_d}{\Delta x})^2\right] & (x_a < x) \end{cases} \tag{2.5}$$

where $N_{d,0}$ and $N_{a,0}$ are the maximum donor and acceptor densities, x_d and x_a are the boundaries of the heavily doped donor and acceptor regions, respectively, and x is the width of the dopant transition as represented by a half-Gaussian function. Note that $x_d < x_a$, the length of the intrinsic region is estimated as x_a - x_d, and x represents the radial direction in radial devices and the axial direction in axial devices.

Because of the high doping levels used in NW devices, the mobility values are dependent upon the doping level as given by the empirical relationships:[109]

$$\mu_n = 92\frac{cm^2}{V \cdot s} + 1268\left[1 + \left(\frac{N_a + N_d}{1.3 \times 10^{17}cm^{-3}}\right)^{0.91}\right]^{-1}\frac{cm^2}{V \cdot s} \tag{2.6}$$

and

$$\mu_p = 54.3\frac{cm^2}{V \cdot s} + 406.9\left[1 + \left(\frac{N_a + N_d}{2.35 \times 10^{17}cm^{-3}}\right)^{0.88}\right]^{-1}\frac{cm^2}{V \cdot s} \tag{2.7}$$

The diffusion constants, D_n and D_p, depend on the doping level as given by their dependence on

mobility through the Einstein relation:

$$D = \frac{kT}{q}\mu \tag{2.8}$$

where k is Boltzmann's constant, and T is temperature in Kelvin. The bandgap of Si also depends on doping as a result of bandgap renormalization; the shift in bandgap can be described empirically as:[107,109]

$$\Delta E_{gap} = -0.0187\left[ln\left(\frac{N_d}{7\times 10^{17}cm^{-3}}\right) + ln\left(\frac{N_a}{7\times 10^{17}cm^{-3}}\right)\right]eV \tag{2.9}$$

which is valid for $|N_d - N_a| > 7\times 10^{17}cm^{-3}$. The bandgap of silicon is thus given as:

$$E_{gap} = E_{gap,0} - \Delta E_{gap} \tag{2.10}$$

where $E_{gap,0}$ is the non-degenerate bandgap of 1.12 eV.

For calculation of the p–n junction characteristics under equilibrium conditions at zero external applied voltage, the built-in potential, ψ_{bi}, is fixed between the Ohmic contacts. In the absence of degenerate doping ($N_a; N_d < 10^{17}$ cm^{-3}), the built-in potential can be represented as:

$$\psi_{bi,0} = \frac{kT}{q}ln\left(\frac{N_a N_d}{n_{i,0}^2}\right) \tag{2.11}$$

where $n_{i,0} = 1.07\times 10^{10}$ cm^{-3} is the intrinsic carrier concentration for non-degenerately doped Si. For the degenerately doped systems considered here, we calculate the intrinsic carrier concentration, n_i, as:

$$n_i = \sqrt{N_c N_v}exp\left(\frac{-E_{gap}}{2kT}\right) \tag{2.12}$$

Where N_c and N_v represent the conduction and valence band density of states with values of 2.86×10^{19} and $2.66x10^{19} cm^{-3}$, respectively, and E_{gap} is the doping-level dependent bandgap given in equation 2.10. For degenerate doping, the standard approximation for the Fermi level, E_F, which assumes E_F is $> 3kT$ from the band edge and is implicit in equation 2.11, substantially deviates from the true value, so we instead use the Joyce-Dixon approximation[110] to estimate the difference between E_F and the band edge:

$$\Delta E_{JD,c} = E_F - E_c = \frac{kT}{q}\left(ln\left(\frac{N_d}{N_c}\right) + \frac{1}{\sqrt{8}}\left(\frac{N_d}{N_c}\right) - \left(\frac{3}{16} - \frac{\sqrt{3}}{9}\right)\left(\frac{N_d}{N_c}\right)^2\right) \quad (2.13)$$

where E_c is the energy of the conduction band edge. An analogous expression can be written for the valence band substituting in N_v, N_a, and E_v, the energy of the valence band edge. Based on this approximation, we introduce a correction term for the built-in voltage as:

$$\Delta E_{correction} = E_{gap,0} + \Delta E_{JD,c} + \Delta E_{JD,v} - \psi_{bi,0} \quad (2.14)$$

We can thus represent the final built-in voltage as:

$$\psi_{bi} = \frac{kT}{q} ln\left(\frac{N_a N_d}{n_{i,a} n_{i,d}}\right) + \Delta E_{correction} + \frac{\Delta E_{gap,0}}{2} \quad (2.15)$$

The potential applied between the Ohmic n-type and p-type contacts, ψ,is given by:

$$\psi = \psi_{bi} + V_{applied} \quad (2.16)$$

where $V_{applied}$ is the external voltage applied to the p-type Ohmic contact such that a positive value represents a forward-biased diode.

To model current–voltage characteristics of the p–n junctions, the recombination term R in equation 2.2 includes Shockley–Read–Hall (SRH)[107,108] as:

$$R_{SRH} = \frac{np - n_i^2}{\tau_n(p + n_i) + \tau_p(n + n_i)} \tag{2.17}$$

where τ_n and τ_p represent the minority carrier lifetimes for electrons and holes, respectively. For all simulations we set these lifetimes equal so that $\tau_n = \tau_p = \tau$. Where noted in the text, the recombination term R also includes Auger recombination[107,108] as:

$$R_{Auger} = \begin{cases} \frac{n(np-n_i^2)}{\tau_{A,n} N_d^2} & for N_d > 5 \times 10^{15} \\ \frac{p(np-n_i^2)}{\tau_{A,p} N_a^2} & for N_a > 5 \times 10^{15} \end{cases} \tag{2.18}$$

where the Auger lifetimes, $\tau_{A,n}$ and $\tau_{A,p}$, are given in the low-injection regime by:[111]

$$\tau_{A,n} = \frac{1}{1.8 \times 10^{-24} cm^{-3} (N_d)^{1.65}} s \tag{2.19}$$

and

$$\tau_{A,p} = \frac{1}{6 \times 10^{-25} cm^{-3} (N_d)^{1.65}} s \tag{2.20}$$

The simulations include surface recombination as a boundary condition on the outer surfaces of the simulation domain excluding the Ohmic contacts. The rate of surface recombination is calculated as:[107,108]

$$R_S = \frac{np - n_i^2}{S_n^{-1}(p + n_i) + S_p^{-1}(n + n_i)} \tag{2.21}$$

where S_n and S_p are the surface recombination velocities of electrons and holes, respectively,

and for all simulations we set $S_n = S_p = S$.

CHAPTER 3: SYNTHETICALLY ENCODING 10 NM MORPHOLOGY IN SILICON NANOWIRES[1]

3.1 Introduction

Most semiconductor technologies rely on the ability to pattern materials with nanometer-scale features using top-down lithographic tools. Over the last decade, however, bottom-up chemical methods to control the size, shape, and composition of nanoscale materials have progressed rapidly, resulting in a diverse set of well-controlled morphologies including dots, rods, ribbons, and wires.[112–114] Semiconductor nanowires (NWs) are recognized as an especially important technological building block because the high aspect ratio can be used for longitudinal transport of electrical or optical signals.[112,113] A variety of devices have been demonstrated, including sensors,[115] waveguides,[116] phase-change memory,[117] light-emitting diodes,[118] and solar cells.[83,119,120] Nevertheless, current NW-based technology has been limited by the material's translational symmetry and the inability to pattern arbitrary, nanometer-scale morphological features.

NWs are typically synthesized using the VLS mechanism,[21] in which a metal nanoparticle catalyzes one-dimensional growth of a single-crystalline semiconductor material. Advancements in VLS-based technologies have generally involved synthesis of new materials or heterostructures.[121] For instance, NW superlattices, in which the composition of a NW is modulated along the growth axis, have been reported for Si/SiGe,[59] GaAs/GaP,[69] InAs/InP,[122,123] Zn-doped InP,[27]

---

[1]This chapter previously appeared as an article in Nano Letters. The original citation is as follows: Christesen, J. D.; Pinion, C. W.; Grumstrup, E. M.; Papanikolas, J. M.; Cahoon, J. F. Synthetically Encoding 10 nm Morphology in Silicon Nanowires. Nano Lett. **2013**, *13*, 6281–6286.

CdSe/ZnSe,[124] and P-doped Si.[125] Modulation of NW composition often results in faceting of the NW surface, providing some capability to control morphology during synthesis.[25,27,98,123] In addition, NW superstructures have been reported in the form of controllably kinked NWs that break the one-dimensional shape.[39,126] Nevertheless, only a handful of reports describe efforts to alter the NW geometry and encode specific morphology. For example, controlled VS over-coating on the NW surface has been used to create tapered structures[127] and periodic variations in morphology.[50] In addition, modulation of the size of the metal catalyst during growth has been shown to provide control over the NW diameter.[91,92] For metal NWs, electrodeposition in metal oxide templates followed by wet-chemical etching has been used to create wires with alternating, nanoscale structures.[99,128] However, a method for accurate, nanometer-scale control of morphology in single-crystalline semiconductor NWs has not been developed. Here, we demonstrate a new method to achieve this type of high-fidelity shape control, a process which we term Encoded Nanowire GRowth and Appearance through VLS and Etching (ENGRAVE). The key aspects and capabilities of this method are illustrated in Figure 3.1 and elaborated below.

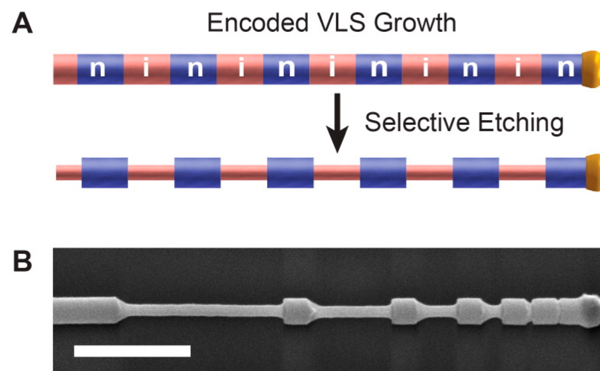

Figure 3.1: Synthesis of Si NWs with encoded morphology. (A) Schematic illustration of NW growth including rapid modulation of P dopant incorporation to form heavily-doped n-type (n) and undoped intrinsic (i) segments that are selectively etched using wet-chemical methods to form a grating. (B) SEM image of a NW grating encoded (from left to right) with sequential intrinsic segments for 200, 100, 50, 25, 10, and 5 s; scale bar, 500 nm.

3.2 Methods

Si NWs were grown by a VLS mechanism in a home-built, hot-wall chemical vapor deposition (CVD) system at 420 °C using Au nanoparticles as catalysts, silane (SiH_4) as the source of Si, and hydrogen (H_2) as the carrier gas (see Chapter 2.1 for details). As illustrated schematically in Figure 3.1A, an additional flow of phosphine (PH_3) was rapidly modulated during growth[125] to encode varying levels of P, an n-type substitutional dopant with high solubility in Si.[129–131] The etch rate of doped Si with aqueous KOH solution is well-known to decrease with higher dopant concentration.[132] This effect has been observed in doped Si NWs, producing changes in diameter along the axis.[66,133] Here, we develop this effect as a tool to encode arbitrary, high-resolution morphology along the NW growth axis, enabling new technological applications of Si NWs.

3.3 Characterization and Optimization of ENGRAVE

To delineate the spatial resolution of the ENGRAVE process, we synthesized NWs with six intrinsic segments encoded along the axis for increasingly short time scales. As shown in Figure 3.1B, wet-chemical etching of these segments yielded an abrupt and conformal reduction in the NW diameter. The largest segment, encoded for 200 s, produced a feature ∼700 nm in length while the smallest segment, encoded for 5 s, produced a feature ∼10 nm in length, defining the lower limit of the spatial resolution for this process. This example also demonstrates that NW growth time is directly proportional to spatial length scale. Quantitative analysis of the NW growth rate yielded a value of 213 ± 6 nm/min, which was used throughout this work to convert growth times to length scales. This rate is comparatively slow because of the low CVD temperature, 420 °C, chosen to minimize radial over-coating and doping of the NW surface, a known problem during Si NW synthesis.[54,134] By minimizing the over-coating, we could encode high-fidelity nanoscale features over macroscopic length scales, as exemplified in Figure 3.2A by the 400 nm-pitch grating encoded over 50 μm of a single NW.

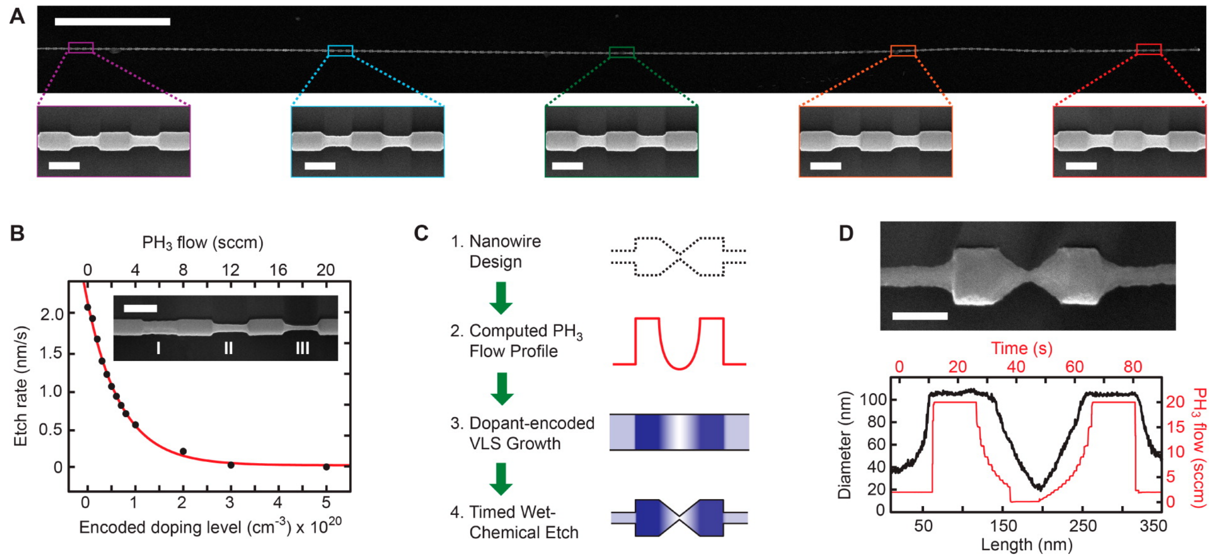

Figure 3.2: Characterization of NW growth, etching, and morphology. (A) Upper: SEM image of a grating-encoded NW more than 50 μm in axial length; scale bar, 5 μm. Lower: Higher magnification SEM images of select sections of the NW in the upper panel; scale bars, 200 nm. (B) Radial etch rate of Si NWs as function of encoded P doping levels. Red curve represents the best fit to a single exponential function. Inset: SEM image of a NW with segments I, II, and III encoded with P doping levels of 1×10^{20} cm^{-3}, 5×10^{19} cm^{-3}, and intrinsic, respectively, and etched for 25 s; scale bar, 200 nm. (C) Schematic of the sequential process for bottom-up synthesis of complex NW morphologies. (D) Upper: SEM image of a NW encoded with a bow-tie; scale bar, 100 nm. Lower: NW diameter (black curve and left-hand axis) as a function of length for the bow-tie shown in upper panel, and measured phosphine flow rate (red curve and right-hand axis) in standard cubic centimeters per minute (sccm) as a function of time during CVD growth.

For the synthesis of NWs with complex morphology, we measured the etch rate of Si NWs encoded with P doping levels ranging from 5.0×10^{20} to less than 1.0×10^{19} dopants/cm^3, as depicted in Figure 3.2B. Note that these doping levels were calculated from the gas-phase ratio of Si to P during CVD growth and the actual values could be lower as a result of incomplete P incorporation.[131] Quantitative evaluation of the etch rate reveals a non-linear dependence on doping level that is well approximated with a single exponential function and varies from 2.1 nm/s for 'intrinsic' segments with doping levels $< 1.0 \times 10^{19}$ cm^{-3} to negligible etching ($<$0.1 nm/s) with heavily doped segments. The exponential dependence is most likely a result of the logarithmic dependence of the Fermi level position on the doping level, which modulates the rate of Si oxidation and dissolution at the semiconductor-solution interface.[132]

The precise calibration of the NW growth and etch rates enables rational design and synthesis of arbitrary high-resolution morphologies, as outlined schematically in Figure 3.2C. This process involves 1) design of the morphological profile, 2) conversion of the physical profile into a dopant profile, 3) VLS growth of the dopant-encoded NW, and 4) wet-chemical etching. As an example, we used this procedure to form the bow-tie structure depicted in Figure 3.2D. The phosphine flow profile for the bow-tie (red curve Figure 3.2D) is complex, requiring over 25 changes in flow rate over a time scale of one minute. The diameter profile (black curve Figure 3.2D) shows the resulting structure to be smoothly tapered with a monotonically decreasing then increasing diameter that reduces to a diameter of $\sim$15 nm at the narrowest point. Note that the phosphine flow profile was modified to be asymmetric around the flow minimum to account for dopants retained by the Au catalyst, a phenomenon termed the reservoir effect.[65]

We used other complex doping profiles to encode the range of morphological features shown in SEM images in Figure 3.33. These structures include periodic (images 1–4) or non-periodic (image 5) gratings, nanogaps with gap sizes as small as 10 nm (images 6–7), suspended nanorods

(image 8), and sinusoidal profiles (images 9–10). These morphologies could each enable a different class of NW-based technology. For instance, the suspended nanorods could be used as mechanical oscillators for nanoelectromechanical systems,[135] periodic gratings for optical applications in nanophotonics.[136] and non-periodic gratings as a method to control thermal transport along the wires, enabling the use of Si as a thermoelectric material.[137,138]

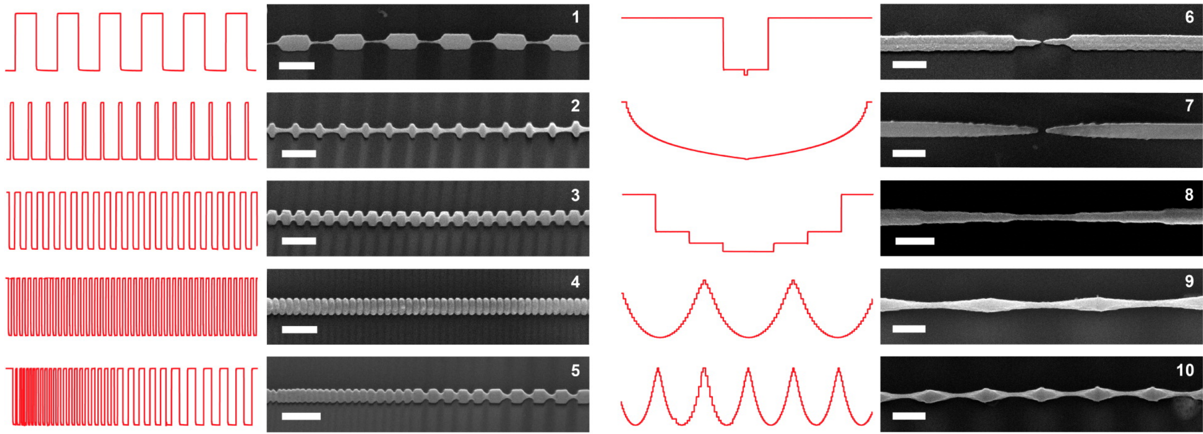

Figure 3.3: SEM images and phosphine flow profiles for the synthesis of Si NWs with complex morphology. The measured phosphine flow profile used to encode the morphology of each segment is depicted in red to the left of each SEM image; all scale bars, 200 nm. The flow rates vary from 0 to 20 sccm for each NW.

As an additional method of morphological control, the ENGRAVE NWs can be thermally oxidized. As shown by SEM images and diameter profiles before and after thermal oxidation (Figure 3.4A and 3.4B), the volumetric expansion of the NW caused by the lattice expansion from Si to SiO_2 results in a broadening of the outer shape. However, the Si core retains its morphology, which can be verified by removing the thermal oxide using a BHF etch (bottom panel in Figure 3.4A). Bright-field TEM imaging of a NW with more extensive thermal oxidation (Figure 3.4C) shows that the center of the NW corresponds to the crystalline Si core, which is surrounded by an oxide shell. It is also possible to completely oxidize the etched regions of the NWs, leaving behind isolated Si segments, ellipsoidal dots, as shown by the lower TEM image in Figure 3.4C. Oxidation of n-type doped Si is also known to drive dopants to the Si/SiO_2

interface due to electrostatic effects combined with the increased diffusion of dopants at elevated temperatures.[137,139–141] Thus, thermal oxidation can also be a route to remove dopants from the NWs, decoupling the connection between doping level, Fermi level, and morphology.

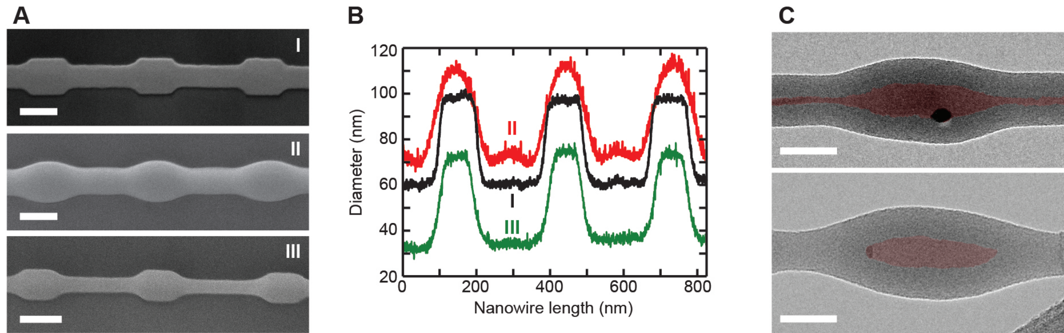

Figure 3.4: Thermal Oxidation of ENGRAVE structures. (A) SEM images of a single ENGRAVE NW before (top; I) and after (middle; II) thermal oxidation and after removal of the thermal oxide (bottom; III): scale bars, 100 nm. (B) Diameter profiles derived from the SEM images in panel A before (black; I) and after (red; II) thermal oxidation and after removal of the thermal oxide (green; III). (C) False-colored TEM images of etched NWs after thermal oxidation, in which the entire Si core (shaded red) retains its morphology (top) or the intrinsic segments are fully oxidized (bottom) leaving an ellipsoidal Si nanodot (shaded red): scale bars, 50 nm. Reprinted with permission from Christesen, J. D., Pinion, C. W., Hill, D. J., Kim, S. & Cahoon, J. F. Chemically Engraving Semiconductor Nanowires: Using Three-Dimensional Nanoscale Morphology to Encode Functionality from the Bottom Up. J. Phys. Chem. Lett. **2016**, *7*, 685–692. Copyright 2015 American Chemical Society.

3.4 Applications

Field-enhanced spectroscopies, such as surface–enhanced Raman spectroscopy (SERS), are often performed using Noble metal nanostructures that support SPPs.[142] Through careful design of the shape of a nanostructure, SPP resonances can be used to confine and amplify incident electromagnetic fields at specific wavelengths and spatial positions.[143] Following the procedure depicted in Figure 3.5A, we used nanogap-encoded NWs as the topological templates for Noble metal films, creating Si/Au nanostructures with tunable SPP resonances.[2] As shown by the SEM images in Figure 3.5B, deposition of ∼50 nm of Au on the NWs by physical vapor deposition

[2]Simulations and experiments performed for both surface-enhanced Raman spectroscopy and memory applications were performed by Christopher Pinion.

preserved the high-resolution structures and nanogap morphology. We used finite-element optical simulations (see Figure 3.5C) to design Si/Au ENGRAVE structures with specific SPP characteristics. The NWs behave as plasmonic resonator antennas,[144] in which the length of the segments adjacent to the gap control the field enhancement as a result of constructive or destructive interference of the SPP wave along the NW axis.[145,146] For a wavelength of 633 nm, we found that segments ∼775 nm in length were on-resonance, producing intense fields in the gap, while segments ∼1175 nm in length were off-resonance, exhibiting weaker field enhancement. As proof-of-concept, we performed SERS imaging on the Si/Au NWs coated with methylene blue.[145,146] We observed a greater than ten-fold Raman signal enhancement from the on-resonance structure, as shown by the spectra in Figure 3.5D. In addition, Raman imaging (see Figure 3.5E) confirmed that the signal enhancement is localized to a narrow spatial region around the gap. In comparison, the off-resonance NW shows a weak Raman signal arising from both the gap and the two ends of the rods, a result that is in good agreement with the optical simulations in Figure 3.5C. These results highlight the capability for ENGRAVE to serve as a simple route to create nanoplasmonic structures with tunable resonances for field-enhanced spectroscopy[138] and nanophotonic technologies.[143]

As a second application of ENGRAVE, we fabricated core/shell Si/SiO_2 nanorod-encoded devices for use as resistive switches in non-volatile memory.[117,147,148] The fabrication steps are illustrated in Figure 3.6A. First, an n-type/intrinsic/n-type NW was synthesized with a 50 nm intrinsic channel.[2] Second, the channel was etched to a diameter of ∼30 nm to produce a suspended nanorod, and third the wire was thermally oxidized to create a ∼10 nm diameter Si core encased by an oxide shell. Fourth, electrical contacts were fabricated to the two n-type segments adjacent to the intrinsic channel, as shown by the SEM image in Figure 3.6B. Device simulations[149] (see Figure 3.6C) indicate that this geometry concentrates the voltage drop and

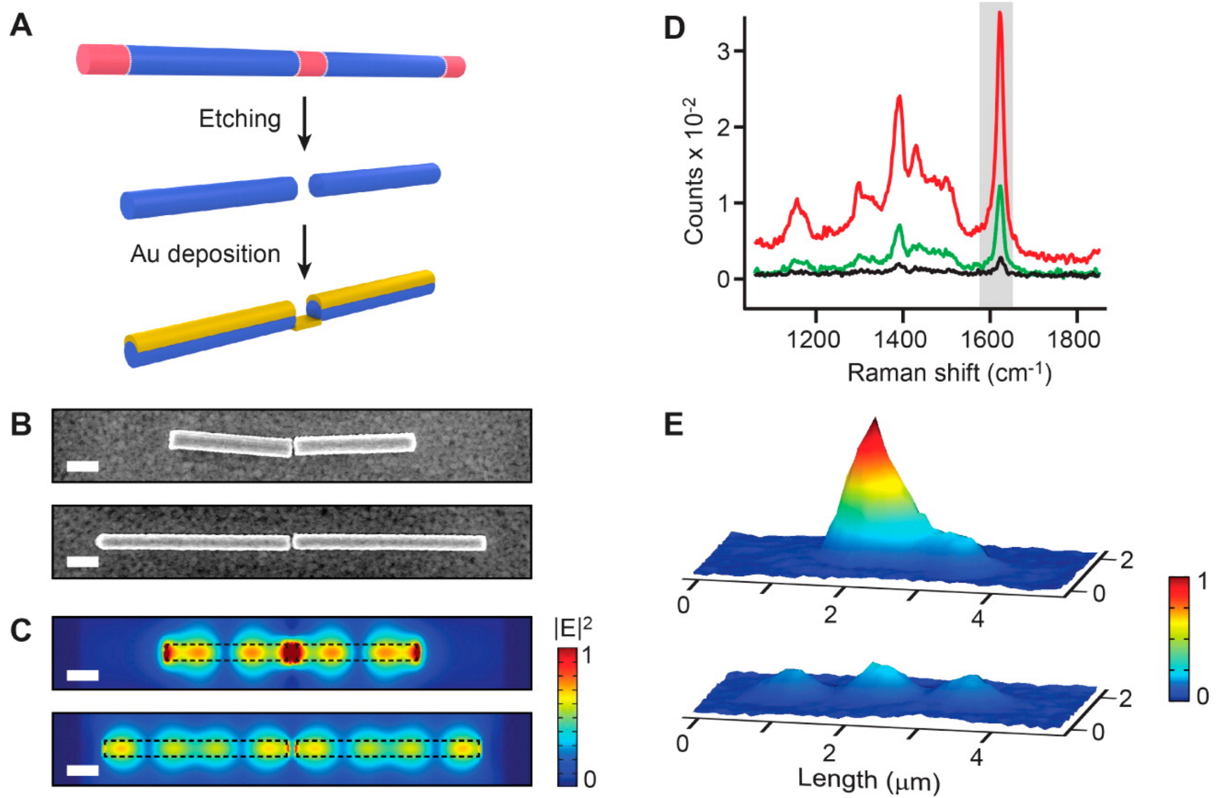

Figure 3.5: Nanogap-encoded NWs for plasmonics. (A) Schematic illustration of Au deposition on a nanogap-encoded NW. (B) SEM images of nanogap-encoded Si NWs with 50 nm Au, gaps of ∼30 nm, and segment lengths of ∼775 nm (upper image) and ∼1175 nm (lower image); scale bars, 200 nm. (C) Finite-element optical simulations of the Si/Au nanogap structures depicted in panel B showing the scattered field ($|E|^2$) in the plane above the NW resulting from illumination at normal incidence with a transverse-magnetic plane wave at 633 nm. The optically excited SPP mode is on-resonance and off-resonance in the upper and lower images, respectively; scale bars, 200 nm. (D) Raman spectra of methylene blue collected from the planar Au film (black), the off-resonance NW (green), and on-resonance NW (red). The shaded region denotes the spectral range used to generate spatial maps of the Raman intensity. (E) Three-dimensional spatial maps of the relative Raman signal intensity generated by raster scanning a 633 nm laser over on- and off-resonance nanogap-encoded Si/Au structures with segment lengths of ∼775 nm (upper) and ∼1175 nm (lower), respectively.

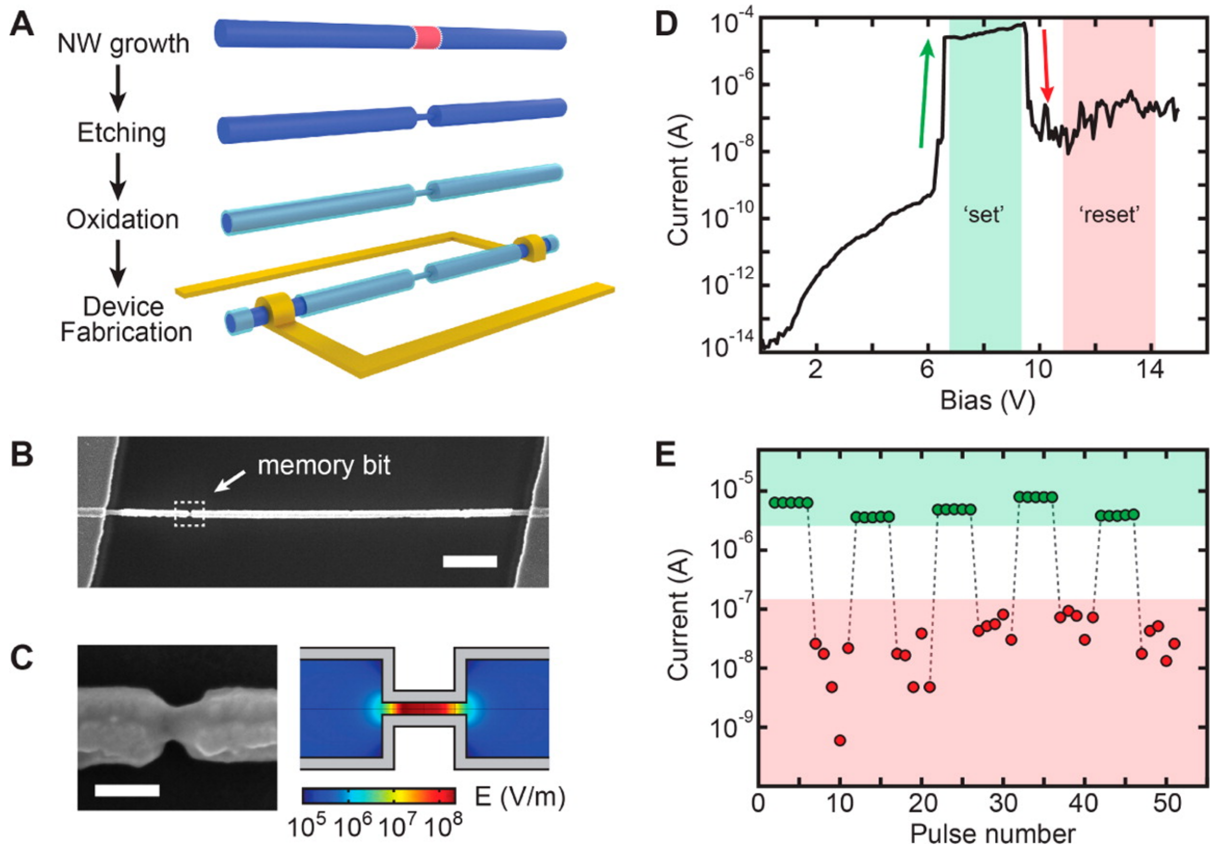

Figure 3.6: Nanorod-encoded NWs for non-volatile memory. (A) Schematic illustration of the sequential process used to fabricate a non-volatile memory bit. (B) SEM image of a NW device encoded with a non-volatile memory bit (dashed box) showing Ti/Pd Ohmic contacts on the far left and right; scale bar, 1 m. (C) Left: SEM image of the encoded memory bit corresponding to the dashed white box in panel B; scale bar, 100 nm. Right: finite-element simulation of the electric field magnitude across the NW at an applied bias of +8 V plotted in a logarithmic color scale for a nanorod segment 50 nm in length and 10 nm in diameter. (D) Characteristic switching I–V curve for an ENGRAVE NW memory device. The shaded green and red regions define the 'set' and 'reset' bias ranges, respectively. (E) Resistive switching behavior over ten memory cycles. Dashed lines represent the 'set'/'reset' pulses between current readings, which were acquired five times at 1 V between each 'set' or 'reset' pulse.

electric field within the narrow channel region, enabling a resistive switching effect as observed in a planar Si/SiO_2 system.[146,147] Initial current–voltage (I–V) measurements showed an Ohmic response from the device with a resistance of 54.7 kΩ, indicating the presence of a thin Si filament encapsulated by the SiO_2 shell. After an electroforming process consisting of multiple I–V sweeps at high bias (see Chapter 2.5 for details), the device converged to the characteristic "switching" I–V behavior (see Figure 3.6D) expected from a Si/SiO_2 system.[146,147] The I–V curve exhibits a low voltage region that "sets" the device to a low resistance state and a high voltage region that "resets" the device to a high resistance state. In the latter state, we observe variations in the current (see Figure 3.6D,E) similar to those reported previously in Si/SiO_2 resistive switching memory devices and attributed to tunneling current fluctuations.[147]

To use the nanorod-encoded device as non-volatile memory, we applied sequential "set" and "reset" voltage pulses (100 s) of 8 V and 12 V, respectively, to reversibly change the resistance of the device. As shown in Figure 3.6E, we cycled the NW device through ten memory states and achieved on/off current ratios of nearly 10^2. With further development, we expect that at least 100 memory bits could be encoded on a single NW and lower voltage operation achieved with smaller nanorod segments. These initial results demonstrate the facile integration of ENGRAVE structures in electronic devices and furthermore highlight the emergent electronic characteristics that can be encoded through morphology.

3.5 Conclusion

In summary, we have demonstrated a method, termed ENGRAVE, to encode high-resolution morphology along the growth axis of Si NWs. We anticipate this process will be extended to other NW materials, such as GaAs/GaP[94,150] et al., that can be selectively etched with gas-phase or wet-chemical techniques and will represent a general route to encode new functionality in semiconductor NWs.

CHAPTER 4: ENCODING ABRUPT AND UNIFORM DOPANT PROFILES IN VAPOR–LIQUID–SOLID NANOWIRES BY SUPPRESSING THE RESERVOIR EFFECT OF THE LIQUID CATALYST[1]

4.1 Introduction

Semiconductor NWs have been developed as a bottom-up technological platform for a variety of electronic,[129,151] photonic,[73,152,153] and photovoltaic[119,154–156] devices. Several of these technologies require modulation of the NW composition along the growth axis to form heterostructures that are required for specific device functions. For instance, NWs with n-type/intrinsic or p-type/intrinsic junctions have been explored as field-effect transistors, enabling both electronic devices[125,129,157] and sensors.[66,158,159] Similarly, NWs with p-type/n-type junctions have been synthesized in Si,[69,85,133,149,159] GaAs,[69] InP,[160] etc, and used for photovoltaic devices,[69,133,149] avalanche photodetectors,[85] Esaki diodes,[161,162] and light-emitting diodes.[76,163] Nevertheless, it is generally believed that heterostructures formed by the VLS process will have broad junctions with a width approximately equal to the wire diameter.[58,63,164] Considering the wide-ranging applications for NW heterostructures, it is increasingly important to understand the microscopic kinetic processes that govern heterostructure formation and to develop methods that overcome the limitations on the transition width.

During the VLS process (Figure 4.1A),[165,166] a liquid droplet composed of metal and semiconductor is formed by supplying a vapor-phase semiconductor precursor (e.g. SiH_4 and GeH_4) to a metal nanoparticle and raising the local temperature above the eutectic point for the two materi-

[1]Reprinted with permission from Christesen, J. D.; Pinion, C. W.; Zhang, X.; McBride, J. R.; Cahoon, J. F. Encoding Abrupt and Uniform Dopant Profiles in Vapor–Liquid–Solid Nanowires by Suppressing the Reservoir Effect of the Liquid Catalyst. ACS Nano **2014**, *8*, 11790–11798. Copyright 2014 American Chemical Society

als. When the liquid droplet is supersaturated, which typically requires semiconductor weight fractions of 10-50%,[64,167] a NW will nucleate and grow. Heterostructures are formed by altering the supply of vapor-phase precursors during VLS growth. However, the liquid droplet can act as a reservoir of material even after a precursor has been removed, causing the heterojunction to be broadened by a phenomena termed the "reservoir effect," as illustrated in Figure 4.1B,C.[65,67,96] This effect has been observed for heterostructures involving a change in dopants (e.g. P-doped Si[52] and Si-doped GaAs[57]) and structures involving a change in semiconductor (e.g. Si/Ge[58–60] and GaAs/InAs[61,62]) and has been described previously.

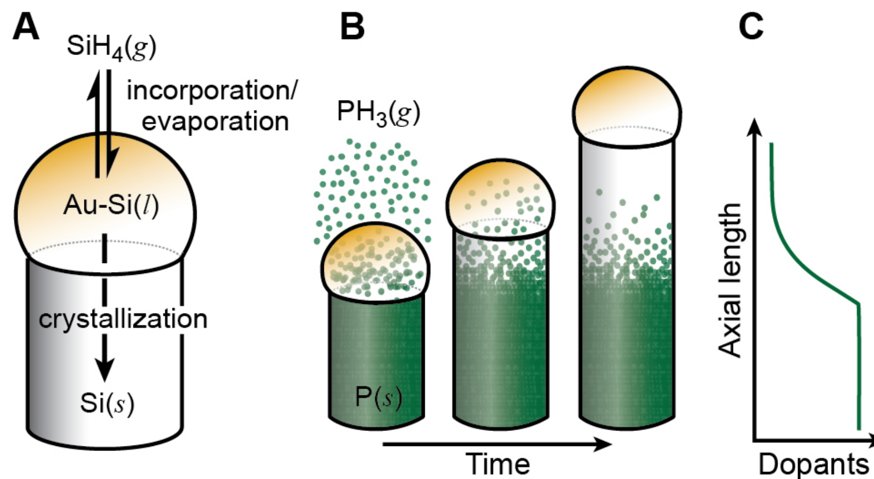

Figure 4.1: VLS NW growth and the reservoir effect. (A) Illustration of the key kinetic processes during Si NW growth: incorporation, evaporation, and crystallization. (B) Schematic of the reservoir effect, showing (left) a supply of P dopant precursor in the gas phase followed by (middle) removal of the gas-phase precursor with retention of P by the liquid catalyst and (right) subsequent depletion of P dopants from the liquid catalyst. (C) A plot of dopant concentration along the axial length of the NW.

Here, we investigate the uniformity and abruptness of P dopant transitions in Si NWs grown by the VLS mechanism with Au catalysts. Transitions between n-type and intrinsic sections of the Si NW are quantitatively evaluated by elemental mapping with ∼1 nm spatial resolution using EDS in a STEM. Previous attempts to quantitatively resolve dopants in NWs have been hindered by low signal-to-noise ratios and long acquisition times;[66,81] however, this problem is

mitigated by the simultaneous x-ray detection of four solid-state detectors in conjunction with the high-brightness Schottky-type field-emission gun of the STEM used in this work (FEI Tecnai Osiris; see Chapter 2.3.2). The transitions are also evaluated by wet-chemical etching of doped NWs using the recently reported ENGRAVE process.[168] We develop a kinetic model of NW doping, which includes the microscopic processes of (1) P incorporation into the liquid catalyst, (2) P evaporation from the catalyst, and (3) P crystallization in the Si NW. We find a VLS growth regime in which the reservoir effect is fully suppressed because the rate of P evaporation greatly exceeds the rate of P crystallization. In this regime, NWs with diameters from 50 nm to 150 nm are encoded with abrupt and uniform dopant transitions, as verified by high-resolution morphologies encoded through the ENGRAVE process. The results suggest that the reservoir effect can be suppressed for any VLS growth system in which the rate of liquid-vapor equilibrium can greatly exceed the rate of NW growth.

4.2 Results

Si NWs were synthesized in a hot-wall CVD reactor at 420 °C and a range of total pressures (20-80 Torr) using SiH_4 and PH_3 as the Si and P precursors, respectively, and H_2 as the carrier gas (see Chapter 2.1 for further details). Calibration of the NW growth rate, as described previously,[166] enabled the growth of n-type and intrinsic sections with precise axial lengths by modulating the flow of PH_3 for specific time intervals. EDS images in Figure 4.2A for NWs grown at 20 Torr show strong P signals from the doped sections and relatively abrupt transitions at the n-type/intrinsic interfaces, which will be analyzed in detail below. Wet-chemical etching of the NWs in KOH solution, as detailed in Chapter 2.2, leads to diameter modulation along the axis, as shown by the SEM image in Figure 4.2A. The large diameter segments correspond to the n-type sections, which act as an etch stop as described previously for the ENGRAVE process.[168] As shown in Figure 4.2B, the EDS and SEM diameter measurements directly correlate with the

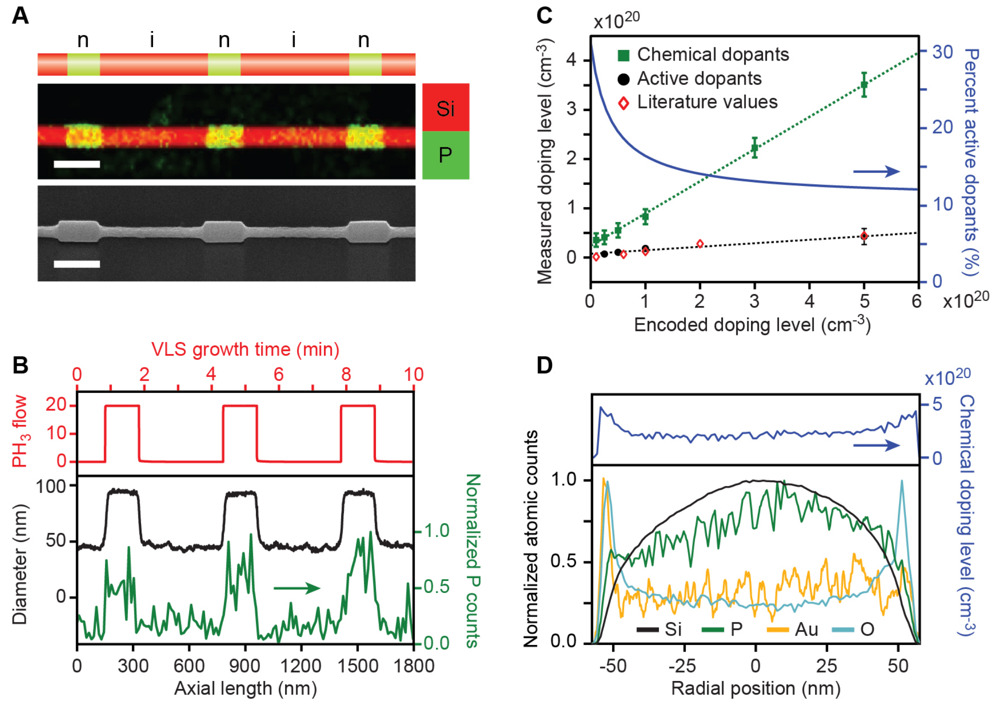

Figure 4.2: Characterization of P doping in VLS-grown Si NWs. (A) Top: Schematic of a Si NW with intrinsic (i) sections depicted in red and P-doped, n-type (n) sections depicted in green. Middle: STEM EDS image of a Si NW showing P counts in green and Si counts in red; scale bar, 200 nm. Bottom: SEM image of Si NW after wet-chemical KOH etching; scale bar, 200 nm. (B) Top: PH_3 flow profile (in units of standard cubic centimeters per minute, sccm) during VLS growth of the NWs shown in panel A. Bottom: Diameter profile (black curve and left-hand axis) derived from the SEM image in panel A and P signal (green curve and right-hand axis) derived from the EDS image in panel A. (C) Active doping level from resistivity measurements (black circles) and chemical doping level from EDS measurements (green squares) as a function of the encoded doping level, which corresponds to the gas-phase ratio of P to Si. Literature values for active doping level from reference 42 are shown as red diamonds, and dashed lines represent linear fits to the data. Blue line and right-hand axis show the percentage of active dopants based on the ratio of active to chemical doping level. (D) Top: chemical doping level as a function of radial position for a NW with encoded doping level of 5×10^{20} cm^{-3}. Bottom: Normalized EDS signals as a function of radial position for Si (black), P (green), Au (gold), and O (light blue). Chemical doping level in the top panel is determined by the ratio of the P to Si EDS signals. All NWs shown in panels A–D were grown with a SiH4 partial pressure of 0.4 Torr and a total pressure of 40 Torr.

PH_3 flow profile. Both measurements reflect dopant incorporation in the wire and are used to evaluate the abruptness of the n-type/intrinsic junctions.

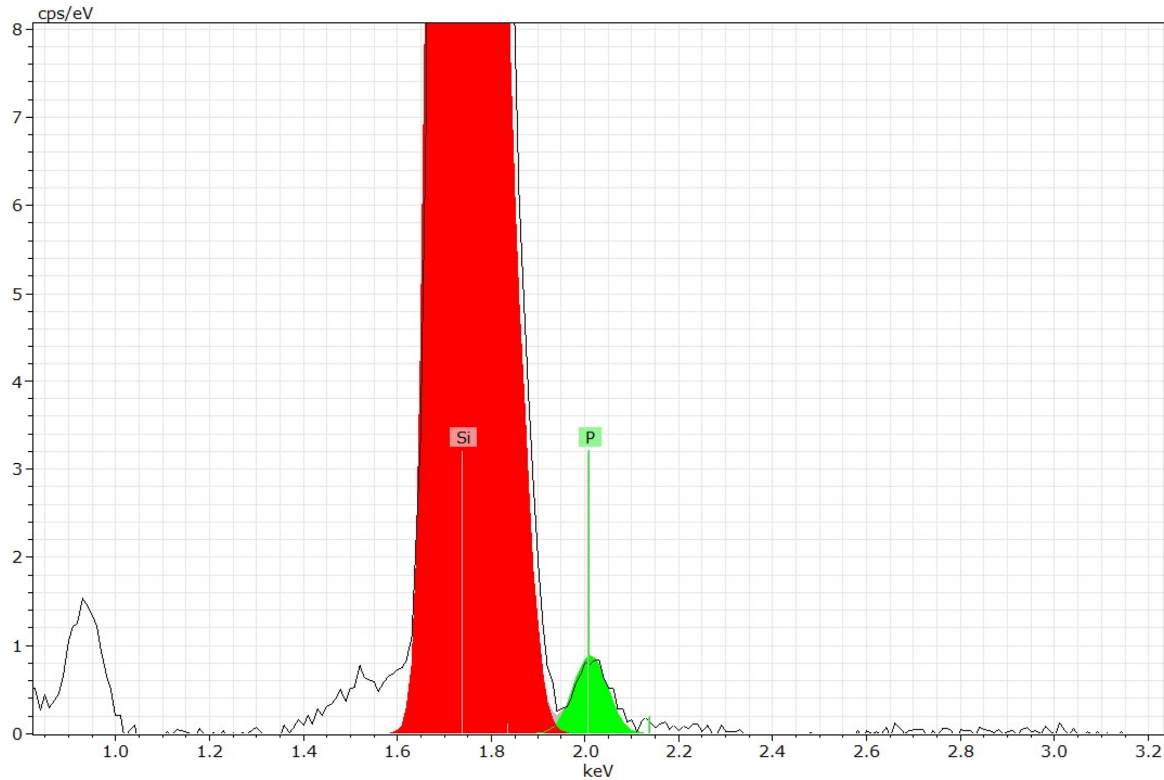

Figure 4.3: Fit of the EDS spectrum. An example spectrum that was used to determine the relative concentration of Si and P to calculate the chemical doping level.

The doping level of the n-type sections was evaluated using both quantitative EDS signal analysis and single-NW resistivity measurements to determine the chemical doping level (i.e. the density of P atoms) and the active doping level (i.e. the density of ionized P atoms), respectively. The nominal encoded doping level, as determined by the vapor-phase ratio of PH_3 to SiH_4, ranged 5×10^{20} cm^{-3} (1:100 PH_3:SiH_4) to 1×10^{19} cm^{-3} (1:5000 PH_3:SiH_4). As shown in Figure 4.2C, EDS analysis (see Figure 4.3 for a representative fit of an EDS spectrum) yielded chemical doping levels that were ∼60% of the nominal encoded level. Resistivity measurements, however, yielded active doping levels (see Figure 4.2C) that were ∼10% of the encoded doping level (see Figure 4.4, Table 4.1, and Chapter 2.4.5 for details on the resistivity measurements).

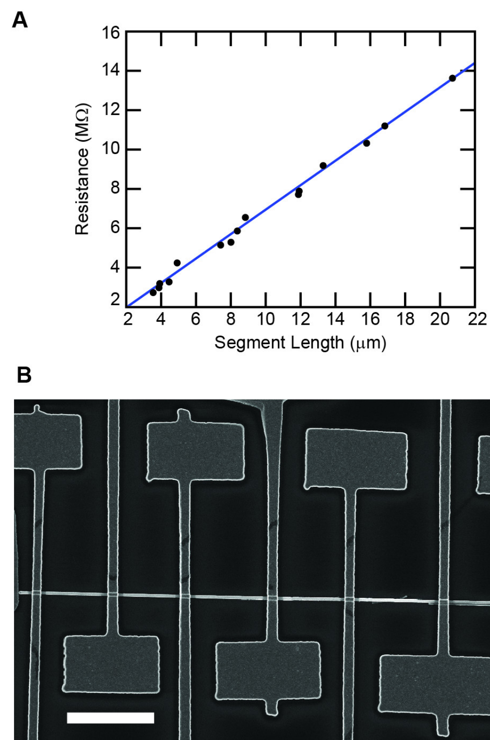

Figure 4.4: n-type Si NW resistivity measurements. (A) A sample plot of resistance vs. contact separation used to extract resistivity. (B) SEM image of NW used to collect the plot in A; scale bar, 5 μm.

The resistivity measurements are in good agreement with previous reports on NW doping with PH_3.[130,131,169] However, a comparison of the chemical and active doping level measurements (right-hand axis of Figure 4.2C) indicates that less than 13% of the dopants in the NW are ionized and thus active for the highest doping levels, and less than 30% are active at the lowest doping level. Although donor deactivation has been reported in silicon nanostructures as a result of dielectric mismatch with the surrounding medium,[170] the magnitude of the deactivation determined here for NWs that are ~100 nm in diameter is not well explained by this effect. Instead, the deactivation is likely due to lattice distortions and/or the formation of P dimers at the relatively low temperature (420 °C) used for VLS growth.[171]

Encoded Doping Level (cm^{-3})	Resistivity (Ω/cm)	Measured Doping Level (cm^{-3})
5.0×10^{20}	1.75×10^{-2}	1.69×10^{18}
5.0×10^{20}	1.21×10^{-3}	5.98×10^{19}
5.0×10^{20}	2.50×10^{-3}	2.74×10^{19}
5.0×10^{20}	1.72×10^{-3}	4.09×10^{19}
1.0×10^{20}	4.29×10^{-3}	1.48×10^{19}
1.0×10^{20}	3.09×10^{-3}	2.16×10^{19}
5.0×10^{19}	3.42×10^{-3}	1.93×10^{19}
5.0×10^{19}	7.27×10^{-3}	7.39×10^{18}
5.0×10^{19}	5.10×10^{-3}	1.19×10^{19}
5.0×10^{19}	1.06×10^{-2}	4.12×10^{18}
2.5×10^{19}	8.86×10^{-3}	5.49×10^{18}
2.5×10^{19}	7.33×10^{-3}	7.30×10^{18}
2.5×10^{19}	5.45×10^{-3}	1.10×10^{19}
2.5×10^{19}	7.95×10^{-3}	6.48×10^{18}
2.5×10^{19}	9.47×10^{-3}	4.94×10^{18}
2.5×10^{19}	8.39×10^{-3}	5.98×10^{18}

Table 4.1: Encoded doping levels and measured active doping levels. Measured resistivity values were converted into active doping levels using the resistivity of bulk Si as a function of P doping level.[172]

The uniformity of doping in the n-type sections was evaluated with radial EDS scans for Si, P, Au, and O, as shown in Figure 4.2D (see Figure 4.5 for additional details on the radial

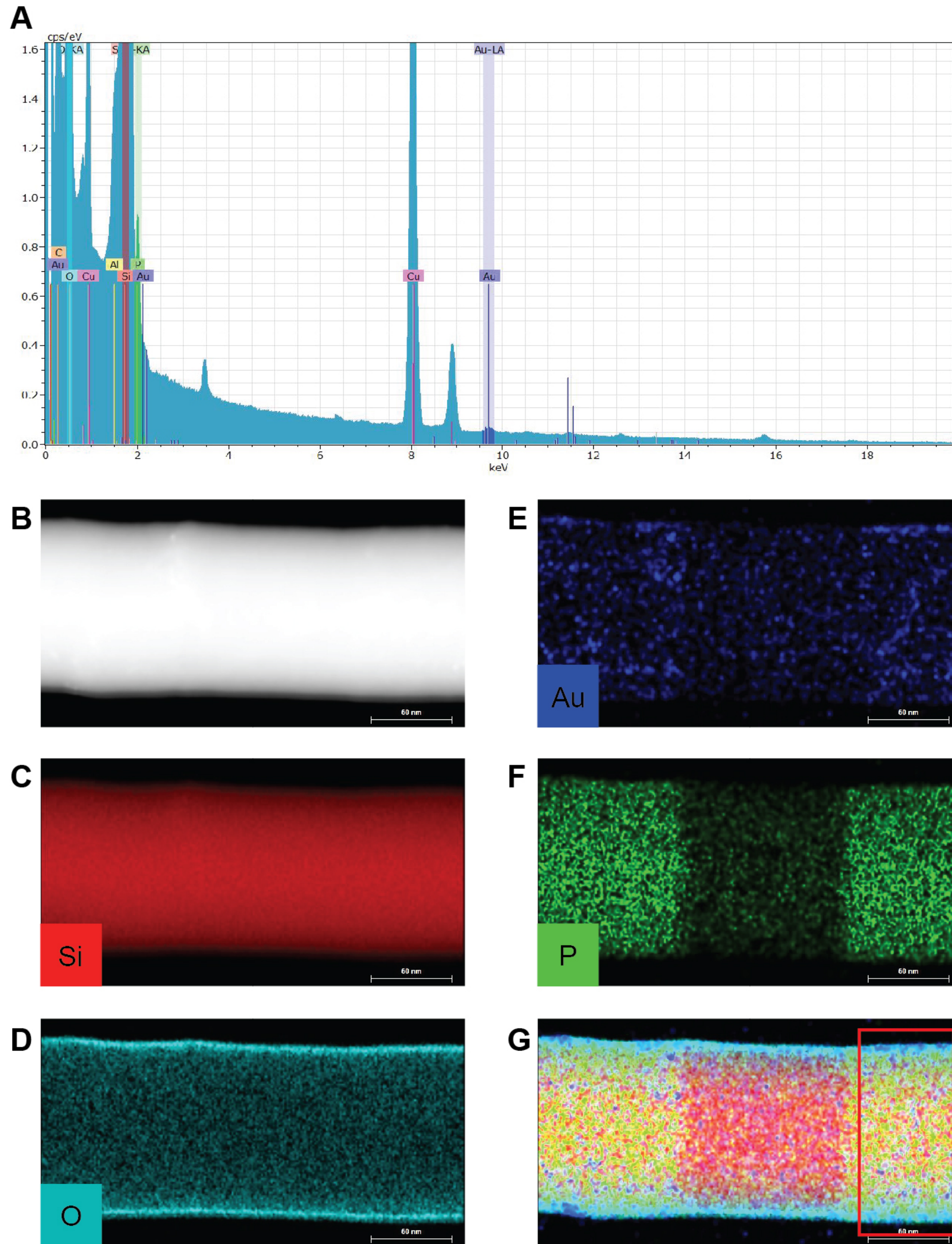

Figure 4.5: EDS spectrum, HAADF-STEM image, and EDS elemental images of a ntype/intrinsic/n-type segment. (A) Spectrum obtained from the data used to generate the radial profile in Figure 4.7D, showing the binned areas for each element. (B) HAADF-STEM image of the NW segment. (C–G) EDS maps of Si (red; panel C), O (light blue; panel D), Au (dark blue; panel E), and P (green; panel F). A composite image overlaying all elements is shown in panel G, and the radial profile in Figure 4.2D corresponds to horizontal averaging within the red boxed region.

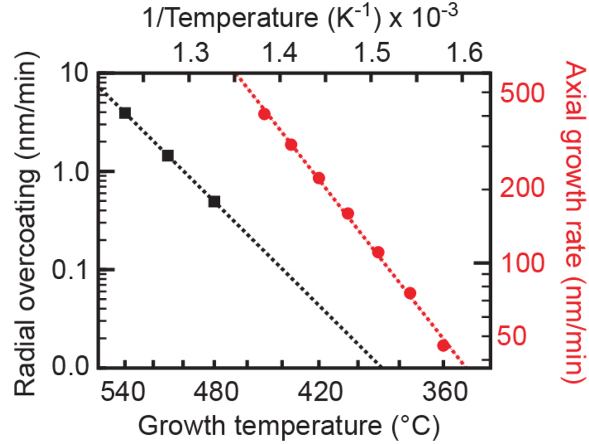

Figure 4.6: Arrhenius plot for VLS growth and VS overcoating. Logarithmic plot of the axial VLS NW growth rate (red circles and right-hand axis) and the radial VS overcoating rate (black squares and left-hand axis) as a function of inverse temperature. Dashed lines represent the best fit to the Arrhenius expression, yielding activation energies of 22 ± 2 kcal/mol and 42 ± 3 kcal/mol for VLS growth and VS overcoating, respectively. At a VLS growth temperature of 420 °C, the VS overcoating rate is less than 0.05 nm/min, but the VLS growth rate is still high because of the nearly two-fold difference in activation energy for the two processes. Error bars are comparable in size to the marker symbols and were omitted for clarity

scan). A plot of chemical doping level vs. radial position (see right-hand axis of Figure 4.2D) shows an increase in the P concentration toward the outer radial positions of the NW. An increasing P concentration toward the surface of the NW is in good agreement with previous studies, which have reported a high surface concentration of P due to VS overcoating[52,54] or from other surface-related effects. However, due to differences in the activation energies between VLS and VS processes, the degree of VS overcoating can be limited by growing the NWs at lower temperatures (e.g. 420 °C; See Figure 4.6). Nevertheless, the region of higher doping also corresponds to the region with higher O counts because of a native oxide on the wire surface. As a result, we expect this region is readily removed when wires are wet-chemically etched to remove the oxide, so electronic devices and the ENGRAVE process[168] should not be substantially affected by this layer. We also note that the radial dependence of the P signal may be overestimated as a result of spectral overlap of an x-ray peak from Au with the peak from P because the wires also show aggregation of Au on the wire surface (see Figure 4.5).

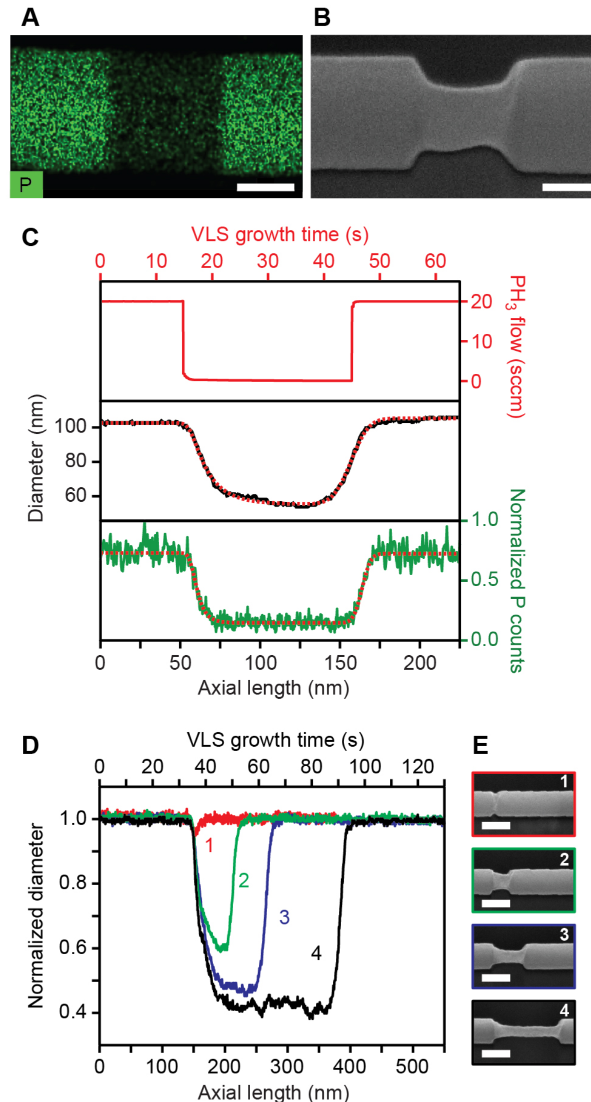

Figure 4.7: Evaluating the abruptness of P dopant profiles in Si NWs. (A) EDS image, showing P counts in green, for an n-type/intrinsic/n-type wire with a ∼100 nm intrinsic section; scale bar, 50 nm. (B) SEM image of a NW, grown under the same conditions as in panel A, after wet-chemical KOH etching; scale bar, 50 nm. (C) Top: PH_3 flow profile (red curve) in units of sccm for the n-type/intrinsic/n-type sections shown in panels A and B. Middle: diameter profile (black curve) derived from the SEM image in panel B and best fit (red dashed line) to equation 2.1. Bottom: P counts (green curve) derived from the EDS image in panel A and best fit (red dashed line) to equation 2.1. (D) Normalized diameter profiles for etched segments along a single NW corresponding to intrinsic segments grown for (1) 6 s (red), (2) 15 s (green), (3) 30 s (blue), and (4) 60 s (black). (E) SEM images of the four segments corresponding to the diameter profiles in panel D. All NWs shown in panels A–E were grown with a SiH_4 partial pressure of 0.4 Torr and a total pressure of 40 Torr.

High-resolution EDS and SEM imaging, as shown in Figure 4.7A and B, was used to quantify the abruptness of the n-type/intrinsic transitions. Line profiles generated from vertical sectioning of the images are displayed in Figure 4.7C. These profiles were fit to single-exponential functions convoluted with a Gaussian (equation 2.1) to extract the characteristic decay length, λ, of the transitions. The Gaussian convolution represents experimental broadening due to mass transport of etchant for SEM images and represents the finite beam size for EDS imaging (see Chapter 2.3.3 for details). The fits (dashed lines in Figure 4.7C) provide a reasonable representation of the transition widths, and the SEM data is also corrected (see Chapter 2.3.3) for the exponential relationship[132,168] between the etch rate and encoded doping level. This analysis yields a measured transition length of 4 nm and 5 nm from the EDS and SEM data, respectively, in Figure 4.7C, demonstrating the good agreement between these two methods. The measured transition widths are substantially shorter than previous reports,[58,164] and we develop below a kinetic model of NW doping in order to interpret the results. Note that for n-type/intrinsic/n-type sections, there is no apparent dependence of the transition width on intrinsic segment length. Diameter profiles and SEM images in Figure 4.7D and 3E show the same profile for intrinsic segments 10 nm to 200 nm in length; however, the smaller segments are etched to a lesser extent presumably because mass transport to the etched region is hindered by the small dimensions. In addition, the first transition region (n-type/intrinsic) shows the same abruptness ($<$10 nm) as the second transition (intrinsic/n-type).

4.3 Kinetic Modeling and Analysis

We analyze P dopant incorporation in Si NWs using the three microscopic kinetic processes depicted in Figure 4.9A: P incorporation, P evaporation, and P crystallization.[173] By analyzing the rate equations, we can construct a kinetic model of NW growth that predicts the transition width for a set of physically reasonable assumptions. First, we assume the engineering of the

CVD system, such as switching speed of the mass flow controllers and rate of gas exchange in the system, has no influence on the observed transition width, which is verified by control growth studies (see Figure 4.8). Second, we assume the NW growth rate is independent of the concentration of vapor-phase PH_3 or P dissolved in the liquid, which is supported by our previous studies of VLS growth kinetics.[166] Third, we assume that prior to a transition, the dopant has reached a steady-state concentration and is uniformly distributed in the liquid catalyst, which is confirmed by the homogeneity of the P signal in Figure 4.2. Note that the kinetic analysis below is used to interpret the transition width of n-type/intrinsic transitions but not intrinsic/n-type transitions. For the latter transitions, in which the n-type region is grown after the intrinsic region, an abrupt, sub-10 nm transition is consistently observed. We attribute this abruptness to a uniformly high rate of P incorporation under all VLS growth conditions.

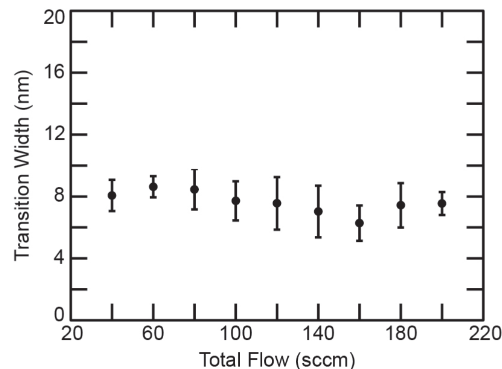

Figure 4.8: Transition width at various carrier gas flow rates with a constant NW growth rate. The H_2 carrier gas flow rate was altered while maintaining a constant total reactor pressure of 40 Torr. The flow rate of SiH_4 was adjusted to maintain the same partial pressure of SiH_4 and thus the same NW growth rate under all conditions.

For the kinetic analysis of n-type/intrinsic transitions, we define the doping level, N_d, as the ratio of the volumetric rate of P crystallization to volumetric rate of Si crystallization:

$$N_d = \frac{k_{PC} C_{P(l)} \pi r^2 \Omega_P}{k_{SiC} C_{Si(l)} \pi r^2 \Omega_{Si}} \approx \frac{k_{PC} C_{P(l)}}{k_{SiC} C_{Si(l)}} \tag{4.1}$$

where k_{PC} is the rate constant for P crystallization (units of nm/s), k_{SiC} is the rate constant for Si crystallization (units of nm/s), $C_{P(l)}$ is the concentration of P in the liquid catalyst, $C_{Si(l)}$ is the concentration of Si in the liquid catalyst, r is the radius of the solid NW, and Ω_{Si} and Ω_P are the Si and P volumes per atom, respectively. We also assume $\Omega_{Si} \sim \Omega_P$, leading to the simplification shown on the right-hand side of equation 4.1. During an n-type/intrinsic transition, the dopant width is dictated by the time-dependence of $C_{P(l)}$, which decreases as a result of P crystallization and evaporation as:

$$\frac{dC_{P(l)}}{dt} = -k_{PE} C_{P(l)} \frac{S}{V} - k_{PC} C_{P(l)} \frac{A}{V} \tag{4.2}$$

where k_{PE} is the rate constant for P evaporation (units of nm/s), S is the liquid-vapor interfacial surface area, V is the volume of the liquid catalyst, and A is the cross-sectional area of the NW (equal to r^2). Solving equation 4.2 for $C_{P(l)}$ and inserting the result into equation 4.1 assuming a partial sphere geometry for the liquid catalyst yields:

$$N_d(t) = \frac{k_{PC} C_{o,P(l)}}{k_{SiC} C_{Si(l)}} \exp\left(\frac{-3\left(2Rk_{PE} + \frac{r^2}{R+\alpha} k_{PC}\right)}{(R+\alpha)(2R-\alpha)} t \right) \tag{4.3}$$

where $C_{o,P(l)}$ is the initial concentration of P in the metal catalyst, R is the liquid catalyst diameter, α is $\sqrt{R^2 - r^2}$, and t is the total amount of time after the P precursor has been turned off. The growth rate, G, of the NW, as developed previously, is:

$$G = \frac{L}{t} = \Omega_{Si} k_{SiC} C_{Si(l)} \tag{4.4}$$

where L is the length of the segment grown in time t. Note that the rate constant, k_{SiC}, as used here is the observed rate constant for Si crystallization in a kinetic analysis that does not explicitly consider the process of Si dissolution from the solid Si NW. As a result, the rate constant must have a weak dependence on supersaturation of the liquid Au–Si droplet thus on the supply of Si precursor (e.g. partial pressure of SiH_4).[166] Rearranging equation 4.4 and substituting for t in equation 4.3 yields:

$$N_d(L) = \frac{k_{PC} C_{o,P(l)}}{k_{SiC} C_{Si(l)}} \exp\left(\frac{-3\left(2Rk_{PE} + \frac{r^2}{R+\alpha} k_{PC}\right)}{(R+\alpha)(2R-\alpha) k_{SiC} \varphi_{Si}} L \right) = \frac{k_{PC} C_{o,P(l)}}{k_{SiC} C_{Si(l)}} \exp\left(\frac{L}{\lambda}\right) \tag{4.5}$$

where $\varphi_{Si} = \Omega_{Si} C_{Si(l)}$ is the volume fraction of Si in the liquid catalyst, and the transition width, λ, is defined as:

$$\lambda = \frac{(R+\alpha)(2R-\alpha) k_{SiC} \varphi_{Si}}{3\left(2Rk_{PE} + \frac{r^2}{R+\alpha} k_{PC}\right)} \approx \frac{k_{SiC} \varphi_{Si}}{3(2k_{PE} + k_{PC})} R \tag{4.6}$$

If the catalyst droplet is assumed to be a hemisphere, then $R = r$, α is zero, and the transition width is linearly dependent on the NW radius, as shown on the right-hand side of equation 4.6.[58,164] However, λ is also dependent on the rate constants k_{SiC}, k_{PC}, and k_{PE}, so we consider several limiting values of these constants to understand the presence—or absence—of the reservoir effect under a variety of synthetic conditions.

We assume that k_{SiC} is nonzero and separately consider the limits of equation 4.6 if P evaporation is much faster than P crystallization (i.e. $k_{PE} >> k_{PC}$) or if P crystallization is much faster than P evaporation (i.e. $k_{PC} >> k_{PE}$). In the first limit, equation 4.6 becomes:

$$\lambda \approx \frac{k_{SiC} \varphi_{Si}}{3k_{PE}} R, \text{ for } k_{PE} >> k_{PC} \tag{4.7}$$

In this limit, the transition width goes to zero if the rate constant of P evaporation is much greater than the rate constant for Si crystallization (i.e. $k_{PE} >> k_{SiC}$), causing the reservoir effect to be fully suppressed. In the second limit, equation 4.6 becomes:

$$\lambda \approx \frac{2k_{SiC}\varphi_{Si}}{3k_{PC}}R = \frac{2}{3}\beta\varphi_{Si}R, \text{ for } k_{PC} >> k_{PE} \tag{4.8}$$

where $\beta = \frac{k_{SiC}}{k_{PC}}$ is the segregation coefficient for crystallization of Si and P in the NW (i.e. the ratio of P concentration in the liquid to P concentration in the NW). In this limit, the transition width is linearly dependent on the radius, R, and there is no regime (for VLS growth of Si with Au catalysts) in which the reservoir effect can be suppressed.

To experimentally delineate the different regimes in equations 4.7 and 4.8, we systematically varied NW growth conditions—including NW diameter, growth rate (i.e. SiH_4 partial pressure), and the total CVD reactor pressure—and observed the effect on the NW transition width as measured by wet-chemical etching (see Figure 4.9B and C). Three distinct regions (I, II, and III) were identified. First, at low total pressures (<40 Torr) and relatively low growth rates (<300 nm/min), we observed abrupt transition widths (<10 nm) that were independent of the NW diameter (Figure 4.9C), as shown by the data in the green shaded regions (labeled I). Second, we observed broadened transition widths (∼10–25 nm), as shown by the yellow regions (labeled II), for low pressures with intermediate growth rates and for high pressures with low growth rates. This region also exhibits a diameter dependence (Figure 4.9C). Third, we observed very broad transitions (>30 nm) and a diameter dependence (Figure 4.9C) at high NW growth rates for all reactor pressures, corresponding to the red region (labeled III) in Figure 4.9B. These experimental results were also confirmed by EDS images collected at the lowest pressure, 20 Torr, with the second to lowest and highest NW growth rates (corresponding to regions I and III, respectively). As shown in the fits in Figure 4.9D, the EDS data yielded transition widths of

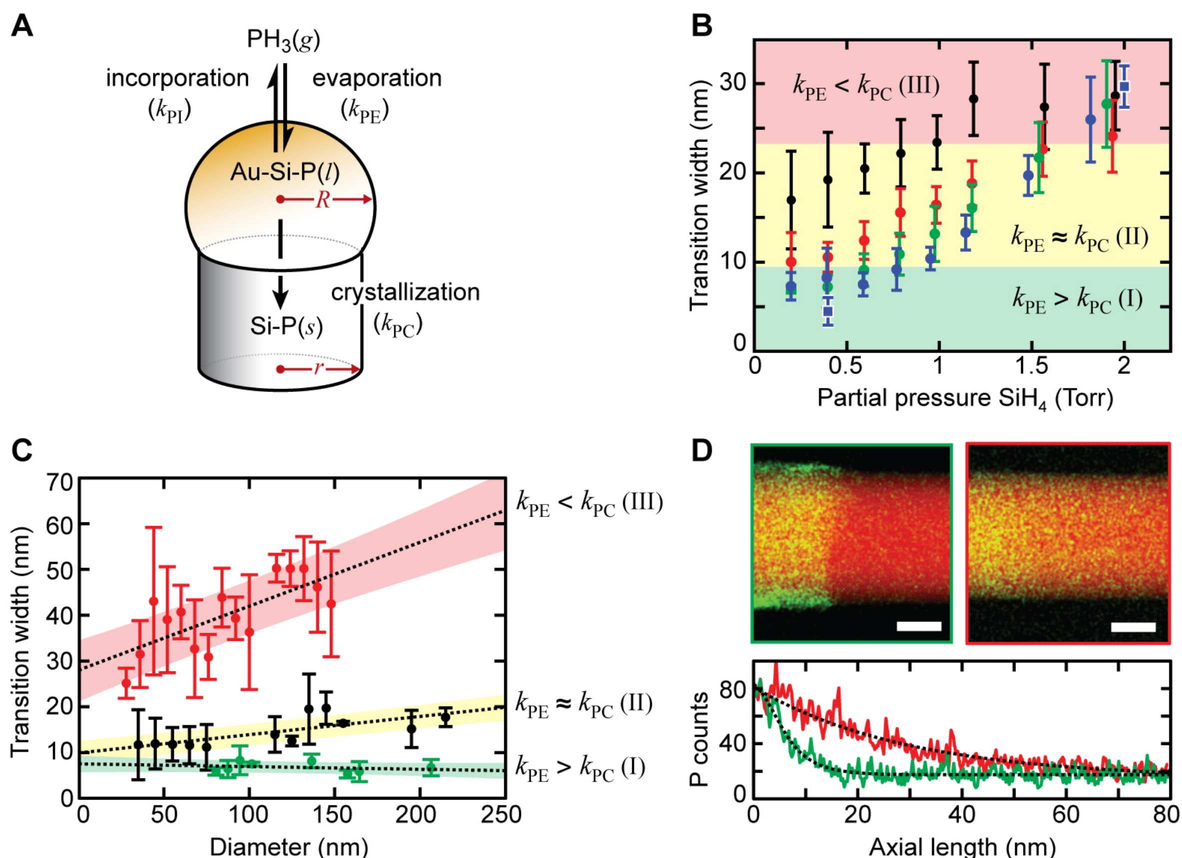

Figure 4.9: Influence of NW growth rate and diameter on the abruptness of n-type/intrinsic dopant heterostructures. (A) Illustration of the key processes for describing the time-dependent P concentration in the catalyst and NW: incorporation, evaporation, and crystallization. (B) Plot of transition width relative to partial pressure of SiH4 for 20 (blue), 40 (green), 60 (red), and 80 (black) Torr total reactor pressure. Blue square data points outlined in white represent transitions widths derived from EDS data in panel D. (C) Plot of transition width vs. diameter for NWs grown at a SiH_4 partial pressure of 0.4 Torr and a total reactor pressure of 20 (green) or 80 (black) Torr, as well as a SiH_4 partial pressure of 2.0 Torr (red) and a total reactor pressure of 20 Torr. Black dashed lines are the best linear fits to each data set, and shaded areas represent one standard deviation error in the fit. (D) EDS images (top) and plot of relative atomic counts vs. axial length (bottom) for NWs grown at a SiH4 partial pressure of 0.4 Torr (left, green) and 2.0 Torr (right, red) at a total reactor pressure of 20 Torr, with growth rates of 100 and 500 nm/min, respectively. The wire grown at a SiH_4 partial pressure of 0.4 Torr shows higher P counts on the edge as a result of higher Au concentration on the surface (see Figure 4.5). The transition widths from these images are plotted in panel B as blue squares with a white outline.

~4 nm and ~30 nm, respectively, under these two conditions.

The three regions observed experimentally can be assigned to different limits of the kinetic analysis (i.e. equations 4.6–4.8). Region I corresponds to synthetic conditions in which evaporation is the dominate term (equation 4.7), causing abrupt dopant transitions. The low pressures and low growth rates favor efficient evaporation of P from the liquid catalyst. This effect is consistent with the abrupt transitions observed from n-type/intrinsic/n-type NWs grown under high vacuum conditions.[169] Region II corresponds to a regime in which the rate constants for evaporation and crystallization are of similar magnitudes (equation 4.6). Finally, region III corresponds to a regime in which P evaporation is slow and P crystallization dominates (equation 4.8), causing substantially broadened transitions. This regime is favored at high NW growth rates (i.e. with high SiH_4 partial pressures) that increase k_{SiC} and φ_{Si} while also disfavoring P evaporation because the higher SiH_4 pressure decreases the number of surface sites available for P associative desorption.

Using the diameter-dependent data from region III, we can calculate φ_{Si}. We first start with equation 4.6 for the transition width for a non-hemispherical catalyst, and then look at the limit where $k_{PC} \gg k_{PE}$ such that

$$\lambda = \frac{(R+\alpha)^2 (2R-\alpha) k_{SiC} \varphi_{Si}}{3r^2 k_{PC}} \tag{4.9}$$

We combine k_{SiC} and k_{PC} into a segregation constant, β, to give:

$$\lambda = \frac{(R+\alpha)^2 (2R-\alpha) \beta \varphi_{Si}}{3r^2} \tag{4.10}$$

We assume a catalyst with a diameter of 110 nm ($R = 55$ nm), a solid NW with a diameter of 100 nm ($r = 50$ nm), and a transition width of 30 nm ($\lambda = 30$ nm). Based on the assumption that

the ratio of Si to P in the liquid catalyst is the same as the vapor phase and that the difference in doping level is due to differences in k_{PC} and k_{SiC}, β is set to 5/3 from the EDS doping level measurements. The volume fraction of Si in Au is then calculated to be: $\varphi_{Si} \approx 26 \pm 5\%$, which is in good agreement with previous reports of the equilibrium volume fraction of Si in Au at 420 °C.[164]

The dependence of the dopant transition width on the NW diameter and on the P incorporation and evaporation rate constants is summarized in Figure 4.10A. Changing the synthetic parameters of VLS NW growth permits a smooth transition between a diameter-dependent transition width consistent with the reservoir effect to a diameter-independent transition width in which the reservoir effect is fully suppressed because of the high rate of P evaporation. Here, we have determined the optimal conditions for abrupt dopant transitions to be low-pressure growth (20 Torr total reactor pressure) with a NW growth rate of ∼200 nm/min, corresponding to a SiH_4 partial pressure of 0.4 Torr. Under these conditions, both the dopant transition width and growth rate[166] are independent of the NW diameter. The only apparent disadvantage of these low-growth-rate conditions is increased Au deposition (see Figure 4.5) on the wire surface,[47] which could potentially be suppressed by addition of HCl to the CVD reactor during VLS growth.[51]

The report of VLS growth conditions that produce abrupt and uniform dopant profiles, as shown here, should assist the development of NW-based technologies. For instance, using the ENGRAVE process,[168] a variety of high-resolution morphological structures can be encoded in NWs with diameters ranging from 50 to 200 nm, as shown in Figure 4.10B. These NWs were grown with the PH_3 flow profile modulated on or off every 6 s, which corresponds to ∼20 nm of NW growth for each section. As demonstrated by the diameter profiles in Figure 4.10C, the ENGRAVE NWs show no loss in spatial resolution as a function of the wire diameter, which is

consistent with full suppression of the reservoir effect.

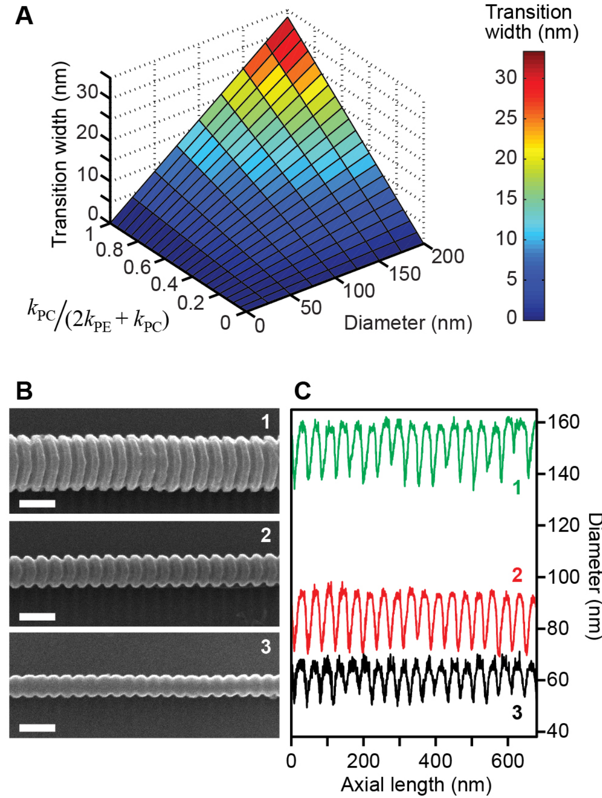

Figure 4.10: Suppressing the reservoir effect for diameter-independent, high-resolution heterostructures. (A) Plot of the n-type/intrinsic transition width as a function of NW diameter and as a function of the ratio between rate constants for P crystallization and P evaporation, where 0 and 1 correspond to the limits $k_{PE} >> k_{PC}$ and $k_{PC} >> k_{PE}$, respectively. (B) SEM images of ENGRAVE NWs created by alternating n-type/intrinsic sections for 6 s each. From top to bottom the NW diameters are (1) ∼150 nm, (2) ∼100 nm, and (3) ∼50 nm; scale bars, 100 nm. (C) Diameter profiles as a function of axial length for NWs 1–3 shown in panel B.

4.4 Conclusions

By examining the width of P dopant transitions at n-type/intrinsic interfaces as a function of Si NW diameter, growth rate (i.e. SiH_4 partial pressure), and total reactor pressure, we have identified a regime in which the reservoir effect can be fully suppressed to produce transition widths of ∼5 nm independent of the NW diameter. Using a detailed kinetic model of NW doping, which includes the processes of P incorporation, evaporation, and crystallization, we have shown that P evaporation plays the primary role in achieving the abrupt interfaces. Our kinetic model

can be applied to a wide range of NW materials grown by the VLS process. The results presented here should provide guidelines to develop the synthetic conditions needed to achieve abrupt compositional and morphological transitions in a variety of NW systems.

CHAPTER 5: ROOM TEMPERATURE ELECTRONIC RATCHETS IN ANISOTROPIC SAWTOOTH SILICON NANOWIRES

5.1 Introduction

Altering the geometry of a material to break structural symmetries can introduce emergent properties, which can be utilized for new technologies and applications. One such technology is a ratchet that takes a time varying force with a mean value of zero and produces directed or rectified movement of a substance such as electrons[174–176] or large biomolecules.[177–179] Ratchets have been used in a variety of applications including separation of molecules,[177–179] molecular motors,[178–180] and solar energy.[174–176] It was previously discovered that materials with crystal structures that are not centrosymmetric can generate electrical current under illumination even though they exhibit homogeneity on macroscopic scales.[176] In this effect, known as the photogalvanic effect, light acts as the external force with a mean value of zero and imposes an unbiased, time-varying electric field on the crystal. Electrical current is generated as a result of rectification of the electric field due to the crystal asymmetry and will propagate in a direction determined by the asymmetry of the crystal structure. This effect has been seen in a wide variety of materials ranging from inorganics (e.g. $LiNbO_3$, $LiTaO_3$, and $BaTiO_3$[176,181,182]) to polymers (e.g. poly(vinylidene flouride)[183,184]).

It is also possible to fabricate ratchets that do not rely on an asymmetry in the crystal structure of the material, but rather the geometry, to provide the asymmetry.[185–190] These ratchets, or geometric diodes, can be produced by either forming the conducting material into an asymmetric geometry such as a sawtooth or by removing material in asymmetric shapes such as triangles or semicircles from the conductive material. As illustrated in Figure 5.1A, it is

possible to understand why an asymmetric structure, like a sawtooth, exhibits rectification by first assuming classical motion of the electrons. When the electrons move along the sawtooth, the reflection off of the surface defined by the shape of the geometric diode funnels the electrons through the constriction. This allows for more current to flow than is defined by cross-sectional area of the constriction. However, when electrons move against the sawtooth, any electrons outside of the cross-sectional area of the constriction are back reflected and do not contribute to current. This effect manifests itself as a difference in resistance based on the polarity of the applied voltage.

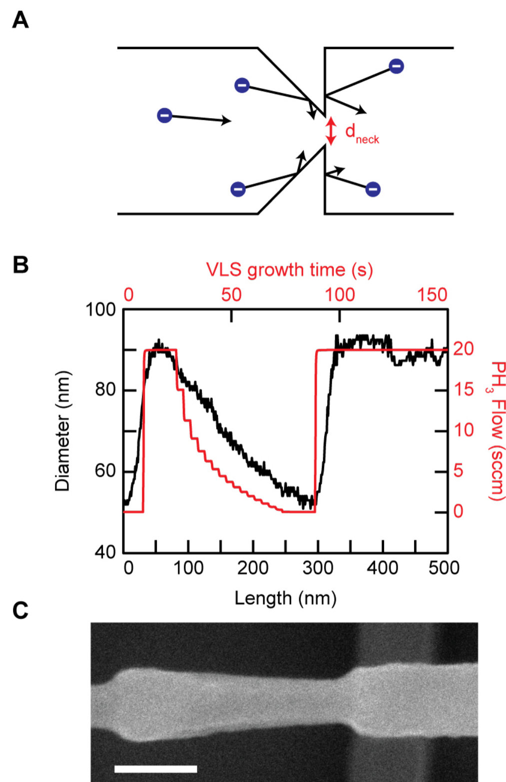

Figure 5.1: Principles of geometric diodes and fabrication of sawtooth Si NWs. (A) Schematic of a sawtooth geometric diode where electrons moving forward are scattered towards the opening and electrons moving backwards are reflected off of the flat interface. The critical parameter is the diameter of the constriction, referred to here as d_{neck}, relative to the mean-free path length. (B) NW diameter (black curve and left-hand axis) as a function of length for a single sawtooth segment shown in panel C, and measured phosphine flow rate (red curve and right-hand axis) in standard cubic centimeters per minute (sccm) as a function of time during CVD growth. (C) SEM image of Si NW after wet-chemical KOH etching; scale bar, 200 nm.

In order to observe the ratcheting effect from a geometric diode, it is necessary for key dimensions of the material to be on the order of the mean–free path length (MFPL) in the material, which generally requires highly conductive materials (e.g. metals and two–dimensional electron gases (2DEGs)) and advanced lithographic techniques (e.g. EBL or FIB milling).[185–190] However, for the first time, we are able to fabricate geometric diodes in Si in a bottom-up process by encoding precise sawtooth structures in VLS-grown Si NWs using the previously described ENGRAVE method (see Chapter 2.2. Realization of a geometric diode within Si NWs will enable more complex electronic designs and open new technologies for future Si NW applications.

5.2 Results

Sawtooth structures have three parameters that govern their shape: the NW diameter, the NW neck diameter, and the period. The NW diameter and the period are both controlled during the NW growth, and the NW neck diameter is controlled through the wet-chemical etch conditions, as described in Chapter 2.2. The most important parameter for a sawtooth structure in determining whether or not the structure is a geometric diode and exhibits rectification is the NW neck diameter.[174] Therefore, we investigated the asymmetry caused by the neck diameter, by varying the etch time.

Si NWs were synthesized in a hot-wall CVD with two 12 μm long n-type regions surrounding the 7 μm long sawtooth region, which consists of 30 repeating sawtooth segments (see Chapter 2.1 for details). Calibration of the NW growth rate and etch rate as described previously allowed precise calculation of the PH_3 flow rate, shown in Figure 5.1B, necessary to produce a single sawtooth segment as shown in Figure 5.1C. The sawtooth NWs were then transferred onto a marker pattern and etched in a wet-chemical KOH solution as described in Chapter 2.2 for times between 90 and 120 seconds. Two contacts were fabricated on either side of the sawtooth region in order to perform four-point probe measurements as detailed in Chapter 2.4.5.

The neck diameter is a critical parameter in whether or not the sawtooth NW will operate as geometric diode, and it needs to be on the order of the MFPL for the material. In Si, the MFPL, l_e can be estimated using the Drude model and the equation:[191]

$$l_e = \frac{m^* v_e \sigma}{ne^2} \tag{5.1}$$

Where m^* is the effective mass, v_e is the thermal velocity, which can be expressed as $\sqrt{3k_B T/m^*}$, σ is the conductance, n is the doping level, and e is the elementary charge. The MFPL for intrinsic Si at room temperature is ∼30 nm and decreases with increased doping level. As the neck diameter shrinks and gets closer the MFPL, the degree of rectification will increase.

To measure the degree of rectification due to the NW neck diameter, we performed four-point probe measurements over the sawtooth regions for a variety of neck diameters. A schematic of the four-point probe measurement is shown in Figure 5.2A, and two sample I–V curves are shown in Figure 5.2B. In Figure 5.2B, the asymmetry in the resistance of the NW (red curve) is evident from the differences in slope based on the applied current, which results in a max voltage difference (red, dashed lines) measured across the sawtooth region of ∼200 mV for an applied current of ±100 nA. The blue curve in Figure 5.2B corresponds to a NWs with larger neck diameters and exhibits no asymmetry as the slopes for each polarity are identical. In order to quantify this asymmetry, we take separate linear fits for positive and negative applied currents to extract the resistance. The diode asymmetry, A, is then defined as:

$$A = \frac{R_{forward}}{R_{reverse}} \tag{5.2}$$

where $R_{forward}$ and $R_{reverse}$ are defined as the resistances for the majority carrier moving along and against the sawtooth, respectively. For $A = 1$, there is no asymmetry as both forward and

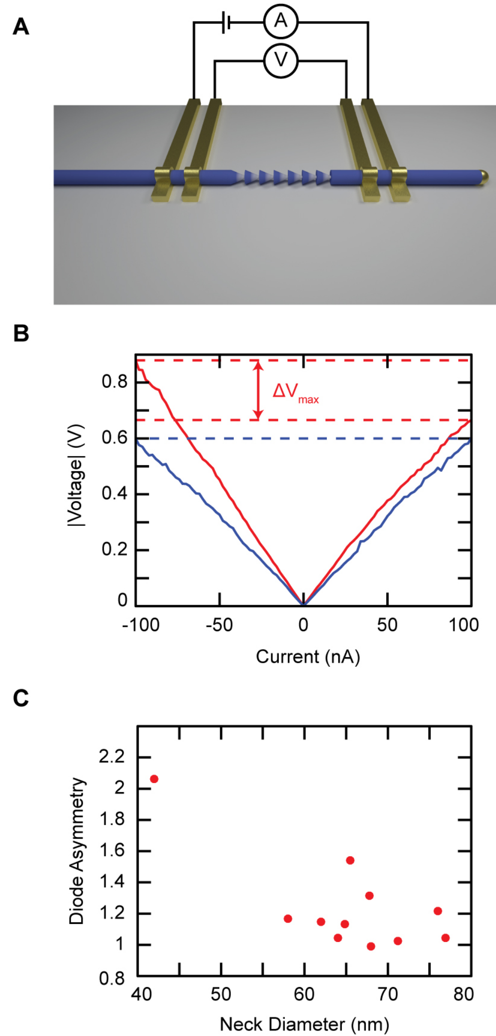

Figure 5.2: Four-point probe measurements of geometric diodes. (A) Schematic illustration of the four-point probe measurements performed on sawtooth NW. A constant current is sourced over the two outermost contacts, and the voltage is measured over the two inner contacts. (B) Characteristic I–V curves from four-point probe measurements for sawtooth NWs. The diode asymmetry and neck diameter of the two measured NWs are 1.02 and 76 nm (blue) and 1.31 and 67 nm (red). The dashed lines correspond to the voltage maximums for positive and negative currents. (C) Plot of diode asymmetry versus NW neck diameter.

reverse directions display the same resistance. For $A > 1$, the majority carrier flows more easily along the sawtooth structure than against it leading to a lower resistance in the reverse than in the forward direction. The measured diode asymmetries for a variety of NW neck diameters show a negative correlation with one another and reach diode asymmetry values over 2 for neck diameters less than 45 nm, as seen in Figure 5.2C. As the NW neck diameter shrinks, it samples more of the free path length distribution, which is dependent on the distributions of both the velocities and scattering times, leading to a higher asymmetry. There is also a high degree of scatter in the data that can be attributed variations in surface quality, which could be improved through thermal oxidation treatments.[102]

These experiments are only a start, and more experiments are need to understand the most important parameters that drive the geometric diode behavior. One parameter that was not studied in this work and that should be the focus of future experiments is the temperature of the NW. By cooling the sample to liquid nitrogen temperatures (∼77 K), the diode asymmetry should increase as the free path length distribution is shifted to longer path lengths and the MFPL increases accordingly. The NW diameter should also increase the diode asymmetry, not by modifying the MFPL, but by increasing the current that can be funneled through the junction under forward bias without affecting the current under reverse bias.[174] In order to fully understanding these effects, Monte Carlo simulations would provide a physical picture as to the interplay between the temperature, neck diameter, NW diameter, and period of the sawtooth segments, and their effects on the diode asymmetry.[174,192]

One of the main applications for geometric diodes is a rectenna, which is an antenna that converts radiation to alternating current combined with an ultrahigh-speed diode to rectify the current. They are used as rectennas because they have a capacitance of a few attofarads and can be fabricated from materials with resistances of a few kΩ, which means their RC time constant

is on the order of femtoseconds.[174] Therefore, four-point probe measurements with an alternating current source should be performed to determine the extent and the frequency response of the ratcheting effect of sawtooth segments. The frequency response of the NW is dependent on the RC time constant, and in Si NWs, the resistance will be the dominate term. Therefore, it will be necessary to keep the resistance of the NW as low as possible. This could be achieve by limiting the number of sawtooth segments and placing the contacts across the region as close to one another as possible, by modifying the PH_3 flow and etch times such that a higher doping level is maintained through the sawtooth structure, and/or by increasing the NW diameter.

5.3 Conclusion

Here, we have successfully demonstrated a geometric diode based on Si NWs by etching asymmetric sawtooth patterns into the Si NWs using the previously described ENGRAVE method. To the best of our knowledge, this is the first demonstration of a bottom-up, purely Si geometric diode, and should serve as the basis for developing advanced electrical applications through the ENGRAVE method.

CHAPTER 6: DESIGN PRINCIPLES FOR PHOTOVOLTAIC DEVICES BASED ON SI NANOWIRES WITH AXIAL OR RADIAL P–N JUNTIONS[1]

6.1 Introduction

Semiconductor NW p-type/n-type (p–n) junctions represent a fundamental building block for the construction of advanced electronic and photonic devices based on single NWs. These junctions have been realized in a range of NW systems including Si,[81,102,133,193–198] InP,[199] GaN,[200] GaAs,[201,202] and CdS.[203,204] As illustrated in Figure 6.1A, two widely explored geometries are the axial junction, in which the p–n transition is encoded along the length of the wire, and the radial junction, in which the p–n transition is encoded from the center to outer surface, creating a core-shell geometry. Axial p–n junctions have permitted wires to be used as sensors,[159] photodiodes,[85] and photovoltaics[133,199] while radial junctions have primarily been used for photovoltaic devices.[81,193,200,201] Because of the ease of doping, integration, earth abundance, and relatively low cost, Si NWs have received special attention as an important new technology, especially for solar energy applications.[120,156,205] Compared with well-developed planar crystalline Si, wire based Si structures could enable low-cost solar cells by permitting high power-conversion efficiencies with relatively low-quality Si.[86]

Here, we use finite-element simulations to delineate the characteristics and theoretical performance of Si NWs with either axial or radial p–n junctions and with diameters limited to a few hundred nanometers. We compare our simulation results to experimental measurements on NWs

[1]This chapter previously appeared as an article in Nano Letters. The original citation is as follows: Christesen, J. D.; Zhang, X.; Pinion, C. W.; Celano, T. A.; Flynn, C. J.; Cahoon, J. F. Design Principles for Photovoltaic Devices Based on Si Nanowires with Axial or Radial p–n Junctions. Nano Lett. **2012**, *12*, 6024–6029.

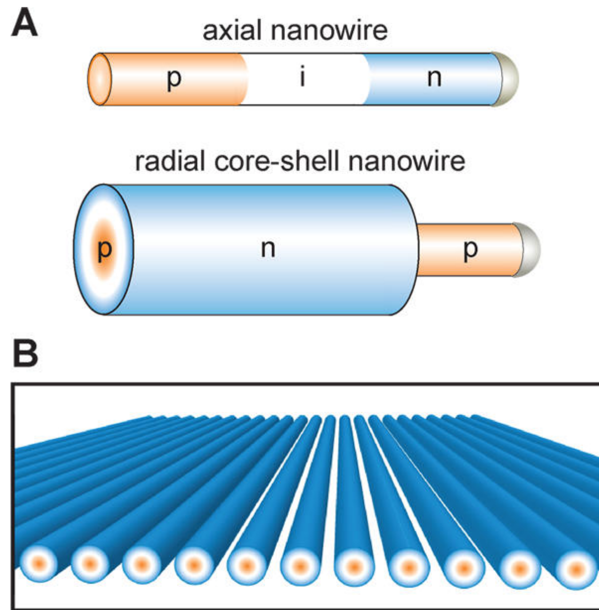

Figure 6.1: Overview of NW geometries used for photovoltaics. (A) Illustration of two distinct classes of NW p–n or p–i–n junctions that can be synthesized using VLS growth from a metal nanoparticle, including axial junctions (top) and radial junctions (bottom). (B) Schematic of NWs organized in a periodic horizontal array to form an ultrathin photovoltaic device.

synthesized by a VLS mechanism.[206] In these VLS-grown wires, axial p–n or p-type/intrinsic/n-type (p–i–n) junctions are encoded by in situ doping of the wire during VLS growth.[133,197,199] For core/shell NWs, the radial junctions are encoded by additional in-situ doping of the shell, which is formed by a VS-growth mechanism.[81,193] Our modeling evaluates realistic NW device geometries and accounts for the effects of degenerately doped Si and charge carrier recombination by SRH, Auger, and surface recombination mechanisms.[107]

The wire-based solar cells considered here are composed of NWs oriented horizontally such that they are uniformly illuminated along their total length. To create a large-area solar cell, these wires can be arranged in a periodic array, as illustrated in Figure 6.1B. This topology is well-suited to take advantage of the optical resonances and photonic crystal effects that result from the subwavelength dimensions of the NWs and periodic arrangement, causing substantially enhanced light absorption.[81,152,207] An alternative implementation of Si wire based solar cells uses

arrays of vertically oriented wires that are several micrometers in diameter.[86,102,194,195] These vertical wire arrays have been produced both by VLS growth[102,195] and by top-down etching of planar wafers or films.[194,198] The performance has been analyzed theoretically,[86,208] highlighting the benefit of collecting charge carriers over short, radial directions that are perpendicular to light propagation. The horizontal wires considered here operate in a different regime, in which the diameters are confined to subwavelength dimensions (200–300 nm) to take advantage of the optical effects in this geometry. Here, we address the device physics of these NWs to fully understand their potential as high-quality diodes and as wire based thin-film photovoltaic devices.

6.2 Methods

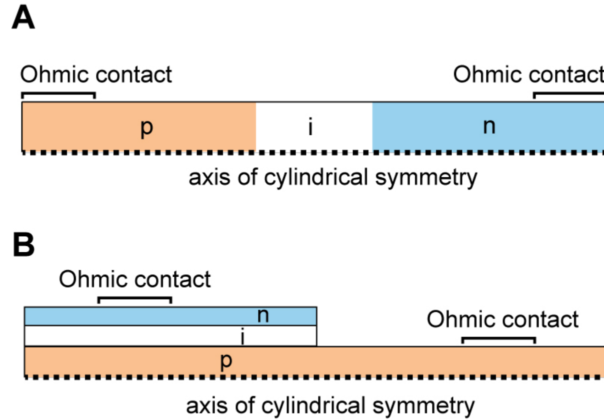

Figure 6.2: Details of simulation geometries used for finite-element modeling (A) Illustration of the axial p–i–n NW structure, which has been modeled as a two-dimensional geometry with cylindrical symmetry. The total axial length of the simulation was fixed at 4.04 μm, the intrinsic length at 40 nm, and radius at 120 nm. 500 nm Ohmic metal contacts (black lines) were positioned at the left- and right-hand surfaces of the NW. (B) Illustration of the radial p–i–n NW core-shell structure, which has been modeled as a two-dimensional geometry with cylindrical symmetry. The axial length of the simulation was fixed at 4 μm and evenly divided between the core and core-shell regions. The core radius and core-shell radius were fixed at 50 and 120 nm, respectively. Ohmic metal contacts (black lines) were positioned at the left- and right-hand surfaces of the NW.

The small size and geometry of NW p–n junctions is well suited to finite element modeling that can accommodate arbitrary geometries and include a wide range of device physics parameters. The NWs were represented as a two-dimensional simulation domain with cylindrical symmetry

(see Figure 6.2), which reduces computational cost but realistically represents the NWs as three-dimensional geometries. For each simulation point, we solved for the drift and diffusion of charge carriers in the presence of SRH, Auger, and surface recombination until converged stationary points were found. The simulations account for band gap renormalization in degenerately doped Si with the associated effects on built-in voltage and intrinsic carrier concentration.[107] Uniform optical generation of charge carriers was included to produce a short–circuit current density (J_{SC}) of 7 mA/cm^2 under 1 sun illumination (except where noted otherwise), which is consistent with experimental measurement and with theoretical predictions of optical absorption in these structures.[152,207] A detail of the equations used is provided in Chapter 2.5.

6.3 Results

To define key characteristics determined by the geometry of the nanoscale p–n junctions, we examined the charge density and built-in electric fields for axial and radial NWs over a range of doping levels, as illustrated in Figure 6.3. To facilitate a direct comparison of the two geometries, both simulated structures possess a total diameter of 240 nm and include a $\sim$ 40 nm intrinsic region between the n- and p-type regions. As expected, the doping level has a substantial effect on the space charge density and the electric field strength within the wires. For axial NWs (Figure 6.3A) with doping levels of 10^{18} cm^{-3} or greater, neither the n-type nor p-type regions reach full depletion. For instance, at 10^{20} cm^{-3}, the depletion region is at most 5% depleted, reaching a charge density of 5×10^{18} q/cm^3. For all doping levels, the electric field strength (Figure 6.3B) is on the order of 10^7 V/m, a value that is sufficiently high for carriers to reach saturation drift velocity in Si.[107]

For radial devices, we examined NWs with doping levels ranging from 5×10^{17} to 10^{20} cm^{-3}, as shown in Figure 6.3C,D. A detailed examination reveals several unique features. First, as observed in axial devices, the n- and p-type regions do not reach full depletion for doping levels

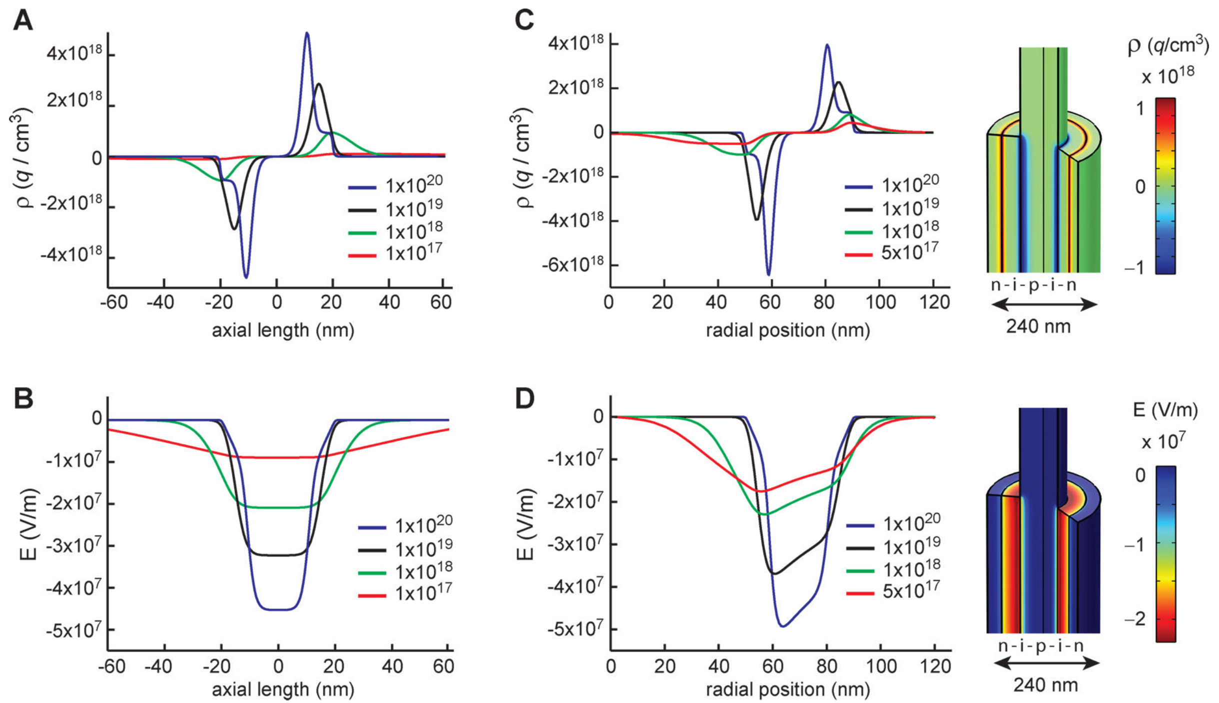

Figure 6.3: Charge density and electric field distributions for axial and radial NWs. (A) Charge density profiles in axial NWs for donor and acceptor doping levels of $10^{17} - 10^{20}$ cm^{-3}. (B) Electric field profiles caused by the charge density distributions shown in panel A. (C) Charge density profiles (left) in radial NWs for donor and acceptor doping levels $5 \times 10^{17} - 10^{20}$ cm^{-3}. Three-dimensional illustration (right) of the charge density distribution for 10^{18} cm^{-3}. (D) Profiles (left) and three-dimensional illustration (right) of the electric field generated by the charge density distributions shown in panel C.

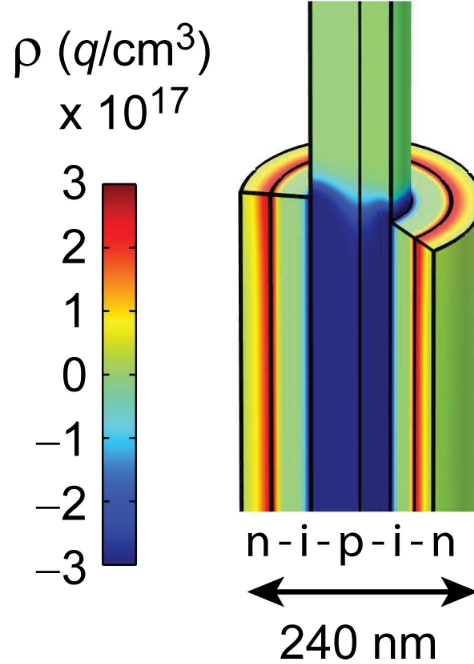

Figure 6.4: Depiction of the space-charge region in radial NWs at low doping levels. Schematic of the charge density distribution in a core-shell p–i–n NW with p-type and n-type doping levels of 3×10^{17} cm^{-3}. The p-type core appears dark blue because it has been fully depleted of holes, reaching a charge density of -3×10^{17} q/cm^3.

greater than 10^{18} cm^{-3}. Second, the positive and negative charge distributions are asymmetric. For example, with a doping level of 10^{19} cm^{-3}, the negative charge density reaches a maximum value of $\sim 4 \times 10^{18}$ q/cm^3 while the positive side reaches only half the value, $\sim 2 \times 10^{18}$ q/cm^3. Third, the doping level of 5×10^{17} cm^{-3} produces a depletion region that extends to the center of the NW. Fourth, the electric field distributions (Figure 6.3D) are asymmetric, reflecting the asymmetry in the charge density distributions. The maximum electric field strengths increase with higher doping levels and, similar to axial devices, are on the order of 10^7 V/m.

The asymmetries present in the charge density and electric field distributions of the radial

NWs result from the cylindrical symmetry of this junction. The magnitudes of both quantities are lower at larger radius because of the increasing volume per unit radius in the outer regions of the wire. This effect is especially pronounced at lower doping levels; below a doping level of 5×10^{17} cm^{-3}, the outer n-type shell retains a defined depletion region whereas the inner p-type core is fully depleted (see Figure 6.4). This effect prevents establishment of the full built-in potential drop across the junction, lowering the device performance and placing a lower limit on doping level that can be used in this structure.

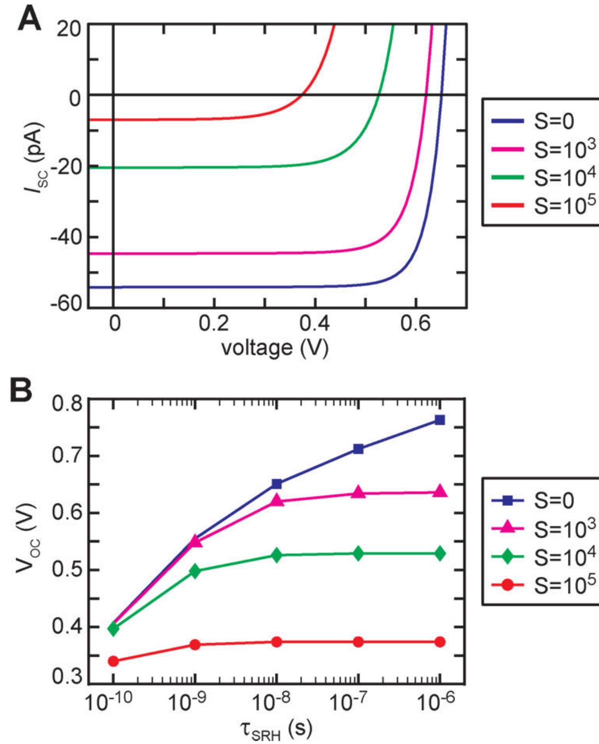

Figure 6.5: Analysis of axial p–i–n junction photovoltaic device characteristics. (A) Simulated I–V curves for axial NWs with a doping level of 10^{18} cm^{-3} and $\tau_{SRH} = 10^{-8}$ s. (B) V_{OC} versus minority carrier lifetimes of $\tau_{SRH} = 10^{-10} - 10^{-6}$ s for a doping level of 10^{18} cm^{-3}. Simulations in panels A and B included SRVs of S = 10^5 (red), 10^4 (green), 10^3 (magenta), and 0 cm/s (blue).

To probe the photovoltaic characteristics of axial NW p–n junctions, we analyzed the performance of devices over a range of parameters, as presented in Figure 6.5. We have performed simulations with SRH minority carrier lifetimes (τ_{SRH}) ranging from $\tau_{\mathrm{SRH}} = 10^{-10}$ to

10^{-6} s, which reflect varying mid-band-gap trap-state densities. Simulated current–voltage (I–V) curves for $\tau_{\text{SRH}} = 10^{-8}$ s are displayed in Figure 6.5A, and photovoltaic metrics for a range of parameters are provided in Table 6.1. These I–V curves also include SRVs of S = $0 - 10^5$ cm/s to account for a broad range of surface trap-state densities. Both short–circuit current (I_{SC}) and V_{OC} show a dramatic dependence on the SRV. From S = 10^5 to S = 0 cm/s, V_{OC} increases by 75% while I_{SC} increases by nearly 1 order of magnitude. The increase in I_{SC} results from a substantial increase in the internal quantum efficiency (IQE) of the wire, as discussed later. The increase in V_{OC} results from both the increase in I_{SC} and a reduction in charge carrier recombination within the depletion region, which is modulated by the SRV because of the direct exposure of the depletion region to the outer surface.

τ_{SRH} (s)	S (cm/s)	V_{OC} (V)	I_{SC} (pA)	FF	power (pW)	n	I_0 (fA)
10^{-10}	0	0.407	8.549	65.1	2.3	1.86	1.702
10^{-10}	10^5	0.340	5.672	61.5	1.2	1.86	4.515
10^{-9}	0	0.555	24.765	73.6	10.1	1.85	0.170
10^{-9}	10^5	0.369	6.823	63.3	1.6	1.86	3.009
10^{-8}	0	0.651	54.147	80.6	28.4	1.85	0.002
10^{-8}	10^5	0.374	6.992	63.3	1.7	1.86	2.855
10^{-7}	0	0.712	65.972	84.1	39.5	1.85	0.002
10^{-7}	10^5	0.374	7.010	63.3	1.7	1.86	2.840
10^{-6}	0	0.763	67.560	85.6	44.1	1.83	0.0002
10^{-6}	10^5	0.374	7.012	63.3	1.7	1.86	2.838

Table 6.1: Simulated photovoltaic metrics for axial NW p–i–n junctions with donor/acceptor doping levels of 10^{18} cm^{-3} , total NW diameter of 240 nm, and intrinsic segment length of 40 nm

We systematically examine the effect of τ_{SRH} and SRV on V_{OC} in axial nanowires with a doping level 10^{18} cm^{-3} in Figure 6.5B. For a SRV of S = 10^5 cm/s, V_{OC} is limited to an upper value of 0.37 V for all values of τ_{SRH}. For smaller values of SRV, increasing τ_{SRH} progressively increases V_{OC}, reaching a value of ~ 0.76 V for S = 0 cm/s and $\tau_{\text{SRH}} = 10^{-6}$ s. Surprisingly, this value exceeds the maximum V_{OC}, 0.71 V, reported for monocrystalline Si.[209] To understand

this result, we can consider the expression for V_{OC} given by the Shockley diode equation:

$$V_{OC} \approx \left(\frac{nkT}{q}\right) ln\left(\frac{I_{SC}}{I_0}\right) \tag{6.1}$$

where n is the ideality factor, k the Boltzmann constant, T temperature, q electron charge, and I_0 the dark saturation current. As evident from this expression, V_{OC} is maximized by maximizing I_{SC} while simultaneously minimizing I_0. The axial geometry is uniquely suited to satisfy this condition because the small p–n junction area (defined by the NW cross-sectional area) minimizes I_0 while the long n- and p-type segments absorb light and maximize I_{SC}.

A similar analysis of the photovoltaic performance of radial NWs is presented in Figure 6.6. Current density–voltage (J–V) curves for radial NWs with a doping level of 10^{18} cm^{-3} and τ_{SRH} ranging from 10^{-10} to 10^{-6} s are displayed in Figure 6.6A, and photovoltaic metrics for a range of parameters are listed in Tables 6.2 and 6.3. V_{OC} is dependent on both the τ_{SRH} and SRV, and the dependence of V_{OC} on these two parameters is plotted in Figure 6.6B. As expected, V_{OC} progressively increases with longer τ_{SRH} but, surprisingly, is relatively insensitive to the SRV for $\tau_{SRH} = 10^{-10} - 10^{-8}$ s. For longer τ_{SRH} ($10^{-7} - 10^{-6}$ s), however, V_{OC} shows a stronger dependence on SRV and is limited to a value of 0.54 V for S = 10^5 cm/s. With complete elimination of surface recombination (S = 0 cm/s), V_{OC} reaches a maximum value of 0.73 V at $\tau_{SRH} = 10^{-6}$ s.

We analyzed the power-conversion efficiency (η) of wires with doping levels of $10^{18} - 10^{20}$ cm^{-3}. From the results over a range of τ_{SRH} and S (see Figure 6.7), a doping level of 10^{18} cm^{-3} maximizes efficiency. Higher doping levels exhibit reduced efficiency primarily as a result of increased Auger recombination. Doping levels below 10^{18} cm^{-3}, on the other hand, fully deplete the p-type core as discussed earlier (see Figure 6.4).

The efficiency of radial NWs was determined for progressively increasing values of J_{SC}

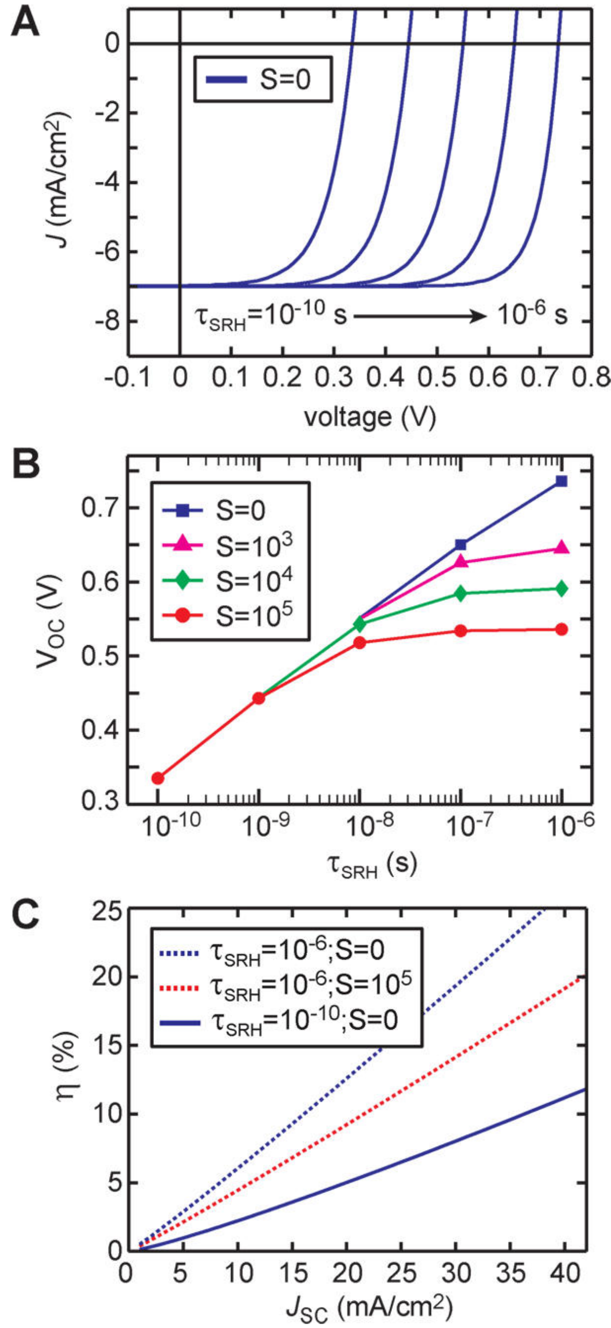

Figure 6.6: Analysis of radial p–i–n junction photovoltaic device characteristics. (A) J–V characteristics for radial wires with a doping level of 10^{18} cm^{-3} and $\tau_{SRH} = 10^{-10} - 10^{-6}$ s, assuming a J_{SC} of 7 mA/cm^2 and SRV of S = 0 cm/s. (B) V_{OC} as a function of τ_{SRH} for a doping level of 10^{18} cm^{-3} and SRVs of S = 10^5 (red), 10^4 (green), 10^3 (magenta) and 0 cm/s (blue). (C) Power-conversion efficiencies (η) as a function of J_{SC} for wires with a doping level of 10^{18} cm^{-3} and with $\tau_{SRH} = 10^{-10}$ s (solid line) and 10^{-6} s (dashed lines) for SRVs of S = 0 (blue) and S = 10^5 cm/s (red).

τ_{SRH} (s)	S (cm/s)	V_{OC} (V)	J_{SC} (mA/cm^2)	FF	η (%)	n	I_0 (fA)
10^{-10}	0	0.335	6.97	61.9	1.45	1.85	30.4
10^{-10}	10^5	0.334	6.89	61.7	2.12	1.85	30.3
10^{-9}	0	0.444	7.00	68.1	2.12	1.85	3.03
10^{-9}	10^5	0.443	6.91	68.0	2.08	1.85	3.03
10^{-8}	0	0.551	7.00	72.7	2.81	1.82	0.275
10^{-8}	10^5	0.518	6.92	75.3	2.70	1.79	0.267
10^{-7}	0	0.650	7.00	75.3	3.48	1.82	0.027
10^{-7}	10^5	0.534	6.92	80.2	2.96	1.26	0.002
10^{-6}	0	0.736	7.00	80.2	4.13	1.85	0.003
10^{-6}	10^5	0.536	6.92	80.9	3.00	1.06	0.0001

Table 6.2: Simulated photovoltaic metrics for radial NW p–i–n junctions with donor/acceptor doping levels of 10^{18} cm $^{-3}$, total NW diameter of 240 nm, and intrinsic segment length of 40 nm

τ_{SRH} (s)	S (cm/s)	V_{OC} (V)	J_{SC} (mA/cm^2)	FF	η (%)	n	I_0 (fA)
10^{-10}	0	0.271	6.81	57.0	1.05	1.85	117
10^{-10}	10^5	0.269	6.52	56.9	1.00	1.85	117
10^{-9}	0	0.382	6.96	64.8	1.72	1.85	11.7
10^{-9}	10^5	0.379	6.64	64.8	1.63	1.85	11.7
10^{-8}	0	0.489	6.98	70.3	2.40	1.85	1.17
10^{-8}	10^5	0.484	6.65	70.6	2.27	1.84	1.14
10^{-7}	0	0.579	6.98	75.7	3.06	1.84	0.114
10^{-7}	10^5	0.542	6.65	78.0	2.81	1.77	0.096
10^{-6}	0	0.610	6.98	81.4	3.47	1.77	0.010
10^{-6}	10^5	0.552	6.65	81.2	2.98	1.48	0.004

Table 6.3: Simulated photovoltaic metrics for radial NW p–i–n junctions with donor/acceptor doping levels of 10^{20} cm^{-3} , total NW diameter of 240 nm, and intrinsic segment length of 40 nm

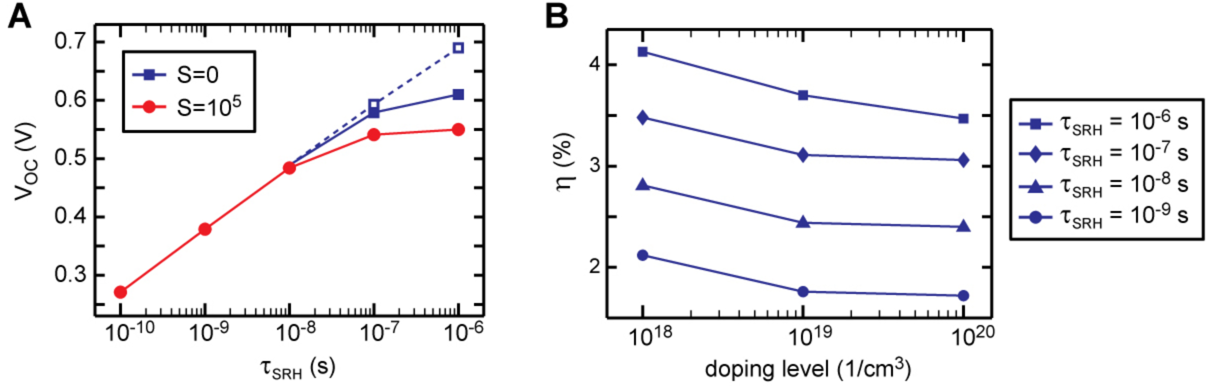

Figure 6.7: Photovoltaic performance of radial NWs at high doping levels (A) V_{OC} as a function of the minority carrier lifetimes, SRH, for a doping level of 10^{20}cm^{-3} and SRVs of S = 10^5 (red) and 0 (blue) cm/s. Dashed line and open blue squares represent simulated data points in the absence of Auger recombination (B) Power-conversion efficiencies (η) as a function of doping level for SRH = $10^{-9} - 10^{-6}$ s and SRV of S = 0 (blue). Simulations assume a J_{SC} of 7 mA/cm^2. Diameter of the NW is 240 nm and intrinsic segment length is 40 nm.

from 1 to 40 mA/cm^2, as illustrated in Figure 6.6C for $\tau_{\mathrm{SRH}} = 10^{-10}$ and 10^{-6} s. Although experimental devices exhibited J_{SC} of only 7–10 mA/cm^2, further efforts to exploit light-trapping, photonic crystal, or plasmonic structures could be used to substantially enhance J_{SC} in these systems.[207,210] The simulation results demonstrate that the electrical properties of Si NWs are sufficient to support ultrathin solar cells with efficiencies in the range of 15–25%. Notably, a value of $\tau_{\mathrm{SRH}} \sim 10^{-6}$ s can produce an efficiency >15% at a J_{SC} of 35 mA/cm^2 with poor surface passivation (S = 10^5 cm/s). Efficiency could be increased to >20% through elimination of surface recombination (S = 0 cm/s).

We synthesized axial and radial p–i–n NWs as described in Chapeter 2.1.[81,133] Measured I–V and J–V curves for axial and radial NWs under simulated 1 sun AM1.5G illumination are shown in Figure 6.8A and Figure 6.8B, respectively, along with the best fit simulations. The simulated and experimental I–V curves without illumination (not shown) are well fit to the Shockley diode equation (eq 6.1), which can be used to extract n and I_0. Note that the axial NW simulation geometry was adjusted to a diameter of 160 nm and intrinsic length of 2 μm to

accurately reflect scanning electron microscopy images of the measured device. All experimental photovoltaic metrics are compared to the simulations of best fit in Table 6.4. For radial devices, a value of $\tau_{\mathrm{SRH}} = 3$ ns and SRV of $S \leq 10^5$ cm/s reproduced the device parameters (V_{OC}, fill factor (FF), η, n, and I_0) from the core-shell p–i–n NWs. Similarly for axial devices, a value of $\tau_{\mathrm{SRH}} \geq 5$ ns and a SRV of $S = 7 \times 10^3$ cm/s reproduced the measured device parameters. The good agreement of all metrics with experiment validates the use of finite-element simulations to analyze the performance of p–n junction NWs and to examine their prospect as a new class of ultrathin solar cell. Furthermore, the simulations demonstrate that the photovoltaic performance of axial devices is predominantly limited by SRV, whereas the performance of radial devices is limited by the bulk SRH recombination lifetime (τ_{SRH}). Because performance is limited by one parameter, we can at most place limits on the value of the other parameter—a lower limit $\tau_{\mathrm{SRH}} = 5$ ns for axial and upper limit of $S = 10^5$ cm/s for radial devices.

	τ_{SRH} (s)	S (cm/s)	V_{OC} (V)	J_{SC}^a (mA/cm^2)	FF	η (%)	n	I_0 (fA)
axial NW								
experiment			0.234	4.8	48	0.36	1.91	38
simulation	$\geq 5^b$	7×10^3	0.232	4.8	55	0.41	1.65	63
radial NW								
experiment			0.441	9.8	69	2.99	1.59	3.73
simulation	3	$\leq 10^{5,c}$	0.449	9.8	69	3.03	1.84	3.75

Table 6.4: Comparison of experimental and simulated photovoltaic metrics for axial and radial NWs. [a]Estimated using the intrinsic segment projected area for axial NWs and core-shell projected area for radial NWs. [b]Higher values produced similar photovoltaic metrics. [c]Lower values produced similar photovoltaic metrics.

As shown in Figure 6.11, we have examined the spatially dependent IQE of axial and radial NW junctions to understand the benefits and limitations of these geometries for efficient charge carrier collection. In axial NWs, the p-type, intrinsic, and n-type regions are each exposed to the outer surface. Within the depletion region, the IQE is >95% for SRVs of $S = 10^5$ cm/s and only

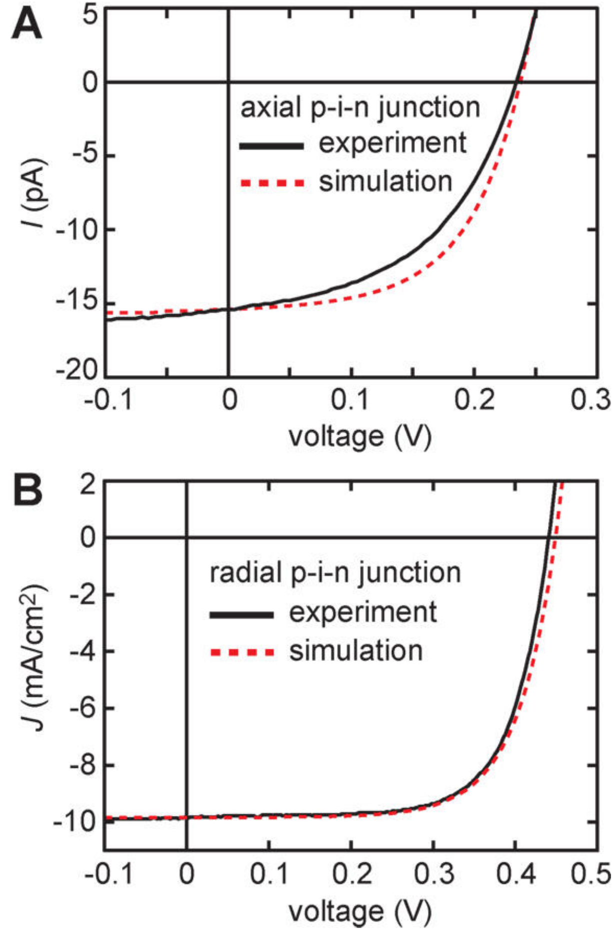

Figure 6.8: Comparison of simulated and experimental I–V or J–V curves for single-NW photovoltaics under 1 sun illumination. (A) Experimental I–V curve (black) for an axial VLS-grown p–i–n NW with a diameter of $\sim$ 160 nm and synthetically encoded intrinsic length of $\sim$ 2000 nm. Simulated I–V curve (dashed red) was calculated using this experimental geometry, $\tau_{SRH} = 100$ ns, SRV of S $= 7 \times 10^3$ cm/s, and the experimentally measured J_{SC} of 4.8 mA/cm^2. (B) Experimental J–V curve (black) for a radial p–i–n NW with a diameter of 260 nm composed of a VLS-grown p-type core of $\sim$ 100 nm diameter and intrinsic and n-type shell thicknesses of $\sim$ 45 and $\sim$ 35 nm, respectively. Simulated J–V curve (dashed red) was calculated using $\tau_{SRH} = 3$ ns, SRV of S $= 10^5$ cm/s, and assuming the experimentally measured J_{SC} of 9.8 mA/cm^2.

drops to $\sim 80\%$ with a SRV of S = 10^6 cm/s. Because the minority carrier diffusion length is much larger than the NW diameter, the IQE shows negligible radial dependence and instead decays exponentially along the length of the wire away from the depletion region. This decay is well fit to a monoexponential function (see Figure 6.9), which yields the effective minority carrier diffusion length (L_{eff}). It has been established that the L_{eff} is typically limited by the SRV rather than by the bulk minority carrier lifetime. Consequently, L_{eff} can be related to the diffusion constant D, minority carrier lifetime τ, S, and the NW diameter, d, as[197,211]

$$L_{\text{eff}} = \sqrt{D\left(\frac{1}{\tau} + \frac{4S}{d}\right)^{-1}} \tag{6.2}$$

For example, with τ = 10 ns, S = 10^5 cm/s, and D = 1.45 cm^2/s, the electron L_{eff} from eq 6.2 is estimated to be 93 nm, which is in agreement with the fit to our simulation that yields a value of 96 nm (see Figure 6.9). Lower values of S produce substantially larger values of L_{eff} and, consequently, higher values of I_{SC} (see Figure 6.5A and Figure 6.10) as a result of high IQE values over a larger portion of the NW.

Unlike axial p–i–n devices, radial junctions possess buried p-type and intrinsic regions that are isolated from the wire surface. IQE as a function of radial position for a device with $\tau_{SRH} = 10^{-8}$ s is plotted in Figure 6.11B. Remarkably, the IQE is unity throughout the p-type and intrinsic regions and deviates from unity only in the outer 30 nm of the n-type region. For SRV of S = 10^5 cm/s, the IQE decays linearly from $\sim 100\%$ at the edge of the depletion region to 84% at the outer surface, producing a high overall IQE of 95% for the entire core-shell region. Decreasing the surface recombination to S = 10^4 cm/s improves the overall IQE to 99%, and IQE at the surface is 98%. These results demonstrate the dramatic advantage of core-shell structures to produce high IQE values even with relatively high SRVs and low τ_{SRH}. In Figure 6.11C, we present a spatial map of IQE throughout the core and core-shell regions of a radial junction

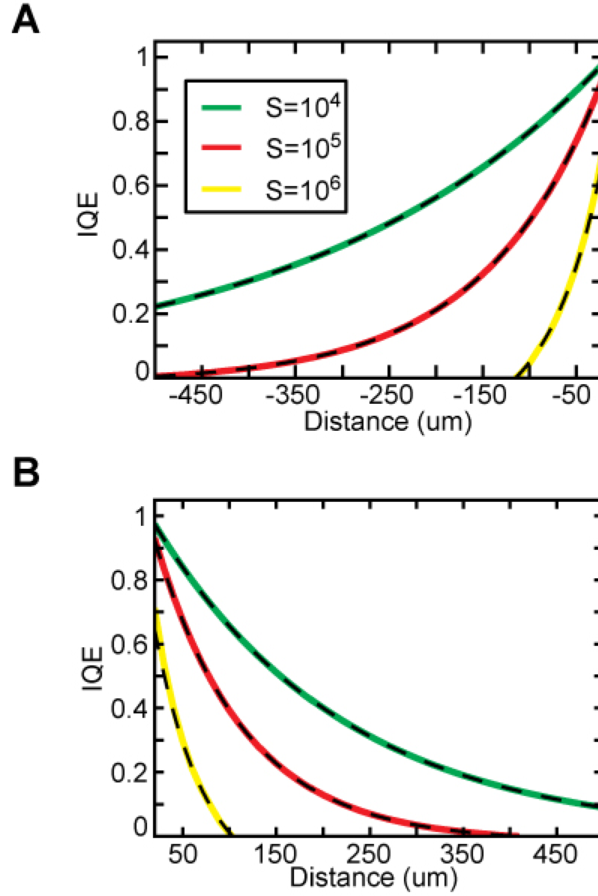

Figure 6.9: Effective minority carrier diffusion length in axial NWs (A) Simulated data (solid colored lines) and mono-exponential fits (dashed black lines) for the IQE in the p-type quasi-neutral region of axial NWs (see Figure 6.11A) with a doping level of 10^{20}cm^{-3} and minority carrier lifetime of SRH = 10^{-8} s. The fits give effective minority carrier diffusion lengths, Leff, of 324 nm, 126 nm, and 58 nm for S = 10^4 (green), 10^5 (red), and 10^6 (yellow) cm/s, respectively (B) Simulated data (solid colored lines) and mono-exponential fits (dashed black lines) for the IQE in the n-type quasi-neutral region of axial NWs (see Figure 6.11A) with a doping level of 10^{20}cm^{-3} and minority carrier lifetime of SRH = 10^{-8} s. The fits give L_{eff} of 203 nm, 96 nm, and 53 nm for S= 10^4 (green), 10^5 (red), and 10^6 (yellow) cm/s, respectively.

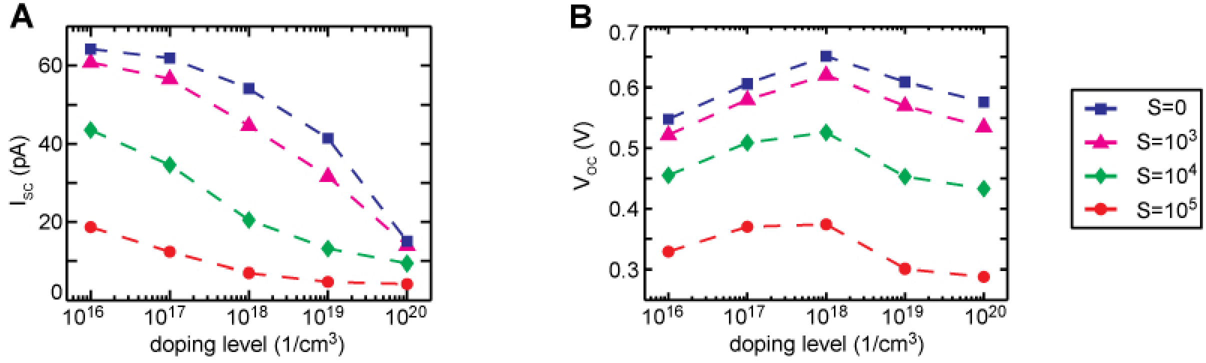

Figure 6.10: Photovoltaic performance of axial NWs at high doping levels (A) Short-circuit current (I_{SC}) and (B) open-circuit voltage (V_{OC}) versus doping level for axial NWs with SRH = 10 ns and SRVs of S = 0 (blue), 10^3 (magenta), 10^4 (green), and 10^5 (red) cm/s. Simulations assume a J_{SC} of 7 mA/cm^2. Diameter of the NW is 240 nm and intrinsic segment length is 40 nm.

device with S = 10^5 cm/s. For the core-shell region, IQE is >80% except in the vicinity of the Ohmic contacts. For the core region, the IQE quickly approaches zero as result of surface recombination.

In conclusion, finite element simulations were used to evaluate the performance of axial and radial NW p–n junctions and to reproduce experimental measurements on these two NW structures. The simulations demonstrate that Si NW photovoltaic devices are capable of producing V_{OC} values of $\sim$ 0.7 V and could serve as the basis for thin-film solar cells with power-conversion efficiencies in the range of 15–25%. Radial wires show distinct advantages over axial wires, exhibiting high IQE values nearly independent of surface recombination. The experimental measurements suggest that axial structures are limited by surface recombination whereas radial structures are limited by a bulk minority carrier lifetime of $\sim$ 3 ns. For radial NWs, an improvement of the lifetime by $\sim$ 2 orders of magnitude would be sufficient to maximize the photovoltaic performance. These results provide motivation for the continued development of 200–300 nm diameter Si NW photovoltaic structures and demonstrate the utility of finite element simulations to quantitatively evaluate and design NW p–n junctions.

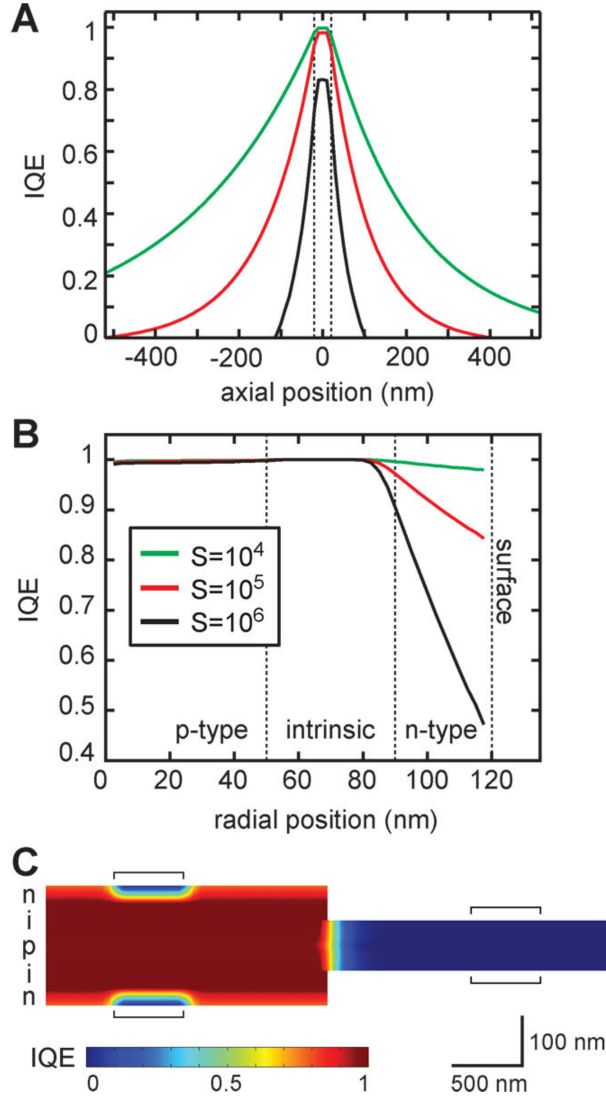

Figure 6.11: IQE of axial and radial NWs. (A) Radially integrated IQE as a function of axial position along an axial p–i–n NW with doping level of 10^{20} cm^{-3}, minority carrier lifetime of $\tau_{SRH} = 10^{-8}$ s, and SRVs of S = 10^4 (green), 10^5 (red), and 10^6 cm/s (black). (B) Axially integrated IQE as a function of radial position for a radial p–i–n NW with doping level of 10^{20} cm^{-3}, minority carrier lifetime of $\tau_{SRH} = 10^{-8}$ s, and SRVs of S = 10^4 (green), 10^5 (red), and 10^6 cm/s (black). (C) Spatial map of IQE for a radial p–i–n NW as shown in panel B with SRV S = 10^5 cm/s. Black bars indicate the positions of the Ohmic contacts.

CHAPTER 7: CONCLUSIONS

We investigated using rational synthetic control composition of NWs in combination with a wet-chemical etch to encode morphology in Si NWs as an alternative route to current "top-down" fabrication techniques for advanced optical and electronic applications. This bottom-up method, called ENGRAVE, enables morphological features as small as 10 nm to be patterned over NWs more than 50 μm in length. We investigate and determine the dependence of the wet-chemical etch rate with respect to doping level in order to synthesis a wide range of shapes including nanorods, sinusoids, bowties, tapers, nanogaps, and gratings.

We then utilized the ENGRAVE method to study the abruptness of these heterojunctions in VLS-grown NWs. The VLS mechanism is a a process in which a liquid droplet—supplied with precursors in the vapor phase—catalyzes the growth of a solid, crystalline NW. By modulating the vapor phase precursors, the NW composition is altered, creating axial heterostructures, which are important for a wide range of technologies. The abruptness of the heterojunction is mediated by the liquid catalyst, which can act as a reservoir of material and impose a lower limit on the junction width. We demonstrate that this "reservoir effect" is not a fundamental limitation and can be suppressed by using slow NW growth rates ($<$200 nm/min) and low total reactor pressures ($<$40 Torr) to enhance evaporation of the reservoir material and suppress incorporation of the reservoir material into the NW. Using these conditions, we were able to grow NWs with diameter independent and radially uniform dopant profiles with abrupt, sub 10 nm axial transitions.

We utilized this control over doping level and morphology in the NW to create several

devices with applications in optics, memory, and electronics. For applications in optics, we used nanogap-encoded NWs as templates for Noble metals, yielding plasmonic structures with tunable resonances for surface-enhanced Raman imaging. For applications in memory, core/shell Si/SiO_2 nanorods were integrated into electronic devices that exhibit resistive switching, enabling nonvolatile memory storage. For applications in electronics, we created a geometric diode based on an asymmetric sawtooth geometry for use as an electronic ratchet, and further work to study the ratcheting effect in this device is ongoing. These are just initial examples of the variety of devices that can be synthesized using the ENGRAVE methods, and we envision this method will become a generic route to encode new functionality in semiconductor NWs.

Finally, we investigate the effect of device geometry and compositional control over the photovoltaic performance of axial and radial Si NW p–n junctions through finite-element simulations. We compare simulated current–voltage data to experimental measurements, permitting detailed analysis of NW performance, limitations, and prospect as a technology for solar energy conversion. Although high surface-to-volume ratios are cited as detrimental to NW performance, radial p–n junctions are surprisingly insensitive to surface recombination, although axial devices, in which the depletion region is exposed to the surface, are far more sensitive to SRV.The simulations show that with further development the electrical characteristics of 200–300 nm Si NWs are sufficient to support power-conversion efficiencies of 15–25%, and the analysis presented here can be generalized to other semiconductor homo- and heterojunctions, which can serve as a guide for the design of advanced nanoscale structures.

APPENDIX: CODE FOR IMAGE ANALYSIS

```
function varargout = nanoWireDiameter(varargin)
    % Begin initialization code - DO NOT EDIT
    gui_Singleton = 1;
    gui_State = struct('gui_Name',       mfilename, ...
                       'gui_Singleton',  gui_Singleton, ...
                       'gui_OpeningFcn', @nanoWireDiameter_OpeningFcn
                          , ...
                       'gui_OutputFcn',  @nanoWireDiameter_OutputFcn,
                           ...
                       'gui_LayoutFcn',  [] , ...
                       'gui_Callback',   []);
    if nargin && ischar(varargin{1})
        gui_State.gui_Callback = str2func(varargin{1});
    end

    if nargout
        [varargout{1:nargout}] = gui_mainfcn(gui_State, varargin{:});
    else
        gui_mainfcn(gui_State, varargin{:});
    end
    % End initialization code - DO NOT EDIT
end %end vargout = nanoWireDiameter

% --- Executes just before nanoWireDiameter is made visible.
function nanoWireDiameter_OpeningFcn(hObject, eventdata, handles,
   varargin)

    %This the directory where the open file function will start
    handles.filePath = 'D:\Users\Joe\SEM_Images\';

    %Initialization of variables that will be used throughout the
       program.
    handles.original_pic = [0,0];
    handles.original_rot_pic = [0,0];
    handles.nmPerPixel = 1;
    handles.bins = [0,0];
    set(handles.scaleBar, 'String', handles.nmPerPixel);
    handles.current_pic = [0,0];
    handles.rot_pic = [0,0];
    handles.diameters = [0,0];
    handles.horz_pic = [0,0];
    handles.bin1_value = .5;
    handles.bin2_value = .4;
    handles.bin3_value = .3;
    handles.originalx = 0;
```

```
handles.originaly = 0;
handles.data = 0;
handles.transitions = 0;
handles.fileName = 0;
handles.bin_pic = 0;
handles.nm = 0;
handles.threshold_value = .4;
handles.range_value = 8;
handles.gaussSpace = [0,0];


%Create the data variables that get updated
%Generate the initial plot in axes1
handles.current_datax = 0;
handles.current_datay = 0;

%initialize the filter value variable
%controls the size of the window for 1D Median Filter
handles.current_filter_value = 3;

%initialize the number of times run
handles.num_times_run = 1;

%initialize minmax function
%minmax is a vector of 1's and 0's used to represent the x-value
    of
%transitions. 1 = transition.
handles.minmax = 0;

%initialize minmaxIdx
%used in conjuction with find() to extract the x values of
    detected transitions
handles.minmaxIdx = 1;

%initialize tranRad
%number of points to ignore on either side of transition point
    when
%calculating average diameter/stdev
handles.tranRad = 10;

%program output
handles.realOutput = [1 1 1];

% Choose default command line output for nanoWireDiameter
handles.output = hObject;

% Update handles structure
guidata(hObject, handles);
```

```
end % end nanoWireDiameter_OpeningFcn

% --- Outputs from this function are returned to the command line.
function varargout = nanoWireDiameter_OutputFcn(hObject, eventdata,
  handles)
    % Get default command line output from handles structure
    varargout{1} = handles.output;
end % end nanoWireDiameter_OutputFcn

%%%%%%%%%%%%%%%%%%%%%%%%%%%%%%%%%%%%%%%%%%%%%%%%%%%%%%%%%%%%%%%%%%%%%%%%%%%
%Initializtion functions that set the scale of the image and rotate
%the wire to the correct orientation
%%%%%%%%%%%%%%%%%%%%%%%%%%%%%%%%%%%%%%%%%%%%%%%%%%%%%%%%%%%%%%%%%%%%%%%%%%%

% --- Executes on button press in setScale.
function setScale_Callback(hObject, eventdata, handles)
    %This will find the scale bar for images taken on the FEI Helios
       FIB

    %Gets a row and column along the far right side and bottom of the
        image
    subWidth = length(handles.original_pic(1,:))-1;
    subHeight = length(handles.original_pic(:,1))-1;

    %Finds the white boxes from the SEM image
    whiteHeight = find(handles.original_pic(subHeight,:)>=.9);
    whiteWidth = find(handles.original_pic(:,subWidth)>=.9);

    %Takes the midPoint of the white box that contains the scale bar
    midPoint = ceil((whiteWidth(end-1)-whiteWidth(end-2))/2+
       whiteWidth(end-2));
    consec = false;
    endColumn = subWidth;
    startColumn = whiteHeight(end-1);

    %Scans the columns from right to left starting at the midPoint
       until
    %it his consecuative white points.
    while ~consec
       if  endColumn < numel(handles.original_pic(midPoint, :)) &&
          endColumn>=1
           if handles.original_pic(midPoint, endColumn) >= 0.9 && ...
                   handles.original_pic(midPoint, endColumn-1) >=
                      0.9, consec = true;
           end %end if
       end %end if
       if endColumn > numel(handles.original_pic(midPoint,:))
```

```
            exception = MException('Outside_of_Picture_limits',...
                'Could_not_find_consecuative_points_to_locate_the_
                   scale_bar');
            throw(exception);
        end %end if
        if ~consec
            endColumn = endColumn - 1;
        end %end if
    end %end while

    consec = false;

    %Scans the columns from left to right starting at the midPoint
        until
    %it his consecuative white points.
    while ~consec
        if  startColumn < numel(handles.original_pic(midPoint, :)) &&
            startColumn>=1
            if handles.original_pic(midPoint, startColumn) >= 0.9 &&
                ...
                    handles.original_pic(midPoint, startColumn+1) >=
                        0.9, consec = true;
            end%end if
        end %end if
        if startColumn > numel(handles.original_pic(midPoint,:))
            exception = MException('Outside_of_Picture_limits',...
                'Could_not_find_consecuative_points_to_locate_the_
                   scale_bar');
            throw(exception);
        end %end if
        if ~consec
            startColumn = startColumn + 1;
        end %end if
    end %end while loop

    %Get the number of pixels in the scale bar and outputs the actual
         scale
    temp = str2double(handles.nm);
    handles.nmPerPixel = temp/(endColumn-startColumn);
    set(handles.scaleBar, 'String', handles.nmPerPixel);

    % Choose default command line output for slider_gui
    handles.output = hObject;

    % Update handles structure
    guidata(hObject, handles);
end %end nanoWireDiameter_OpeningFcn
```

```
% --- Executes on button press in setRotate.
function setRotate_Callback(hObject, eventdata, handles)

    %Gets a line drawn by the user. Left click places a point and
       right
    %click ends the line.
    [x,y] = getline(handles.largePic);
    newPic = handles.current_pic;

    %Gets 4 points around the starting point and makes them a value
       of
    %21 or 22 (for end points). Uses 4 points incase during rotation
    %point is lost
    newPic(floor(y(1)), floor(x(1))) = 21;
    newPic(ceil(y(1)), floor(x(1))) = 21;
    newPic(floor(y(1)), ceil(x(1))) = 21;
    newPic(ceil(y(1)), ceil(x(1))) = 21;
    newPic(floor(y(2)), floor(x(2))) = 22;
    newPic(ceil(y(2)), floor(x(2))) = 22;
    newPic(floor(y(2)), ceil(x(2))) = 22;
    newPic(ceil(y(2)), ceil(x(2))) = 22;

    %Calculates the length of the line segment
    lineSegLength = sqrt((x(1)-x(2))^2+(y(1)-y(2))^2);

    %Vector of the line
    vec_x = x(2)-x(1);
    vec_y = y(2)-y(1);

    %Angle between the line and verticle
    theta = radtodeg(acos(vec_y/lineSegLength));

    %Rotates the picture the correct amount. Determines whether to
       use a
    %negative angle or positive
    if vec_x > 0
       rotPic = imrotate(newPic, -theta, 'loose');
    else
       rotPic = imrotate(newPic, theta, 'loose');
    end %end if-else

    %Finds the starting and ending points
    [new_y, new_x] = find(rotPic == 21);
    [new_y2, new_x2] = find(rotPic == 22);

    %Picks the line going from top to bottom and takes the subPic
       area
    x1 = new_x(1)-500;
```

```
    x2 = new_x2(1)+500;
    if x1<=0
        x1 = 1;
    elseif x1>=length(rotPic(1,:))
        x1 = length(rotPic(1,:));
    end %end if-elseif
    if x2<=0
        x2 = 1;
    elseif x2>=length(rotPic(1,:))
        x2 = length(rotPic(1,:));
    end %end if-elseif

    if new_y(1)<new_y2(1)
      subPic = rotPic(new_y(1):new_y2(1),x1:x2);
    else
      subPic = rotPic(new_y2(1):new_y(1),x1:x2);
    end %end if-else

    handles.current_pic = subPic;
    handles.original_rot_pic = handles.current_pic;
    handles.rot_pic = subPic;
    cla(handles.largePic);
    imshow(handles.current_pic, 'Parent', handles.largePic);

    % Choose default command line output for slider_gui
    handles.output = hObject;

    % Update handles structure
    guidata(hObject, handles);
end %end setRotate_Callback

%%%%%%%%%%%%%%%%%%%%%%%%%%%%%%%%%%%%%%%%%%%%%%%%%%%%%%%%%%%%%%%%%%%%%%%%%%%
%These functions are used for editing the image and coloring in
%black and white areas where the background intensity is too high
%or the wire intesity is too low.
%%%%%%%%%%%%%%%%%%%%%%%%%%%%%%%%%%%%%%%%%%%%%%%%%%%%%%%%%%%%%%%%%%%%%%%%%%%

% --- Executes on button press in colorBlack.
function colorBlack_Callback(hObject, eventdata, handles)
    %Draws a black box over the image to remove problem areas

    [finalrect] = getrect(handles.largePic);
    finalY = finalrect(1,2)+finalrect(1,4);
    finalX = finalrect(1,1)+finalrect(1,3);

    if finalrect(1,1) < 1
        finalrect(1,1) = 1;
    end
```

```
    if finalrect(1,2) < 1
        finalrect(1,2) = 1;
    end
    if finalX > numel(handles.rot_pic(1,:))
        finalX = numel(handles.rot_pic(1,:));
    end
    if finalY > numel(handles.rot_pic(:,1))
        finalY = numel(handles.rot_pic(:,1));
    end


    handles.rot_pic(floor(finalrect(1,2)):floor(finalY), floor(
       finalrect(1,1)):floor(finalX))=0;


    handles.current_pic = showThePic(handles);

    % Choose default command line output for slider_gui
    handles.output = hObject;

    % Update handles structure
    guidata(hObject, handles);
end %end colorBlack_Callback

% --- Executes on button press in colorWhite.
function colorWhite_Callback(hObject, eventdata, handles)
    %Draws a white box over the image to improve the contrast of the
       wire

    [finalrect] = getrect(handles.largePic);
    finalY = finalrect(1,2)+finalrect(1,4);
    finalX = finalrect(1,1)+finalrect(1,3);

    if finalrect(1,1) < 1
        finalrect(1,1) = 1;
    end
    if finalrect(1,2) < 1
        finalrect(1,2) = 1;
    end
    if finalX > numel(handles.rot_pic(1,:))
        finalX = numel(handles.rot_pic(1,:));
    end
    if finalY > numel(handles.rot_pic(:,1))
        finalY = numel(handles.rot_pic(:,1));
    end

    handles.rot_pic(floor(finalrect(1,2)):floor(finalY), floor(
       finalrect(1,1)):floor(finalX))=1;
```

```
    handles.current_pic = showThePic(handles);

    % Choose default command line output for slider_gui
    handles.output = hObject;

    % Update handles structure
    guidata(hObject, handles);
end %end colorWhite_Callback


%%%%%%%%%%%%%%%%%%%%%%%%%%%%%%%%%%%%%%%%%%%%%%%%%%%%%%%%%%%%%%%%%%%%%%%%%%%%%
%These functions are used for binning the picture including
%Creating all of the bin sliders (bin1, bin2, bin3_Callback),
%Setting up the initial bin (bins_Callback), and
%Allowing editing of the sliders (bin1, bin2, bin3_edit_Callback)
%%%%%%%%%%%%%%%%%%%%%%%%%%%%%%%%%%%%%%%%%%%%%%%%%%%%%%%%%%%%%%%%%%%%%%%%%%%%%

% --- Executes on button press in bins.
function bins_Callback(hObject, eventdata, handles)
    %Takes the average of the mid line which should include the wire
    midColumn = floor(length(handles.current_pic(1,:))/2);
    averageIntensity = mean(handles.current_pic(:, midColumn));

    handles.bin3_value = averageIntensity*0.5;  %50% of average
       intensity
    handles.bin2_value = averageIntensity*0.75; %75% of average
       intensity
    handles.bin1_value = averageIntensity;      %average intensity

    set(handles.bin1, 'Value', handles.bin1_value);
    set(handles.bin2, 'Value', handles.bin2_value);
    set(handles.bin3, 'Value', handles.bin3_value);
    set(handles.bin1, 'Min', handles.bin2_value);
    set(handles.bin2, 'Max', handles.bin1_value);
    set(handles.bin2, 'Min', handles.bin3_value);
    set(handles.bin3, 'Max', handles.bin3_value);
    set(handles.bin1_edit, 'String', handles.bin1_value);
    set(handles.bin2_edit, 'String', handles.bin2_value);
    set(handles.bin3_edit, 'String', handles.bin3_value);

    handles.bins = showThePic(handles);
    handles.current_pic = handles.bins;


    % Choose default command line output for slider_gui
    handles.output = hObject;
```

```
    % Update handles structure
    guidata(hObject, handles);
end %end bins_Callback

% --- Executes on slider movement.
function bin1_Callback(hObject, eventdata, handles)
    % Hints: get(hObject,'Value') returns position of slider
    %        get(hObject,'Min') and get(hObject,'Max') to determine
        range of slider

    handles.bin1_value = get(hObject, 'Value');
    set(handles.bin1_edit, 'String', handles.bin1_value);
    set(handles.bin2, 'Max', handles.bin1_value);


    handles.bins=showThePic(handles);
    handles.current_pic = handles.bins;

    % Choose default command line output for slider_gui
    handles.output = hObject;

    % Update handles structure
    guidata(hObject, handles);
end %end bin1_Callback

% --- Executes during object creation, after setting all properties.
function bin1_CreateFcn(hObject, eventdata, handles)
    % Hint: slider controls usually have a light gray background.
    if isequal(get(hObject,'BackgroundColor'), get(0,'
        defaultUicontrolBackgroundColor'))
         set(hObject,'BackgroundColor',[.9 .9 .9]);
    end
end %end bin1_CreateFcn

function bin1_edit_Callback(hObject, eventdata, handles)
end %end bin1_edit_Callback

% --- Executes during object creation, after setting all properties.
function bin1_edit_CreateFcn(hObject, eventdata, handles)
    % Hint: edit controls usually have a white background on Windows.
    %       See ISPC and COMPUTER.
    if ispc && isequal(get(hObject,'BackgroundColor'), get(0,'
        defaultUicontrolBackgroundColor'))
         set(hObject,'BackgroundColor','white');
    end
end %end bin1_edit_CreateFcn

% --- Executes on slider movement.
```

```
function bin2_Callback(hObject, eventdata, handles)
    % Hints: get(hObject,'Value') returns position of slider
    %        get(hObject,'Min') and get(hObject,'Max') to determine
       range of slider

    handles.bin2_value = get(hObject, 'Value');
    set(handles.bin2_edit, 'String', handles.bin2_value);
    set(handles.bin3, 'Max', handles.bin2_value);
    set(handles.bin1, 'Min', handles.bin2_value);


    handles.bins=showThePic(handles);
    handles.current_pic = handles.bins;

    % Choose default command line output for slider_gui
    handles.output = hObject;

    % Update handles structure
    guidata(hObject, handles);
end %end bin2_Callback

% --- Executes during object creation, after setting all properties.
function bin2_CreateFcn(hObject, eventdata, handles)
    % Hint: slider controls usually have a light gray background.
    if isequal(get(hObject,'BackgroundColor'), get(0,'
       defaultUicontrolBackgroundColor'))
        set(hObject,'BackgroundColor',[.9 .9 .9]);
    end
end %end bin2_CreateFcn

function bin2_edit_Callback(hObject, eventdata, handles)
    % Hints: get(hObject,'String') returns contents of bin2_edit as
       text
    %        str2double(get(hObject,'String')) returns contents of
       bin2_edit as a double
end %end bin2_edit_Callback

% --- Executes during object creation, after setting all properties.
function bin2_edit_CreateFcn(hObject, eventdata, handles)
    % Hint: edit controls usually have a white background on Windows.
    %       See ISPC and COMPUTER.
    if ispc && isequal(get(hObject,'BackgroundColor'), get(0,'
       defaultUicontrolBackgroundColor'))
        set(hObject,'BackgroundColor','white');
    end
end %end bin2_edit_CreateFcn

% --- Executes on slider movement.
```

```
function bin3_Callback(hObject, eventdata, handles)
    % Hints: get(hObject,'Value') returns position of slider
    %        get(hObject,'Min') and get(hObject,'Max') to determine
       range of slider

    handles.bin3_value = get(hObject, 'Value');
    set(handles.bin3_edit, 'String', handles.bin3_value);
    set(handles.bin2, 'Min', handles.bin3_value);


    handles.bins=showThePic(handles);
    handles.current_pic = handles.bins;

    % Choose default command line output for slider_gui
    handles.output = hObject;

    % Update handles structure
    guidata(hObject, handles);
end %end bin3_Callback

% --- Executes during object creation, after setting all properties.
function bin3_CreateFcn(hObject, eventdata, handles)
    % Hint: slider controls usually have a light gray background.
    if isequal(get(hObject,'BackgroundColor'), get(0,'
       defaultUicontrolBackgroundColor'))
        set(hObject,'BackgroundColor',[.9 .9 .9]);
    end
end %end bin3_CreateFcn

function bin3_edit_Callback(hObject, eventdata, handles)
    % Hints: get(hObject,'String') returns contents of bin3_edit as
       text
    %        str2double(get(hObject,'String')) returns contents of
       bin3_edit as a double
end %end bin3_edit_Callback

% --- Executes during object creation, after setting all properties.
function bin3_edit_CreateFcn(hObject, eventdata, handles)
    % Hint: edit controls usually have a white background on Windows.
    %       See ISPC and COMPUTER.
    if ispc && isequal(get(hObject,'BackgroundColor'), get(0,'
       defaultUicontrolBackgroundColor'))
        set(hObject,'BackgroundColor','white');
    end
end %end bin3_edit_CreateFcn

%%%%%%%%%%%%%%%%%%%%%%%%%%%%%%%%%%%%%%%%%%%%%%%%%%%%%%%%%%%%%%%%%%%%%%%%%%
%These functions deal with creating the transition lines
```

```
%%%%%%%%%%%%%%%%%%%%%%%%%%%%%%%%%%%%%%%%%%%%%%%%%%%%%%%%%%%%%%%%%%%%%%%%%%%%%

% --- Executes on button press in editLines.
function editLines_Callback(hObject, eventdata, handles)
    output = linePlot(handles.diameters,handles.horz_pic(:,:,1),
        handles.nmPerPixel,...
         find(handles.minmax==1));
    for i = 1:numel(output(:,2))
        temp(i,1) = find(handles.diameters(:,1)>output(i,2),1,'first'
            );
    end %end for
    handles.minmax(:,1) = 0;
    handles.minmax(temp) = 1;
    handles.minmaxIdx = find(handles.minmax);

    plotLines(hObject, eventdata, handles);
    handles=guidata(handles.output);%ensure handles get updated
    tableData(hObject, eventdata, handles);
    handles=guidata(handles.output);%ensure handles get updated

    % Choose default command line output for slider_gui
    handles.output = hObject;

    % Update handles structure
    guidata(hObject, handles);
end %end editLines_Callback

% --- Executes on button press in dispTrans.
function dispTrans_Callback(hObject, eventdata, handles)
    calcTrans(hObject, eventdata, handles);
    handles=guidata(handles.output);%ensure handles get updated

    plotLines(hObject, eventdata, handles);
    handles=guidata(handles.output);%ensure handles get updated

    %n by 2 array with the xlocations of transitions in column 1 and
        1's in
    %the second
    handles.minmaxIdx = find(handles.minmax);

    vect(:,1) = handles.minmaxIdx;
    vect(:,2) = 1;

    tempminmax = handles.minmax; %create a temporary copy of minmax
        to edit
    entriesToKeep = find(vect(:,2)); %find the x-values to keep
    assignin('base','entriesToKeep',entriesToKeep);
    assignin('base','tempminmax',tempminmax);
```

```
    tempminmax = zeros(length(tempminmax),1);

    for m = 1:size(entriesToKeep)
        tempminmax(vect(entriesToKeep(m)),1)=1;
    end %end for

    handles.minmaxIdx = vect(entriesToKeep,1);%replace the old x-
       values with the new ones
    handles.minmax = tempminmax;

    tableData(hObject, eventdata, handles);
    handles=guidata(handles.output);%ensure handles get updated

    % Choose default command line output for slider_gui
    handles.output = hObject;

    % Update handles structure
    guidata(hObject, handles);
end %end dispTrans_Callback

function calcTrans(hObject, eventdata, handles)
    %the list of scales at which to perform the analysis
    scales = [1, 2, 4, 8];

    %a list of numbers between 0 and 1 indicating how obvious a step
       has to be
    %at each scale in order to be considered a transition.
    %Do Not Edit unless you know what the values mean
    thresholds = [.1, .2, .3, .4];

    % Create the derivative scale space--minima and maxima of the
       derivative
    % correspond to transitions
    data = CreateGaussScaleSpace(handles.current_datay, 1, scales);

    %Find the position of local minima and maxima of the most coarse
       scale
    handles=guidata(handles.output);%ensure handles get updated
    handles.minmax = FindLocalExtrema(data(:, end), thresholds(end),
       scales(end));
    guidata(handles.output,handles);%ensure handles get updated

    %Place x-coordinate of transitions into a list
    handles=guidata(handles.output);%ensure handles get updated
    handles.minmaxIdx = find(handles.minmax);
    guidata(handles.output,handles);%ensure handles get updated

    % Refine min/max positions through scale space
```

```
    for i = size(scales)-1:-1:1
        handles=guidata(handles.output);%ensure handles get updated
           throughout the for loop
        handles.minmax = FindLocalExtrema(data(:,i), thresholds(i),
           scales(i), handles.minmaxIdx);
        handles.minmaxIdx = find(handles.minmax);
    end %end for

    % Choose default command line output for slider_gui
    handles.output = hObject;

    % Update handles structure
    guidata(hObject, handles);
end %end calcTrans

function plotLines(hObject, eventdata, handles)
    cla(handles.widthPlot); %clear the diameter plot axes
    plot(handles.originalx,handles.current_datay, 'Parent', handles.
       widthPlot);%plot the current data
    hold(handles.widthPlot,'on')

    %plot calculated transition points using minmax
    %(0 everywhere except at transitions, where it is 1
    set(handles.widthPlot, 'XLim', [0 handles.diameters(end,1)]);

    set(handles.widthPlot, 'YLim', [min(handles.diameters(:,2))-5 max
       (handles.diameters(:,2))+5]);
    y = get(handles.widthPlot, 'YLim');
    ydif = y(2) - y(1);
    plot(handles.originalx,(1.0 * handles.minmax * ydif) + y(1)...
        , 'r', 'Parent', handles.widthPlot);
    hold(handles.widthPlot,'off')
    handles.transitions = [handles.originalx, (1.0 * handles.minmax *
        ydif) + y(1)];

    cla(handles.horizontalPic);
    imshow(handles.horz_pic,'Parent',handles.horizontalPic);
    hold(handles.horizontalPic,'on')
    plot(1.0 * handles.minmax * 401, 'r', 'Parent', handles.
       horizontalPic);
    hold(handles.horizontalPic,'off')

    % Choose default command line output for slider_gui
    handles.output = hObject;

    % Update handles structure
    guidata(hObject, handles);
end %end plotLines
```

```
function tableData(hObject, eventdata, handles)
    stats = RegionStats(handles.current_datay, handles.minmaxIdx,
       handles.tranRad);
    quick = handles.minmaxIdx; %give quick access to updated x values
        for transitions

    %lengthdata is a column vector with the length(in mm) of each
       region
    %between transisitons
    lengthdata(1)=handles.originalx(quick(1)); %length from beginning
        of wire image area to first transition

    %calcualte the length between each of the transitions
    for m=2:length(quick)
        lengthdata(m)= handles.originalx(quick(m))-handles.originalx(
           quick(m-1));
    end %end for

    %length from last transition to end of wire image area
    lengthdata(end+1)= handles.originalx(length(handles.originalx))-
       handles.originalx(quick(end));

    output(:,2) = lengthdata;%place the lengths in an output vector
    output(:,3) = stats(:,1); %place the mean calculated diameter in
       the output vector
    output(:,4) = stats(:,2);%place the standard deviation along a
       region of the wire in the output vector

    set(handles.dataTable,'Data',output);%load data into statsTable
    handles.data = output;

    % Choose default command line output for slider_gui
    handles.output = hObject;

    % Update handles structure
    guidata(hObject, handles);
end %end tableData

% --- Executes on button press in showPic.
function showPic_Callback(hObject, eventdata, handles)
    imshow(handles.current_pic, 'Parent', handles.largePic);
    %set(handles.largePic, 'Visible', 'on');
    set(handles.horizontalPic, 'Visible', 'off');
    cla(handles.horizontalPic);
    set(handles.widthPlot, 'Visible', 'off');
    cla(handles.widthPlot);
end %end showPic_Callback
```

```
% --- Executes on button press in showGraphs.
function showGraphs_Callback(hObject, eventdata, handles)
    cla(handles.largePic);
    set(handles.largePic, 'Visible', 'off');
    %set(handles.horizontalPic, 'Visible', 'on');
    imshow(handles.horz_pic, 'Parent', handles.horizontalPic);
    set(handles.widthPlot, 'Visible', 'on');
    plot(handles.current_datax, handles.current_datay, ...
        'Parent', handles.widthPlot);
    set(handles.widthPlot, 'xlim', [min(handles.diameters(:,1))...
        max(handles.diameters(:,1))]);
    set(handles.widthPlot, 'ylim', [min(handles.diameters(:,2))-20
        ...
        max(handles.diameters(:,2))+20]);

end %end showGraphs_Callback

% --- Executes on button press in calcDiameter.
function calcDiameter_Callback(hObject, eventdata, handles)
    %Takes in the handles and makes a picture based on the bins
    %returns the picture

    %creates a matrix to put the diameters for each row it scans
    diameters = zeros(size(handles.current_pic,1),2);
    currentRow = 1;

    bins = handles.current_pic;

    assignin('base', 'vert_plot', bins);
    left_side = [];
    right_side = [];
    %Loops over all the lines in the picture
    for k=1:size(bins,1)

       %Sets variables for each line
       started = false; bin2Count = 0; startPos = 0;
       bin3Count = 0; blankCount = 0; endPos = 0;
       crossSec = 0;
       tempArray = [];

       %Loops over all the columns in the current line (k)
       for j=1:size(bins,2)

           %If the bin contains a 1 start the diameter count or reset
           %all of the other counts
           if bins(k,j) == 1
               if ~started
```

```
                started = true;
                startPos = j;
            else
                endPos = j; bin2Count = 0;
                bin3Count = 0; blankCount = 0;
            end
        %bin2 count, will start the count if it reaches 10 then it
        %will stop the count
        elseif bins(k,j) > 0.6
            bin2Count = bin2Count+1;
            if ~started, started = true; startPos = j;
            elseif bin2Count < 11
                endPos = j; blankCount = 0;
            else
                started = false; bin2Count = 0;
                bin3Count = 0; blankCount = 0; crossSec = endPos-
                    startPos;
                tempArray=[tempArray; crossSec, startPos, endPos];
            end
        %bin3 count, will start the count till it reaches 5, then
            it
        %will stop the count
        elseif bins(k,j) > 0.3
            bin3Count = bin3Count+1;
            if ~started, started = true; startPos = j;
            elseif bin3Count < 6
                endPos = j; blankCount = 0;
            else
                started = false; bin2Count = 0;
                bin3Count = 0; blankCount = 0; crossSec = endPos-
                    startPos;
                tempArray=[tempArray; crossSec, startPos, endPos];
            end
        %Can only have 2 blank spaces in a row before the count
            will
        %stop
        elseif bins(k,j) < 1
            blankCount = blankCount+1;
            if blankCount > 3
                started = false; bin2Count = 0;
                bin3Count = 0; blankCount = 0; crossSec = endPos-
                    startPos;
                tempArray=[tempArray; crossSec, startPos, endPos];
            end
        end %end if-else statements for determining the bins
    end %end loop over columns
```

```
        %determins the max diameter for the current row
        [M, I] = max(tempArray(:,1));
        diameters(currentRow, 2) = M;
        diameters(currentRow,1) = k;
        currentRow = currentRow+1;
        left_side(k) = tempArray(I,2);
        right_side(k) = tempArray(I,3);
    end%end loop over rows


    assignin('base', 'left_side', left_side);
    assignin('base', 'right_side', right_side);
    assignin('base', 'scale', handles.nmPerPixel);
    handles.diameters = diameters.*handles.nmPerPixel;

    handles.current_datax = handles.diameters(:,1);
    handles.current_datay = handles.diameters(:,2);

    handles.originalx = handles.diameters(:,1);
    handles.originaly = handles.diameters(:,2);

    handles.horz_pic = imcrop(imrotate(handles.original_rot_pic,90)
        ,[0,350,...
         length(handles.original_rot_pic(:,2)),400]);
    imshow(handles.horz_pic, 'Parent', handles.horizontalPic);
    plot(handles.diameters(:,1), handles.diameters(:,2), 'Parent',
        handles.widthPlot);
    set(handles.widthPlot, 'XLim', [0 handles.diameters(end,1)]);
    set(handles.widthPlot, 'YLim', [min(handles.diameters(:,2))-5 max
        (handles.diameters(:,2))+5]);

    % Choose default command line output for slider_gui
    handles.output = hObject;

    % Update handles structure
    guidata(hObject, handles);

    showGraphs_Callback(hObject, eventdata, handles);

    % Choose default command line output for slider_gui
    handles.output = hObject;

    % Update handles structure
    guidata(hObject, handles);
end %end calcDiameter_Callback

% --- Executes on button press in showOriginal.
function showOriginal_Callback(hObject, eventdata, handles)
```

```
    handles.current_pic = handles.original_pic;
    showPic_Callback(hObject, eventdata, handles);
end %end showOriginal_Callback

% --- Executes on button press in showRot.
function showRot_Callback(hObject, eventdata, handles)
    handles.current_pic = handles.original_rot_pic;
    showPic_Callback(hObject, eventdata, handles);
end %end showRot_Callback

function bins=showThePic(handles)
    temp = handles.rot_pic;
    bin1 = handles.bin1_value;
    bin2 = handles.bin2_value;
    bin3 = handles.bin3_value;

    bin1_array = (temp > bin1);
    bin2_array = (temp > bin2);
    bin3_array = (temp > bin3);

    bins = (bin1_array+bin2_array+bin3_array)./3;
    imshow(bins,'Parent', handles.largePic);
    set(handles.horizontalPic, 'Visible', 'off');
    cla(handles.horizontalPic);
    set(handles.widthPlot, 'Visible', 'off');
    cla(handles.widthPlot);

    handles.current_pic = bins;
    handles.bin_pic = bins;

end %end showThePic

function scaleBarLength_Callback(hObject, eventdata, handles)
    % Hints: get(hObject,'String') returns contents of scaleBarLength
        as text
    %        str2double(get(hObject,'String')) returns contents of
       scaleBarLength as a double

    handles.mm = get(hObject,'String');

    % Choose default command line output for slider_gui
    handles.output = hObject;

    % Update handles structure
    guidata(hObject, handles);
end %end scaleBarLength_Callback

function scaleBarLength_CreateFcn(hObject, eventdata, handles)
```

```
    % Hint: edit controls usually have a white background on Windows.
    %       See ISPC and COMPUTER.
    if ispc && isequal(get(hObject,'BackgroundColor'), get(0,'
       defaultUicontrolBackgroundColor'))
        set(hObject,'BackgroundColor','white');
    end
end %end scaleBarLength_CreateFcn

 function scaleBar_CreateFcn(hObject, eventdata, handles)
 end %end scaleBar_CreateFcn

% --- Executes on button press in saveTable.
function saveTable_Callback(hObject, eventdata, handles)
    name = strrep(handles.fileName, '-', '_');
    temp = cellstr(name(11:end-4));
    answer = inputdlg('Variable Save Name', '', 1, temp);
    data = get(handles.dataTable, 'Data');
    z0 = ones(length(data(:,1)), 1);
    data(:,2) = [];
    data = [data, z0];

    holder = [0, 0, 0, 0];
    for i=1:length(data(:,1))
        r = find(holder(:,1)==data(i,1));
        if r ~= 0
            holder(r,2) = (holder(r,2)*holder(r,4)+data(i,2))/(holder
               (r,4)+data(i,4));
            holder(r,3) = (holder(r,3)*holder(r,4)+data(i,3))/(holder
               (r,4)+data(i,4));
            holder(r,4) = holder(r,4)+data(i,4);
        else
            holder = [holder; data(i,:)];
        end %end if-else
    end %end for
    holder = sortrows(holder(:,1:4));
    holder = num2cell(holder);
    output{1,1} = 'Doping Level';
    output{1,2} = 'Segment Diameter';
    output{1,3} = 'Std Dev';
    output{1,4} = 'Number Averaged';
    output = [output; holder];


    uni = unique(data(:,1));
    neg1 = uni == -1;
    uni(neg1) = [];

    for i = 1:length(uni)
```

```
        cell{i,1} = uni(i);
        cell{i,2} = [];
    end %end for

    minmax = find(handles.minmax==1);
    minmax = [1;minmax;length(handles.minmax)];
    for i =1:length(data(:,1))
        if data(i,1) ~= -1
            r = find(uni==data(i,1));
            if isempty(cell{r,2})
                cell{r,2} = handles.diameters(minmax(i):minmax(i+1)
                    ,:);
                cell{r,3} = handles.diameters(minmax(i):minmax(i+1)
                    ,:);
            else
                cell{r,2} = [cell{r,2}; handles.diameters(minmax(i):
                    minmax(i+1),:)];
                cell{r,3} = [cell{r,3}; 0, 0; handles.diameters(
                    minmax(i):minmax(i+1),:)];
            end %end if-else
        end %end if
    end %end for

    for i=1:length(cell(:,1))
        struct(i).dopingLevel = cell{i,1};
        struct(i).segData = cell{i,2};
        struct(i).segLength = cell{i,3};
    end %end for
    assignin('base', answer{1}, struct);

end %end saveTable_Callback

% --- Executes during object creation, after setting all properties.
function saveTable_CreateFcn(hObject, eventdata, handles)
end %end saveTable_CreateFcn

%%%%%%%%%%%%%%%%%%%%%%%%%%%%%%%%%%%%%%%%%%%%%%%%%%%%%%%%%%%%%%%%%%%%%%%%%%
%These methods are used for navigation through files including
%Showing the current file name (fileNameString_Callback),
%Moving to the next file (nextButton_Callback), and
%Moving to the previous file (prevButton_Callback)
%%%%%%%%%%%%%%%%%%%%%%%%%%%%%%%%%%%%%%%%%%%%%%%%%%%%%%%%%%%%%%%%%%%%%%%%%%

function open_ClickedCallback(hObject, eventdata, handles)
    [fileName, filePath, filterIndex] = uigetfile(strcat(handles.
        filePath, '*.tif'));

    %Skips opening if cancel is clicked
```

```
    if fileName == 0
        return
    end %end if
    handles.filePath = filePath;
    handles.fileName = fileName;
    set(handles.fileNameString, 'String', strcat(filePath, fileName))
       ;
    pic = imread(strcat(filePath, fileName), 'tiff');
    if numel(pic(1,1,:))==3, pic = rgb2gray(pic); end
    handles.original_pic = im2double(pic);
    handles.current_pic = handles.original_pic;

    showPic_Callback(hObject, eventdata, handles);

    % Choose default command line output for slider_gui
    handles.output = hObject;

    % Update handles structure
    guidata(hObject, handles);
end %end open_ClickedCallback

function save_ClickedCallback(hObject, eventdata, handles)

    folder_name = uigetdir(handles.filePath);

    %Skips saving if cancel is clicked
    if folder_name == 0
        return
    end %end if

    cell_array = {};
    cell_array{1} = handles.fileName(1:end-4);
    savename = inputdlg('Base␣Save␣File␣Name:', 'Save␣File',1,
       cell_array);

    %Skips saving if cancel is clicked
    if isempty(savename)
        return;
    end %end if
    savename = strcat('\',savename{1});

    newPic = handles.original_rot_pic(:,:);
    [r,c] = find(newPic>1);
    newPic(r,c) = 1;
    filename = strcat(folder_name,savename,'_original_rot_pic.tif');

    newPic = handles.bin_pic(:,:);
    [r,c] = find(newPic>1);
```

```
    newPic(r,c) = 1;
    filename = strcat(folder_name,savename,'_rot_pic.tif');

    temp = {'Length', 'Mean Diameter', 'Standard Deviation'};
    v1 = genvarname(strcat(savename(2:end), '_dataTable_header'));
    v2 = genvarname(strcat(savename(2:end), '_dataTable'));
    v3 = genvarname(strcat(savename(2:end), '_plotData'));
    v4 = genvarname(strcat(savename(2:end), '_transitions'));
    v5 = genvarname(strcat(savename(2:end), '_horizontalPic'));
    eval([v1 '= temp;'])
    eval([v2 '= handles.data;'])
    eval([v3 '= handles.diameters;'])
    eval([v4 '= handles.transitions;'])
    eval([v5 '= handles.horz_pic;'])

    save(strcat(folder_name,savename), v1, v2, v3, v4, v5);
end %end save_ClickedCallback

function fileNameString_Callback(hObject, eventdata, handles)
end %end fileNameString_Callback

% --- Executes during object creation, after setting all properties.
function fileNameString_CreateFcn(hObject, eventdata, handles)
    % Hint: edit controls usually have a white background on Windows.
    %       See ISPC and COMPUTER.
    if ispc && isequal(get(hObject,'BackgroundColor'), get(0,'
        defaultUicontrolBackgroundColor'))
         set(hObject,'BackgroundColor','white');
    end
end %end fileNameString_CreateFcn

% --- Executes on button press in nextButton.
function nextButton_Callback(hObject, eventdata, handles)
    temp = dir(fullfile(handles.filePath, '*.tif'));

    %Check for the next .tif image in the folder
    for i=1:length(temp)
        if strcmp(temp(i).name, handles.fileName)
            if i<length(temp)
                handles.fileName = temp(i+1).name;
            else
                handles.fileName = temp(1).name;
            end %end if-else
            break;
        end %end if
    end %end for

    %Sets the handles and reads in the new file
```

```
    set(handles.fileNameString, 'String', strcat(handles.filePath,
        handles.fileName));
    pic = imread(strcat(handles.filePath, handles.fileName), 'tiff');
    if numel(pic(1,1,:))==3, pic = rgb2gray(pic); end
    handles.original_pic = im2double(pic);
    handles.current_pic = handles.original_pic;

    showPic_Callback(hObject, eventdata, handles);

    % Choose default command line output for slider_gui
    handles.output = hObject;

    % Update handles structure
    guidata(hObject, handles);
end %end nextButton_Callback

% --- Executes during object creation, after setting all properties.
function nextButton_CreateFcn(hObject, eventdata, handles)
end %end nextButton_CreateFcn

% --- Executes on button press in prevButton.
function prevButton_Callback(hObject, eventdata, handles)
    temp = dir(fullfile(handles.filePath, '*.tif'));

    %Check for the previous .tif image in the folder
    for i=1:length(temp)
        if strcmp(temp(i).name, handles.fileName)
            if i>1
                handles.fileName =  temp(i-1).name;
            else
                handles.fileName =  temp(length(temp)).name;
            end %end if-else
            break;
        end %end if
    end %end for

    %Sets the handles and reads in the new file
    set(handles.fileNameString, 'String', strcat(handles.filePath,
        handles.fileName));
    pic = imread(strcat(handles.filePath, handles.fileName), 'tiff');
    if numel(pic(1,1,:))==3, pic = rgb2gray(pic); end
    handles.original_pic = im2double(pic);
    handles.current_pic = handles.original_pic;

    %Shows the picture
    showPic_Callback(hObject, eventdata, handles);

    % Choose default command line output for slider_gui
```

```
    handles.output = hObject;

    % Update handles structure
    guidata(hObject, handles);
end %end prevButton_Callback

% --- Executes during object creation, after setting all properties.
function prevButton_CreateFcn(hObject, eventdata, handles)
end %end prevButton_CreateFcn


%%%%%%%%%%%%%%%%%%%%%%%%%%%%%%%%%%%%%%%%%%%%%%%%%%%%%%%%%%%%%%%%%%%%%%%%%
% END nanoWireDiameter.m
%%%%%%%%%%%%%%%%%%%%%%%%%%%%%%%%%%%%%%%%%%%%%%%%%%%%%%%%%%%%%%%%%%%%%%%%%

%Function that allows the user to edit transitions lines. Left click
    and
%hold to move the lines around. While moving around a line use 'd' to
%delete the line. Use space bar to exit and return to
    nanoWireDiameter
function xVal = linePlot(diameters, pic, nmPerPixel, lines)
    %Initialize variables
    j = 1; lineTag = 0; lineTag2 = 0; currentLineTag = 0; deleted =
        [];

    %Set up the figure
    figure

    %make a subplot that contains 2 rows and 1 column
    a = subplot(2,1,1);

    %plot the graph of diameters
    plot(diameters(:,1), diameters(:,2));
    set(a, 'XLim', [0 diameters(end,1)]);
    set(a, 'YLim', [min(diameters(:,2))-5 max(diameters(:,2))+5]);

    %get the position of the graph. 1=left, 2=bottom, 3=width, 4=
        height.
    %All measured from the bottom left corner
    pos1 = get(a, 'Position');

    %second plot
    b = subplot(2,1,2);
    aspectRatio1 = pos1(4)/pos1(3);
    height = aspectRatio1*numel(pic(1,:));
    [row col] = find(pic>1);

    %Makes all the values greater than 1 now equal to 1
```

```
for i = 1:numel(row)
    pic(row(i), col(i)) = 1;
end %end for

%project the current picture to 3 more dimensions for RGB
if numel(pic(:,1))>height
    newPic = pic((numel(pic(:,1))-height)/2:(numel(pic(:,1))+
        height)/2,:);
else
    newPic = pic(:,:);
end %end if-else
newPic(:,:,2) = newPic(:,:);
newPic(:,:,3) = newPic(:,:,2);

%Sets the position of picture. image as opposed to imshow makes
    this
%work
h = image(newPic);
pos2 = get(b, 'Position');
pos2(3) = pos1(3);
pos2(2) = pos1(2) - pos2(4);
set(b, 'Position', pos2);


if nargin == 4
    for i = 1:numel(lines(:,1))
        yLim = get(a, 'ylim');
        l = line([lines(i,1)*nmPerPixel lines(i,1)*nmPerPixel],
            yLim, 'Color', 'red',...
              'tag',strcat('line', int2str(j)));
        set(l, 'parent', a)
        yLim = get(b, 'yLim');
        l = line([lines(i,1) lines(i,1)],yLim,...
            'Color', 'red', 'tag',strcat('line', int2str(j),'_2')
                );
        set(l, 'parent', b);
        j = j+1;
    end %end for
end %end if

%Sets the functions to be called for button press and mouse click
    . Also
%waits for the @endAndOutput function to call uiresume.
set(gcf,'WindowButtonDownFcn',@createLine)
set(gcf,'KeyPressFcn', @endAndOutput)
uiwait(gcf);
```

```
%This function makes a line or finds the closest line to the
   mouse
%click to determine the line to be moved.
function createLine(src, event)

    %This first part will create a line for a left click
    if strcmp(get(src,'SelectionType'),'alt')
        clicked=get(gca,'currentpoint');
        xcoord=clicked(1,1,1);
        yLim = get(a, 'ylim');
        line([xcoord xcoord],yLim, 'Color', 'red',...
            'tag',strcat('line', int2str(j)));
        yLim = get(b, 'yLim');
        l = line([xcoord/nmPerPixel xcoord/nmPerPixel],yLim,...
            'Color', 'red', 'tag',strcat('line', int2str(j),'_2')
               );
        set(l, 'parent', b);
        j = j+1;

    %This else part cycles through all the lines and picks which
       one is
    %closest in order to pick which line to drag
    else
        clicked=get(gca,'currentpoint');
        xcoord=clicked(1,1,1);
        minDist = inf;
        for i=1:j-1
            if ~any(deleted == i)
                l1 = findobj(a, 'tag', strcat('line', int2str(i))
                    );
                l2 = findobj(b, 'tag', strcat('line', int2str(i),
                    '_2'));
                lineX = get(l1, 'xdata');
                lineX = lineX(1,1);
                if abs(lineX-xcoord) < minDist
                    minDist = abs(lineX-xcoord);
                    lineTag = l1;
                    lineTag2 = l2;
                    currentLineTag = i;
                end %end if distance is smaller than the current
                    min distance
            end %end for determining if the line was deleted
        end %end looping over all the lines

        set(gcf,'windowbuttonmotionfcn',@moveLine)
        set(gcf,'KeyPressFcn', @deleteLine)
        set(gcf,'windowbuttonupfcn',@moveDone)
    end %end if right click or left click
```

```
end %end createLine function

%Drags the line while the left click is depressed
function moveLine(src, event)
    clicked=get(gca,'currentpoint');
    xcoord=clicked(1,1,1);
    set(lineTag,'xdata',[xcoord xcoord]);
    set(lineTag2,'xdata',[xcoord/nmPerPixel xcoord/nmPerPixel]);
end %end moveLine function

%Resets the functions after the left click is released
function moveDone(src, event)
    set(gcf,'windowbuttonmotionfcn','')
    set(gcf,'windowbuttonupfcn','')
    set(gcf,'KeyPressFcn', @endAndOutput)
end %end moveDone function

%Use space bar to exit the program
function endAndOutput(src, event)
    if strcmp(event.Character, ' ')
        k = 1;
        for i=1:j-1
            if ~any(deleted == i)
                temp = findobj(gcf, 'tag', strcat('line', int2str
                    (i)));
                temp2 = get(temp, 'xdata');
                xVal(k,1) = k;
                xVal(k,2) = temp2(1,1);
                k = k+1;
            end %end if line has been deleted
        end %end loop over all lines
        xVal = sortrows(xVal, 2);
        uiresume(gcf);
        close;
    end %end if the keypress was a space
end %end endAndOutput function

%use the 'd' key while a line is selected to delete it
function deleteLine(src, event)
    if strcmp(event.Character, 'd')
        delete(lineTag);
        delete(lineTag2);
        deleted = [deleted currentLineTag];
        set(gcf,'windowbuttonmotionfcn','')
        set(gcf,'windowbuttonupfcn','')
        set(gcf,'KeyPressFcn', @endAndOutput)
    end %end if key press was d
```

```
    end %end deleteLine function

end %end xVal = linePlot function

function [ space ] = CreateGaussScaleSpace( data, deriv, scales )
% space = CreateGaussScaleSpace( data, deriv, scales )
% Computes the Gaussian scale space of a 1D data set.  (Scale
   parameters
% are in data-spacing units.)
% Input:
%   data         A 1D data set
%   deriv        The order of Gaussian scale space to compute (e.g. 0
   is a
%                smoothing scale space; 1 is an edge detecting scale
   space)
%   scales       A list (vector) of scales to compute
% Output:
%   space        A scale space representation of the input data

% defaults
if (nargin < 3)
    scales = 1:20;
end
if (nargin < 2)
    deriv = 0;
end

for i = 1:length(scales)
    scale = scales(i);

    % Find the gaussian kernel, convolve
    g = GaussianKernel1D(scale, deriv);

    % we have to pad the data to avoid the derivative blowing up at
       the
    % boundaries
    padData = [data(1)*ones(length(g),1); data; data(end)*ones(length
       (g),1)];
    fData = conv(padData, g);

    % Resize the filtered data
    offset = (length(fData) - length(data)) / 2;
    fData = fData(offset:offset+length(data)-1);
    space(:,i) = fData;
end;

function [ kernel ] = GaussianKernel1D( scale, deriv, width )
% GaussianKernel1D( sigma, deriv, width ) Creates a centered Gaussian
```

```
% kernel of the specified derivative order and the specified scale.
   The
% width parameter specifies how many sigma from the center the kernel
% should extend.
if (nargin < 3)
    width = 3;
end;
% sigma = sqrt(scale/(2*pi));
sigma = scale;
range = 1:2*width*(ceil(sigma)) + 1;
center = range(ceil(length(range)/2));
derivs(1,1:length(range)) = 1;
derivs(2,1:length(range)) = -((range-center)/(sigma^2));
derivs(3,1:length(range)) = ((range-center).^2 - (sigma^2))/(sigma^4)
   ;
derivs(4,1:length(range)) = -((range-center).^3 - 3 * (sigma^2) * (
   range-center))/(sigma^6);
derivs(5,1:length(range)) = ((range-center).^4 - 6 * (sigma^2) * (
   range-center).^2 + 3 * (sigma^4))/(sigma^8);
kernel = (1/(sigma*sqrt(2*pi))) * exp(-((range-center).^2)/(2*sigma
   ^2));
kernel = kernel .* derivs(deriv+1,:);

function [ extrema ] = FindLocalExtrema( data, threshold, scale,
   regions )
% maxmin = FindLocalExtrema( data )
% Finds locally maximal or minimal values in the y direction of the
   given
% data.
%
% Input:
%   data         1D data array (image)
%   threshold    What fraction of total maximum or minimum a data
   point
%                needs to be for consideration (non-maximum supression
   )
%   scale        Specifies the number of data points in a local
   neighborhood
%                (neighborhood legth is 2 * scale + 1)
%   regions      Specifies a set of regions to look in--if not
   supplied,
%                the whole data region will be searched
% Output:
%   extrema      a vector the same size as the input data with value 1
    at
%                input data maxima and minima, 0 elsewhere

if (nargin < 3)
```

```
    scale = 1;
end
if (nargin < 2)
    threshold = 0.5;
end

% rescale data
rdataMax = data / max(data);
rdataMin = data / min(data);

winmax = zeros(size(data));
winmin = zeros(size(data));

% Note: It would have been nice to do the follwing as a vector
   operation,
% even within the min/max detection below.  For reasons opaque to me,
    the
% max() function doesn't seem to work in a vector operation.  We
   wanted
% something like:
% winmax(ii) = max(rdataMax(ii-scale:ii+scale));
% But, this seems to generate a vector mostly of, almost like the
   maximum
% is being applied cummulatively. Oh, well...this isn't too slow if
   the
% data are not too big.
% create a sliding window min & max
for i = 1+scale:size(data,1)-scale
    winmax(i) = max(rdataMax(i-scale:i+scale));
    winmin(i) = max(rdataMin(i-scale:i+scale));
end

maxima = zeros(size(data));
minima = zeros(size(data));

% find the local minima and maxima
if (nargin < 4)      % regions not defined--search everywhere
    ii = (1+scale:size(data,1)-scale)';
    maxima(ii) = rdataMax(ii) >= threshold & rdataMax(ii) >= winmax(
        ii);
    minima(ii) = rdataMin(ii) >= threshold & rdataMin(ii) >= winmin(
        ii);
else                 % only search in specified regions
    for i = 1:length(regions)
        ii = (max(1+scale, regions(i)-scale):min(size(data,1)-scale,
            regions(i)+scale))';
        maxima(ii) = rdataMax(ii) >= threshold & rdataMax(ii) >=
            winmax(ii);
```

```
        minima(ii) = rdataMin(ii) >= threshold & rdataMin(ii) >=
            winmin(ii);
    end
end

% combine min and max
extrema = maxima + minima;

function [ stats ] = RegionStats( data, regionIdx, radius )
% [ stats ] = RegionStats( data, regionIdx )
% Finds statistics for data broken up into distinct regions.
% Input:
%   data        The data to analyze
%   regionIdx   The indices that demarcate distinct data regions
%   radius      The radius of transition regions (data within
  transition
%               regions is excluded from statistics)

if (nargin < 3)
    radius = 1;
end

region = 1:regionIdx(1)-radius;
stats(1, :) = [mean(data(region)), std(data(region))];
for i = 2:length(regionIdx)
    region = regionIdx(i-1)+radius:regionIdx(i)-radius;
    stats(i, :) = [mean(data(region)), std(data(region))];
end
region = regionIdx(end)+radius:length(data);
stats(end+1, :) = [mean(data(region)), std(data(region))];
```

REFERENCES

1. Brinkman, W., Haggan, D. & Troutman, W. A History of the Invention of the Transistor and Where It Will Lead Us. *IEEE J. Solid-State Circuits* **32,** 1858–1865 (1997).

2. Arns, R. The Other Transistor: Early History of the Metal-Oxide Semiconductor Field-Effect Transistor. *Eng. Sci. Educ. J.* **7,** 233–240 (1998).

3. Moore, G. E. Cramming More Components Onto Integrated Circuits. *Proc. IEEE* **86,** 82–85 (1998).

4. Harriott, L. R. Limits of Lithography. *Proc. IEEE* **89,** 366–374 (2001).

5. Wagner, C. & Harned, N. EUV Lithography: Lithography Gets Extreme. *Nat. Photonics* **4,** 24–26 (2010).

6. Pimpin, A. & Srituravanich, W. Review on Micro- and Nanolithography Techniques and their Applications. *Eng. J.* **16,** 37–56 (2012).

7. Sanders, D. P. Advances in Patterning Materials for 193 nm Immersion Lithography. *Chem. Rev.* **110,** 321–360 (2010).

8. Manfrinato, V. R. *et al.* Resolution Limits of Electron-Beam Lithography toward the Atomic Scale. *Nano Lett.* **13,** 130321102652000 (2013).

9. Broers, A. N., Hoole, A. C. F. & Ryan, J. M. Electron Beam Lithography–Resolution Limits. *Microelectron. Eng.* **32,** 131–142 (1996).

10. Hoy, J., Morrison, P. J., Steinberg, L. K., Buhro, W. E. & Loomis, R. A. Excitation Energy Dependence of the Photoluminescence Quantum Yields of Core and Core/Shell Quantum Dots. *J. Phys. Chem. Lett.* **4,** 2053–2060 (2013).

11. Zhang, J. Z., Cooper, J. K. & Gul, S. Rational Codoping as a Strategy to Improve Optical Properties of Doped Semiconductor Quantum Dots. *J. Phys. Chem. Lett.* **5,** 3694–3700 (2014).

12. Tang, J. *et al.* Colloidal-Quantum-Dot Photovoltaics using Atomic-Ligand Passivation. *Nat. Mater.* **10,** 765–771 (2011).

13. Kamat, P. V. Quantum Dot Solar Cells. The Next Big Thing in Photovoltaics. *J. Phys. Chem. Lett.* **4,** 908–918 (2013).

14. Kamat, P. V. Quantum Dot Solar Cells. Semiconductor Nanocrystals as Light Harvesters. *J. Phys. Chem. C* **112,** 18737–18753 (2008).

15. Shirasaki, Y., Supran, G. J., Bawendi, M. G. & Bulović, V. Emergence of Colloidal Quantum-Dot Light-Emitting Technologies. *Nat. Photonics* **7,** 13–23 (2012).

16. Knauf, R. R., Brennaman, M. K., Alibabaei, L., Norris, M. R. & Dempsey, J. L. Revealing the Relationship between Semiconductor Electronic Structure and Electron Transfer Dynamics at Metal Oxide–Chromophore Interfaces. *J. Phys. Chem. C* **117,** 25259–25268 (2013).

17. Hines, D. a. & Kamat, P. V. Recent Advances in Quantum Dot Surface Chemistry. *ACS Appl. Mater. Interfaces* **6,** 3041–3057 (2014).

18. Novoselov, K. S. Electric Field Effect in Atomically Thin Carbon Films. *Science* **306,** 666–669 (2004).

19. Novoselov, K. S. *et al.* A Roadmap for Graphene. *Nature* **490,** 192–200 (2012).

20. Jariwala, D., Sangwan, V. K., Lauhon, L. J., Marks, T. J. & Hersam, M. C. Emerging Device Applications for Semiconducting Two-Dimensional Transition Metal Dichalcogenides. *ACS Nano* **8,** 1102–1120 (2014).

21. Wagner, R. S. & Ellis, W. C. Vapor-Liquid-Solid Mechanism of Single Crystal Growth. *Appl. Phys. Lett.* **4,** 89 (1964).

22. Cui, Y., Lauhon, L. J., Gudiksen, M. S., Wang, J. & Lieber, C. M. Diameter-Controlled Synthesis of Single-Crystal Silicon Nanowires. *Appl. Phys. Lett.* **78,** 2214 (2001).

23. Lauhon, L. J., Gudiksen, M. S. & Lieber, C. M. Semiconductor Nanowire Heterostructures. *Philos. Trans. R. Soc. London Ser. a-Mathematical Phys. Eng. Sci.* **362,** 1247–1260 (2004).

24. Shin, N., Chi, M. & Filler, M. a. Sidewall Morphology-Dependent Formation of Multiple Twins in Si Nanowires. *ACS Nano* **7,** 8206–8213 (2013).

25. Caroff, P. *et al.* Controlled Polytypic and Twin-plane Superlattices in III–V Nanowires. *Nat. Nanotechnol.* **4,** 50–5 (2009).

26. Shin, N., Chi, M. & Filler, M. a. Interplay between Defect Propagation and Surface Hydrogen in Silicon Nanowire Kinking Superstructures. *ACS Nano* **8,** 3829–35 (2014).

27. Algra, R. E. *et al.* Twinning Superlattices in Indium Phosphide Nanowires. *Nature* **456,** 369–372 (2008).

28. Bierman, M. J., Lau, Y. K. A., Kvit, A. V., Schmitt, A. L. & Jin, S. Dislocation-Driven Nanowire Growth and Eshelby Twist. *Science* **320,** 1060–3 (2008).

29. Zhu, J. *et al.* Formation of Chiral Branched Nanowires by the Eshelby Twist. *Nat. Nanotechnol.* **3,** 477–481 (2008).

30. Lau, Y. K. A., Chernak, D. J., Bierman, M. J. & Jin, S. Formation of PbS Nanowire Pine Trees Driven by Screw Dislocations. *J. Am. Chem. Soc.* **131,** 16461–16471 (2009).

31. Jiming, B. *et al.* Optical Properties of Rotationally Twinned InP Nanowire Heterostructures. *Nano Lett.* **8,** 836–841 (2008).

32. Ikonić, Z., Srivastava, G. P. & Inkson, J. C. Electronic Properties of Twin Boundaries and Twinning Superlattices in Diamond-Type and Zinc-blende-type Semiconductors. *Phys. Rev. B* **48,** 17181–17193 (1993).

33. Stiles, M. D. & Hamann, D. R. Electron Transmission through Silicon Stacking Faults. *Phys. Rev. B* **41,** 5280–5282 (1990).

34. Stiles, M. D. & Hamann, D. R. Ballistic Electron Transmission through Interfaces. *Phys. Rev. B* **38,** 2021–2037 (1988).

35. Assali, S. *et al.* Direct Band Gap Wurtzite Gallium Phosphide Nanowires. *Nano Lett.* **13,** 1559–1563 (2013).

36. Lee, G. *et al.* Directionally Integrated VLS Nanowire Growth in a Local Temperature Gradient. *Angew. Chemie Int. Ed.* **48,** 7366–7370 (2009).

37. Madras, P., Dailey, E. & Drucker, J. Kinetically Induced Kinking of Vapor–Liquid–Solid Grown Epitaxial Si Nanowires. *Nano Lett.* **9,** 3826–3830 (2009).

38. Wagner, R. S. & Doherty, C. J. Mechanism of Branching and Kinking During VLS Crystal Growth. *J. Electrochem. Soc.* **115,** 93–99 (1968).

39. Tian, B., Xie, P., Kempa, T. J., Bell, D. C. & Lieber, C. M. Single-Crystalline Kinked Semiconductor Nanowire Superstructures. *Nat. Nanotechnol.* **4,** 824–829 (2009).

40. Lugstein, A. *et al.* Pressure-Induced Orientation Control of the Growth of Epitaxial Silicon Nanowires. *Nano Lett.* **8,** 2310–2314 (2008).

41. Dailey, E., Madras, P. & Drucker, J. Composition and Growth Direction Control of Epitaxial Vapor–Liquid–Solid-Grown SiGe Nanowires. *Appl. Phys. Lett.* **97,** 143106 (2010).

42. Wang, J. *et al.* Reversible Switching of InP Nanowire Growth Direction by Catalyst Engineering. *Nano Lett.* **13,** 3802–6 (2013).

43. Kawashima, T. *et al.* Control of Surface Migration of Gold Particles on Si Nanowires. *Nano Lett.* **8,** 362–368 (2008).

44. Musin, I. R. & Filler, M. a. Chemical Control of Semiconductor Nanowire Kinking and Superstructure. *Nano Lett.* **12,** 3363–3368 (2012).

45. Kodambaka, S., Hannon, J. B., Tromp, R. M. & Ross, F. M. Control of Si Nanowire Growth by Oxygen. *Nano Lett.* **6,** 1292–1296 (2006).

46. Sivaram, S. V., Shin, N., Chou, L.-W. & Filler, M. a. Direct Observation of Transient Surface Species during Ge Nanowire Growth and Their Influence on Growth Stability. *J. Am. Chem. Soc.* 150730100807008 (2015).

47. Madras, P., Dailey, E. & Drucker, J. Spreading of Liquid AuSi on Vapor–Liquid–Solid-Grown Si Nanowires. *Nano Lett.* **10,** 1759–1763 (2010).

48. Shin, N. & Filler, M. a. Controlling Silicon Nanowire Growth Direction Via Surface Chemistry. *Nano Lett.* **12,** 2865–70 (2012).

49. Musin, I. R., Shin, N. & Filler, M. a. Diameter Modulation as a Route to Probe the Vapour–Liquid–Solid Growth Kinetics of Semiconductor Nanowires. *J. Mater. Chem. C* **2,** 3285–3291 (2014).

50. Musin, I. R., Boyuk, D. S. & Filler, M. a. Surface Chemistry Controlled Diameter-modulated Semiconductor Nanowire Superstructures. *J. Vac. Sci. Technol. B Microelectron. Nanom. Struct.* **31,** 020603 (2013).

51. Gentile, P. *et al.* Effect of HCl on the Doping and Shape Control of Silicon Nanowires. *Nanotechnology* **23,** 215702 (2012).

52. Amit, I. *et al.* Spatially Resolved Correlation of Active and Total Doping Concentrations in VLS Grown Nanowires. *Nano Lett.* **13,** 2598–2604 (2013).

53. Schlitz, R. A., Perea, D. E., Lensch-Falk, J. L., Hemesath, E. R. & Lauhon, L. J. Correlating Dopant Distributions and Electrical Properties of Boron-Doped Silicon Nanowires. *Appl. Phys. Lett.* **95** (2009).

54. Perea, D. E. *et al.* Direct Measurement of Dopant Distribution in an Individual Vapour–Liquid–Solid Nanowire. *Nat. Nanotechnol.* **4,** 315–319 (2009).

55. Tutuc, E., Chu, J. O., Ott, J. A. & Guha, S. Doping of Germanium Nanowires Grown in Presence of PH_3. *Appl. Phys. Lett.* **89,** 263101 (2006).

56. Pinion, C. W., Christesen, J. D. & Cahoon, J. F. Understanding the Vapor–Liquid–Solid Mechanism of Si Nanowire Growth and Doping to Synthetically Encode Precise Nanoscale Morphology. *J. Mater. Chem. C* **4,** 3890–3897 (2016).

57. Hilse, M., Ramsteiner, M., Breuer, S., Geelhaar, L. & Riechert, H. Incorporation of the Dopants Si and Be into GaAs Nanowires. *Appl. Phys. Lett.* **96,** 193104 (2010).

58. Clark, T. E. *et al.* Diameter Dependent Growth Rate and Interfacial Abruptness in Vapor-Liquid-Solid Si/Si1-xGex Heterostructure Nanowires. *Nano Lett.* **8,** 1246–1252 (2008).

59. Wu, Y., Fan, R. & Yang, P. Block-by-Block Growth of Single-Crystalline Si/SiGe Superlattice Nanowires. *Nano Lett.* **2,** 83–86 (2002).

60. Amato, M., Palummo, M., Rurali, R. & Ossicini, S. Silicon-Germanium Nanowires: Chemistry and Physics in Play, from Basic Principles to Advanced Applications. *Chem. Rev.* **114,** 1371–412 (2014).

61. Ohlsson, B. *et al.* Growth and Characterization of GaAs and InAs Nano-Whiskers and InAs/GaAs Heterostructures. *Phys. E Low-dimensional Syst. Nanostructures* **13,** 1126–1130 (2002).

62. Hiruma, K. *et al.* Growth and Optical Properties of Nanometerscale GaAs and InAs Whiskers. *J. Appl. Phys.* **77,** 447–462 (1995).

63. Perea, D., Li, N., Dickerson, R., Misra, A. & Picraux, S. Controlling Heterojunction Abruptness in VLS-Grown Semiconductor Nanowires via in situ Catalyst Alloying. *Nano Lett.* **11,** 3117–3122 (2011).

64. Wen, C. Y., Tersoff, J., Reuter, M. C., Stach, E. A. & Ross, F. M. Step-Flow Kinetics in Nanowire Growth. *Phys. Rev. Lett.* **105,** 195502 (2010).

65. Wen, C. Y. *et al.* Formation of Compositionally Abrupt Axial Heterojunctions in Silicon-Germanium Nanowires. *Science* **326,** 1247–1250 (2009).

66. Cohen-Karni, T. *et al.* Synthetically Encoded Ultrashort-Channel Nanowire Transistors for Fast, Pointlike Cellular Signal Detection. *Nano Lett.* **12,** 2639–44 (2012).

67. Dick, K., Bolinsson, J., Borg, B. & Johansson, J. Controlling the Abruptness of Axial Heterojunctions in III–V Nanowires: Beyond the Reservoir Effect. *Nano Lett.* **12,** 3200–3206 (2012).

68. Thelander, C. *et al.* Nanowire-Based One-Dimensional Electronics. *Mater. today* **9,** 28–35 (2006).

69. Gudiksen, M. S., Lauhon, L. J., Wang, J., Smith, D. C. & Lieber, C. M. Growth of Nanowire Superlattice Structures for Nanoscale Photonics and Electronics. *Nature* **415,** 617–20 (2002).

70. Nylund, G., Storm, K., Lehmann, S., Capasso, F. & Samuelson, L. Designed Quasi-1D Potential Structures Realized in Compositionally Graded $InAs_{1-x}P_x$ Nanowires. *Nano Lett.* **16,** 1017–1021 (2016).

71. Thelander, C. *et al.* Single-Electron Rransistors in Heterostructure Nanowires. *Appl. Phys. Lett.* **83,** 2052 (2003).

72. Bjork, M. T. *et al.* Nanowire Resonant Tunneling Diodes. *Appl. Phys. Lett.* **81,** 4458 (2002).

73. Yan, R., Gargas, D. & Yang, P. Nanowire Photonics. *Nat. Photonics* **3,** 569–576 (2009).

74. Lieber, C. M. & Wang, Z. L. Functional Nanowires. *MRS Bull.* **32,** 99–108 (2007).

75. Huang, Y., Duan, X. & Lieber, C. M. Nanowires for Integrated Multicolor Nanophotonics. *Small* **1,** 142–147 (2004).

76. Guo, W., Banerjee, A., Bhattacharya, P. & Ooi, B. S. InGaN/GaN Disk-in-Nanowire White Light Emitting Diodes on (001) Silicon. *Appl. Phys. Lett.* **98,** 193102 (2011).

77. Duan, X., Huang, Y., Agarwal, R. & Lieber, C. M. Single-Nanowire Electrically Driven Lasers. *Nature* **421,** 241–245 (2003).

78. Huang, M. H. *et al.* Room-Temperature Ultraviolet Nanowire Nanolasers. *Science* **292,** 1897–1899 (2001).

79. Saxena, D. *et al.* Optically Pumped Room-Temperature GaAs Nanowire Lasers. *Nat. Photonics* **7,** 963–968 (2013).

80. Claudon, J. *et al.* A Highly Efficient Single-Photon Source Based on a Quantum Dot in a Photonic Nanowire. *Nat Phot.* **4,** 174–177 (2010).

81. Kempa, T. J. *et al.* Coaxial Multishell Nanowires with High-Quality Electronic Interfaces and Tunable Optical Cavities for Ultrathin Photovoltaics. *Proc. Natl. Acad. Sci.* **109,** 1407–1412 (2012).

82. Kim, S.-K. *et al.* Doubling Absorption in Nanowire Solar Cells with Dielectric Shell Optical Antennas. *Nano Lett.* **15,** 753–758 (2015).

83. Zhang, X. *et al.* Horizontal Silicon Nanowires with Radial p–n Junctions: A Platform for Unconventional Solar Cells. *J. Phys. Chem. Lett.* **4,** 2002–2009 (2013).

84. Hayden, O., Agarwal, R. & Lieber, C. M. Nanoscale Avalanche Photodiodes for Highly Sensitive and Spatially Resolved Photon Detection. *Nat. Mater.* **5,** 352–356 (2006).

85. Yang, C., Barrelet, C. J., Capasso, F. & Lieber, C. M. Single p-Type/Intrinsic/n-Type Silicon Nanowires as Nanoscale Avalanche Photodetectors. *Nano Lett.* **6,** 2929–2934 (2006).

86. Kayes, B. M., Atwater, H. A. & Lewis, N. S. Comparison of the Device Physics Principles of Planar and Radial p-n Junction Nanorod Solar Cells. *J. Appl. Phys.* **97,** 114302 (2005).

87. Wallentin, J. *et al.* InP Nanowire Array Solar Cells Achieving 13.8% Efficiency by Exceeding the Ray Optics Limit. *Science* **339,** 1057–1060 (2013).

88. Kuncicky, D. M., Christesen, S. D. & Velev, O. D. Role of the Micro- and Nanostructure in the Performance of Surface–Enhanced Raman Scattering Substrates Assembled from Gold Nanoparticles. *Appl. Spectrosc.* **59,** 401–409 (2005).

89. Luo, Z. *et al.* Atomic Gold–Enabled Three-Dimensional Lithography for Silicon Mesostructures. *Science* **348,** 1451–1455 (2015).

90. Day, R. W. *et al.* Plateau–Rayleigh Crystal Growth of Periodic Shells on One-Dimensional Substrates. *Nat. Nanotechnol.* **10,** 345–352 (2015).

91. Lim, S. K., Crawford, S., Haberfehlner, G. & Gradecak, S. Controlled Modulation of Diameter and Composition Along Individual III–V Nitride Nanowires. *Nano Lett.* **13,** 331–336 (2013).

92. Crawford, S., Lim, S. K. & Gradecak, S. Fundamental Insights into Nanowire Diameter Modulation and the Liquid/Solid Interface. *Nano Lett.* **13,** 226–32 (2013).

93. Ma, Z. *et al.* Vapor–Liquid–Solid Growth of Serrated GaN Nanowires: Shape Selection Driven by Kinetic Frustration. *J. Mater. Chem. C* **1,** 7294 (2013).

94. Kallesoe, C. *et al.* Integration, Gap Formation, and Sharpening of III–V Heterostructure Nanowires by Selective Etching. *J. Vac. Sci. Technol. B Microelectron. Nanom. Struct.* **28,** 21 (2010).

95. Fu, L.-T. *et al.* Fabrication and Visible Emission of Single-Crystal Diameter-Modulated Gallium Phosphide Nanochains. *J. Appl. Phys.* **107,** 124321 (2010).

96. Ross, F. M. Controlling Nanowire Structures through Real Time Growth Studies. *Reports Prog. Phys.* **73,** 114501 (2010).

97. Zeng, Z. M., Li, Y., Chen, J. J. & Zhou, W. L. GaP/GaO_x Core–Shell Nanowires and Nanochains and Their Transport Properties. *J. Phys. Chem. C* **112,** 18588–18591 (2008).

98. Ross, F. M., Tersoff, J. & Reuter, M. C. Sawtooth Faceting in Silicon Nanowires. *Phys. Rev. Lett.* **95,** 146104 (2005).

99. Qin, L., Park, S., Huang, L. & Mirkin, C. A. On-wire Lithography. *Science* **309,** 113–5 (2005).

100. Ozel, T., Bourret, G. R. & Mirkin, C. A. Coaxial Lithography. *Nat. Nanotechnol.* **10,** 319–324 (2015).

101. Schmid, H. *et al.* Template-Assisted Selective Epitaxy of III–V Nanoscale Devices for Co-Planar Heterogeneous Integration with Si. *Appl. Phys. Lett.* **106,** 233101 (2015).

102. Kendrick, C. E. *et al.* Radial Junction Silicon Wire Array Solar Cells Fabricated by Gold-Catalyzed Vapor–Liquid–Solid Growth. *Appl. Phys. Lett.* **97,** 143108 (2010).

103. Johannessen, J. S., Spicer, W. E., Gibbons, J. F., Plummer, J. D. & Taylor, N. J. Observation of phosphorus pile-up at the SiO_2-Si interface. *J. Appl. Phys.* **49,** 4453 (1978).

104. Lau, F., Mader, L., Mazure, C., Werner, C. & Orlowski, M. A Model for Phosphorus Segregation at the Silicon-Silicon Dioxide Interface. *Appl. Phys. A* **675,** 671–675 (1989).

105. Schmidt, V., Senz, S. & Gösele, U. Influence of the Si/SiO_2 interface on the charge carrier density of Si nanowires. *Appl. Phys. A* **86,** 187–191 (2006).

106. Kramer, N. J., Schramke, K. S. & Kortshagen, U. R. Plasmonic Properties of Silicon Nanocrystals Doped with Boron and Phosphorus. *Nano Lett.* **15,** 5597–5603 (2015).

107. Sze, S. & Ng, K. K. *Physics of Semiconductor Devices* 3rd, 293–373 (John Wiley & Sons, Inc., Hoboken, NJ, 2007).

108. Gray, J. L. in *Handb. Photovolt. Sci. Eng.* 82–129 (John Wiley & Sons, Ltd, Chichester, UK, 2011).

109. Alamo, J. D., Swirhun, S. & Swanson, R. Simultaneous Measurement of Hole Lifetime, Hole Mobility and Bandgap Narrowing in Heavily Doped n-type Silicon. *1985 Int. Electron Devices Meet.* **31,** 290–293 (1985).

110. Joyce, W. B. & Dixon, R. W. Analytic Approximations for the Fermi Energy of an Ideal Fermi Gas. *Appl. Phys. Lett.* **31,** 354 (1977).

111. Kerr, M. J. & Cuevas, A. General Parameterization of Auger Recombination in Crystalline Silicon. *J. Appl. Phys.* **91,** 2473–2480 (2002).

112. Lieber, C. M. Semiconductor Nanowires: A Platform for Nanoscience and Nanotechnology. *MRS Bull.* **36,** 1052–1063 (2011).

113. Yang, P., Yan, R. & Fardy, M. Semiconductor Nanowire: What's Next? *Nano Lett.* **10,** 1529–1536 (2010).

114. Choi, C. L. & Alivisatos, A. P. From Artificial Atoms to Nanocrystal Molecules: Preparation and Properties of More Complex Nanostructures. *Annu. Rev. Phys. Chem.* **61,** 369–389 (2010).

115. Cui, Y., Wei, Q., Park, H. & Lieber, C. Nanowire Nanosensors for Highly Sensitive and Selective Detection of Biological and Chemical Species. *Science* **293,** 1289–1292 (2001).

116. Law, M. *et al.* Nanoribbon Waveguides for Subwavelength Photonics Integration. *Science* **305,** 1269–1273 (2004).

117. Lee, S.-H., Jung, Y. & Agarwal, R. Highly Scalable Non-volatile and Ultra-low-power Phase-change Nanowire Memory. *Nat. Nanotechnol.* **2,** 626–630 (2007).

118. Qian, F. *et al.* Gallium Nitride-Based Nanowire Radial Heterostructures for Nanophotonics. *Nano Lett.* **4,** 1975–1979 (2004).

119. Kempa, T. J., Day, R. W., Kim, S.-K., Park, H.-G. & Lieber, C. M. Semiconductor Nanowires: a Platform for Exploring Limits and Concepts for Nano-enabled Solar Cells. *Energy Environ. Sci.* **6,** 719 (2013).

120. Hochbaum, A. I. & Yang, P. Semiconductor Nanowires for Energy Conversion. *Chem. Rev.* **110,** 527–546 (2010).

121. Li, Y., Qian, F., Xiang, J. & Lieber, C. M. Nanowire Electronic and Optoelectronic Devices. *Mater. Today* **9,** 18–27 (2006).

122. Björk, M. T. *et al.* One-dimensional Steeplechase for Electrons Realized. *Nano Lett.* **2,** 87–89 (2002).

123. Eymery, J. *et al.* Strain and Shape of Epitaxial InAs/InP Nanowire Superlattice Measured by Grazing Incidence X-ray Techniques. *Nano Lett.* **7,** 2596–2601 (2007).

124. Laocharoensuk, R. *et al.* Flow-based Solution–liquid–solid Nanowire Synthesis. *Nat. Nanotechnol.* **8,** 660–666 (2013).

125. Yang, C., Zhong, Z. & Lieber, C. M. Encoding Electronic Properties by Synthesis of Axial Modulation-Doped Silicon Nanowires. *Science* **310,** 1304–1307 (2005).

126. Lilach, Y., Zhang, J.-P., Moskovits, M. & Kolmakov, A. Encoding Morphology in Oxide Nanostructures During their Growth. *Nano Lett.* **5,** 2019–22 (2005).

127. Chueh, Y.-L. *et al.* Nanoscale Structural Engineering via Phase Segregation: Au–Ge System. *Nano Lett.* **10,** 393–397 (2010).

128. Kline, T. R. *et al.* Template-Grown Metal Nanowires. *Inorg. Chem.* **45,** 7555–7565 (2006).

129. Zheng, G. F., Lu, W., Jin, S. & Lieber, C. M. Synthesis and Fabrication of High-Performance n-Type Silicon Nanowire Transistors. *Adv. Mater.* **16,** 1890–1893 (2004).

130. Wang, Y. *et al.* Use of Phosphine as an n-Type Dopant Source for Vapor-Liquid-Solid Growth of Silicon Nanowires. *Nano Lett* **5,** 2139–43 (2005).

131. Schmid, H. *et al.* Doping Limits of Grown in situ Doped Silicon Nanowires Using Phosphine. *Nano Lett.* **9,** 173–177 (2009).

132. Seidel, H., Csepregi, L., Heuberger, A. & Baumgartel, H. Anisotropic Etching of Crystalline Silicon in Alkaline-Solutions: II. Influence of Dopants. *J. Electrochem. Soc.* **137,** 3626–3632 (1990).

133. Kempa, T. J. *et al.* Single and Tandem Axial p–i–n Nanowire Photovoltaic Devices. *Nano Lett.* **8,** 3456–3460 (2008).

134. Schmid, H. *et al.* Patterned Epitaxial Vapor-Liquid-Solid Growth of Silicon Nanowires on Si(111) Using Silane. *J. Appl. Phys.* **103,** 024304 (2008).

135. He, R., Feng, X. L., Roukes, M. L. & Yang, P. Self-transducing Silicon Nanowire Electromechanical Systems at Room Temperature. *Nano Lett.* **8,** 1756–61 (2008).

136. Lindquist, N. C., Nagpal, P., McPeak, K. M., Norris, D. J. & Oh, S.-H. Engineering Metallic Nanostructures for Plasmonics and Nanophotonics. *Reports Prog. Phys.* **75,** 036501 (2012).

137. Hochbaum, A. I. *et al.* Enhanced Thermoelectric Performance of Rough Silicon Nanowires. *Nature* **451,** 163–167 (2008).

138. Zianni, X. Diameter-modulated Nanowires as Candidates for High Thermoelectric Energy Conversion Efficiency. *Appl. Phys. Lett.* **97,** 233106 (2010).

139. Williams, K. R. & Muller, R. S. Etch rates for micromachining processing. *J. Microelectromechanical Syst.* **5,** 256–269 (1996).

140. Bean, K. E. Anisotropic Etching of Silicon. *IEEE Trans. Electron Devices* **25,** 1185–1193 (1978).

141. Chou, L.-w., Boyuk, D. S. & Filler, M. A. Optically Abrupt Localized Surface Plasmon Resonances in Si Nanowires by Mitigation of Carrier Density Gradients. *ACS Nano* **9,** 1250–1256 (2015).

142. Willets, K. A. & Van Duyne, R. P. Localized Surface Plasmon Resonance Spectroscopy and Sensing. *Annu Rev Phys Chem* **58,** 267–297 (2007).

143. Schuller, J. A. *et al.* Plasmonics for Extreme Light Concentration and Manipulation. *Nat. Mater.* **9,** 193–204 (2010).

144. Barnard, E. S., White, J. S., Chandran, A. & Brongersma, M. L. Spectral Properties of Plasmonic Resonator Antennas. *Opt. Express* **16,** 16529 (2008).

145. Pedano, M. L., Li, S., Schatz, G. C. & Mirkin, C. A. Periodic Electric Field Enhancement Along Gold Rods with Nanogaps. *Angew. Chemie Int. Ed.* **49,** 78–82 (2010).

146. Li, S., Pedano, M. L., Chang, S.-H., Mirkin, C. A. & Schatz, G. C. Gap Structure Effects on Surface-Enhanced Raman Scattering Intensities for Gold Gapped Rods. *Nano Lett.* **10,** 1722–1727 (2010).

147. Yao, J., Sun, Z., Zhong, L., Natelson, D. & Tour, J. M. Resistive Switches and Memories from Silicon Oxide. *Nano Lett.* **10,** 4105–10 (2010).

148. Yao, J., Zhong, L., Natelson, D. & Tour, J. M. In-situ Imaging of the Conducting Filament in a Silicon Oxide Resistive Switch. *Sci. Rep.* **2** (2012).

149. Christesen, J. D. *et al.* Design Principles for Photovoltaic Devices Based on Si Nanowires with Axial or Radial p–n Junctions. *Nano Lett.* **12,** 6024–6029 (2012).

150. Kallesoe, C. *et al.* Selective Etching of III–V Nanowires for Molecular Junctions. *Microelectron. Eng.* **85,** 1179–1181 (2008).

151. Lu, W. & Lieber, C. M. Nanoelectronics from the bottom up. *Nat. Mater.* **6,** 841–50 (2007).

152. Kim, S.-K. *et al.* Tuning Light Absorption in Core/Shell Silicon Nanowire Photovoltaic Devices through Morphological Design. *Nano Lett.* **12,** 4971–6 (2012).

153. Sirbuly, D. J., Law, M., Yan, H. & Yang, P. Semiconductor Nanowires for Subwavelength Photonics Integration. *J. Phys. Chem. B* **109,** 15190–213 (2005).

154. Tian, B., Kempa, T. J. & Lieber, C. M. Single Nanowire Photovoltaics. *Chem. Soc. Rev.* **38,** 16–24 (2009).

155. Dasgupta, N. P. & Yang, P. Semiconductor Nanowires for Photovoltaic and Photoelectrochemical Energy Conversion. *Front. Phys.* **9,** 289–302 (2013).

156. Garnett, E. C., Brongersma, M. L., Cui, Y. & McGehee, M. D. Nanowire Solar Cells. *Annu. Rev. Mater. Res.* **41,** 269–295 (2011).

157. Thelander, C., Nilsson, H. a., Jensen, L. E. & Samuelson, L. Nanowire Single-Electron Memory. *Nano Lett.* **5,** 635–638 (2005).

158. Rigutti, L. *et al.* Ultraviolet Photodetector Based on GaN/AlN Quantum Disks in a Single Nanowire. *Nano Lett.* **10,** 2939–43 (2010).

159. Jiang, Z., Qing, Q., Xie, P., Gao, R. & Lieber, C. M. Kinked p–n Junction Nanowire Probes for High Spatial Resolution Sensing and Intracellular Recording. *Nano Lett.* **12,** 1711–1716 (2012).

160. Cui, Y. *et al.* Efficiency Enhancement of InP Nanowire Solar Cells by Surface Cleaning. *Nano Lett.* **13,** 4113–7 (2013).

161. Dey, A. W. *et al.* Combining Axial and Radial Nanowire Heterostructures: Radial Esaki Diodes and Tunnel Field-Effect Transistors. *Nano Lett.* **13,** 5919–59124 (2013).

162. Ganjipour, B., Dey, A., Borg, B. & Ek, M. High Current Density Esaki Tunnel Diodes Based on GaSb-InAsSb Heterostructure Nanowires. *Nano Lett.* **11,** 4222–4226 (2011).

163. Nguyen, H. P. T. *et al.* Controlling Electron Overflow in Phosphor-Free InGaN/GaN Nanowire White Light-Emitting Diodes. *Nano Lett.* **12,** 1317–23 (2012).

164. Li, N., Tan, T. Y. & Gösele, U. Transition Region Width of Nanowire Hetero- and pn-Junctions Grown Using Vapor-Liquid-Solid Processes. *Appl. Phys. A Mater. Sci. Process.* **90,** 591–596 (2008).

165. Givargizov, E. I. Fundamental Aspects of VLS Growth. *J. Cryst. Growth* **31,** 20–30 (1975).

166. Pinion, C. W., Nenon, D. P., Christesen, J. D. & Cahoon, J. F. Identifying Crystallization- and Incorporation-Limited Regimes during Vapor–Liquid–Solid Growth of Si Nanowires. *ACS Nano* **8,** 6081–6088 (2014).

167. Persson, A. I. *et al.* Solid-Phase Diffusion Mechanism for GaAs Nanowire Growth. *Nat. Mater.* **3,** 677–81 (2004).

168. Christesen, J. D., Pinion, C. W., Grumstrup, E. M., Papanikolas, J. M. & Cahoon, J. F. Synthetically Encoding 10 nm Morphology in Silicon Nanowires. *Nano Lett.* **13,** 6281–6286 (2013).

169. Chou, L. & Filler, M. Engineering Multimodal Localized Surface Plasmon Resonances in Silicon Nanowires. *Angew. Chemie Int. Ed.* **52,** 8079–8083 (2013).

170. Bjork, M., Schmid, H., Knoch, J., Riel, H. & Riess, W. Donor Deactivation in Silicon Nanostructures. *Nat. Nanotechnol.* **4,** 103–107 (2009).

171. Mueller, D. & Fichtner, W. Highly n-doped Silicon: Deactivating Defects of Donors. *Phys. Rev. B* **70,** 245207 (2004).

172. Thurber, W., Mattis, R. & Liu, Y. Resistivity-Dopant Density Relationship for Phosphorus-Doped Silicon. *J. Electrochem. Soc.* **127,** 1807–1812 (1980).

173. Wallentin, J. & Borgström, M. T. Doping of semiconductor nanowires. *J. Mater. Res.* **26,** 2142–2156 (2011).

174. Zhu, Z., Joshi, S., Grover, S. & Moddel, G. *Rectenna Solar Cells* (eds Moddel, G. & Grover, S.) 209–227 (Springer New York, New York, NY, 2013).

175. Sharma, A., Singh, V., Bougher, T. L. & Cola, B. A. A Carbon Nanotube Optical Rectenna. *Nat. Nanotechnol.* **10,** 1027–1032 (2015).

176. Belinicher, V. & Sturman, B. The photogalvanic effect in media lacking a center of symmetry. *Uspekhi Fiz. Nauk* **130,** 415 (1980).

177. Matthias, S. & Muller, F. Asymmetric pores in a silicon membrane acting as massively parallel brownian ratchets. *Nature* **424,** 53–57 (2003).

178. Prost, J., Chauwin, J.-F., Peliti, L. & Ajdari, A. Asymmetric Pumping of Particles. *Phys. Rev. Lett.* **72,** 2652–2655 (1994).

179. Astumian, R. D. Thermodynamics and Kinetics of a Brownian Motor. *Science* **276,** 917–922 (1997).

180. Yanagida, T., Kitamura, K., Tokunaga, M. & Iwane, A. H. A Single Myosin Head Moves Along an Actin Filament with Regular Steps of 5.3 Nanometres. *Nature* **397,** 129–134 (1999).

181. Novotny, L. & van Hulst, N. Antennas for Light. *Nat. Photonics* **5,** 83–90 (2011).

182. Glass, A. M. High-Voltage Bulk Photovoltaic Effect and the Photorefractive Process in $LiNbO_3$. *Appl. Phys. Lett.* **25,** 233 (1974).

183. Sasabe, H., Nakayama, T., Kumazawa, K., Miyata, S. & Fukada, E. Photovoltaic Effect in Poly(vinylidene fluoride). *Polym. J.* **13,** 967–973 (1981).

184. Bune, A. V., Fridkin, V. M., Verkhovskaya, K. A. & Taylor, G. Photoelectric Properties of the Ferroelectric Polymer Poly(vinylidene fluoride). *Polym. J.* **22,** 7–14 (1990).

185. Ramvall, P. *et al.* $Ga_{0.25}In_{0.75}As$/InP quantum wells with extremely high and anisotropic two-dimensional electron gas mobilities. *Appl. Phys. Lett.* **68,** 1111 (1996).

186. Song, A. Electron Ratchet Effect in Semiconductor Devices and Artificial Materials with Broken Centrosymmetry. *Appl. Phys. A* **75,** 229–235 (2002).

187. Bisotto, I. *et al.* Microwave based nanogenerator using the ratchet effect in Si/SiGe heterostructures. *Nanotechnology* **22,** 245401 (2011).

188. Song, A. M. *et al.* Room-Temperature and 50 GHz Operation of a Functional Nanomaterial. *Appl. Phys. Lett.* **79,** 1357–1359 (2001).

189. Sassine, S. *et al.* Experimental investigation of the ratchet effect in a two-dimensional electron system with broken spatial inversion symmetry. *Phys. Rev. B* **78,** 045431 (2008).

190. Kannan, E. S., Bisotto, I., Portal, J.-C., Murali, R. & Beck, T. J. Photovoltage Induced by Ratchet Effect in Si/SiGe Heterostructures under Microwave Irradiation. *Appl. Phys. Lett.* **98,** 193505 (2011).

191. Weber, L. & Gmelin, E. Transport properties of silicon. *Appl. Phys. A Solids Surfaces* **53,** 136–140 (1991).

192. Lundstrom, M. *Fundamentals of Carrier Transport, 2nd edn* 2002.

193. Tian, B. *et al.* Coaxial Silicon Nanowires as Solar Cells and Nanoelectronic Power Sources. *Nature* **449,** 885–889 (2007).

194. Garnett, E. & Yang, P. Light Trapping in Silicon Nanowire Solar Cells. *Nano Lett.* **10,** 1082–1087 (2010).

195. Putnam, M. C. *et al.* Si Microwire-Array Solar Cells. *Energy Environ. Sci.* **3,** 1037 (2010).

196. Kelzenberg, M. D. *et al.* High-performance Si Microwire Photovoltaics. *Energy Environ. Sci.* **4,** 866 (2011).

197. Mohite, A. D. *et al.* Highly Efficient Charge Separation and Collection across in Situ Doped Axial VLS-Grown Si Nanowire p–n Junctions. *Nano Lett.* **12,** 1965–1971 (2012).

198. Lu, Y. & Lal, A. High-Efficiency Ordered Silicon Nano-Conical-Frustum Array Solar Cells by Self-Powered Parallel Electron Lithography. *Nano Lett.* **10,** 4651–4656 (2010).

199. Heurlin, M. *et al.* Axial InP Nanowire Tandem Junction Grown on a Silicon Substrate. *Nano Lett.* **11,** 2028–2031 (2011).

200. Dong, Y., Tian, B., Kempa, T. J. & Lieber, C. M. Coaxial Group III–Nitride Nanowire Photovoltaics. *Nano Lett.* **9,** 2183–2187 (2009).

201. Colombo, C., Heiβ, M., Grätzel, M. & Fontcuberta i Morral, A. Gallium Arsenide p-i-n Radial Structures for Photovoltaic Applications. *Appl. Phys. Lett.* **94,** 173108 (2009).

202. Gutsche, C. *et al.* Direct Determination of Minority Carrier Diffusion Lengths at Axial GaAs Nanowire p–n Junctions. *Nano Lett.* **12,** 1453–1458 (2012).

203. Tang, J., Huo, Z., Brittman, S., Gao, H. & Yang, P. Solution-Processed Core-Shell Nanowires for Efficient Photovoltaic Cells. *Nat. Nanotechnol.* **6,** 568–572 (2011).

204. Fan, Z. *et al.* Three-dimensional Nanopillar-array Photovoltaics on Low-Cost and Flexible Substrates. *Nat. Mater.* **8,** 648–653 (2009).

205. Peng, K.-Q. & Lee, S.-T. Silicon Nanowires for Photovoltaic Solar Energy Conversion. *Adv. Mater.* **23,** 198–215 (2011).

206. Schmidt, V., Wittemann, J. V., Senz, S. & Gösele, U. Silicon Nanowires: A Review on Aspects of their Growth and their Electrical Properties. *Adv. Mater.* **21,** 2681–2702 (2009).

207. Cao, L. *et al.* Semiconductor Nanowire Optical Antenna Solar Absorbers. *Nano Lett.* **10,** 439–445 (2010).

208. Wong, S. M. *et al.* Si Nanopillar Array Surface-Textured Thin-Film Solar Cell With Radial p–n Junction. *IEEE Electron Device Lett.* **32,** 176–178 (2011).

209. Green, M. A., Emery, K., Hishikawa, Y. & Warta, W. Solar Cell Efficiency Tables (Version 36). *Prog. Photovoltaics Res. Appl.* **18,** 346–352 (2010).

210. Atwater, H. A. & Polman, A. Plasmonics for Improved Photovoltaic Devices. *Nat. Mater.* **9,** 205–213 (2010).

211. Allen, J. E. *et al.* High-resolution Detection of Au Catalyst Atoms in Si Nanowires. *Nat. Nanotechnol.* **3,** 168–173 (2008).